SEVENTH FRAMEWORK PROGRAMME
THEME ICT-2007.8.3 - FET proactive 3
“Bio-ICT convergence”

Grant agreement for:	**Collaborative Project** (small or medium-scale focused research project)
Project acronym:	LAMPETRA
Project full title:	Life-like Artefacts for Motor-Postural Experiments and Development of new Control Technologies inspired by Rapid Animal locomotion

Grant agreement no.: 216100

Project Deliverable D 2.3:

Report on neural mechanisms underlying decision making and selection of behaviours

Involved period:	**From month 13 to month 42 (March 1, 2009 – July 31, 2011)**
Date of issue:	**July 31, 2011**
Version:	**1.0**
Dissemination level:	**PU**
Responsible partner:	**KI**
Date of release:	**September 5, 2011**
Contact address:	**sten.grillner@ki.se**

The present deliverable consists of 2 different sections; the first deals with the mechanism of behaviour in the basal ganglia, the second with the visuomotor control. The first is made by three manuscripts, while the second is made by one article and one poster.

The presented results are produced thanks to the experimental activity carried out during the third year of the LAMPETRA project. This type of deliverable was also adopted in other FET projects (such as NEUROBOTIC), in which the KI partner has collaborated.

Section 1

Planert, H., S.N. Szydlowski, J.J. Hjorth, S. Grillner, G. Silberberg (2010) Dynamics of synaptic transmission between fast-spiking interneurons and striatal projection neurons of the direct and indirect pathways.

Ericsson J., G. Silberberg, B. Robertson, MA Wikström, S. Grillner (2011) Striatal cellular properties conserved from lampreys to mammals.

Stephenson-Jones M, E. Samuelsson, J. Ericsson, B. Robertson and S. Grillner (2011) Evolutionary conservation of the basal ganglia as a common vertebrate mechanism for action selection.

Section 2

Jones, M., S. Grillner, B. Robertson (2009) Selective projection patterns from subtypes of retinal ganglion cells to tectum and pretectum: distribution and relation to behaviour. J of Comparative Neurology 517:257-275.

Kardamakis et al, 2011 presented at the IBRO meeting in Firenze

Table of Contents

1. Introduction: Dynamics of synaptic transmission between fast-spiking interneurons and striatal projection neurons of the direct and indirect pathways

The striatum plays a major role in motor learning and in determining the pattern of behavior that is selected at any given time in all vertebrates (Graybiel et al., 1994; Barnes et al., 2005; Grillner et al., 2005; McHaffie et al., 2005). It receives converging glutamatergic input from cortex and thalamus, dopaminergic projections from substantia nigra pars compacta, as well as selective GABAergic input from the external pallidum (Bevan et al., 1998), all of which interact with the primarily GABAergic intrinsic striatal microcircuitry. The striatal microcircuit consists mostly of GABAergic neurons, of which medium spiny neurons (MSNs), the projection neurons, constitute the vast majority (Wilson and Groves, 1980; Graveland and DiFiglia, 1985). Synaptic connectivity between MSNs has long been predicted from their morphology (Wilson and Groves, 1980) and in recent years was confirmed at the electrophysiological level (Czubayko and Plenz, 2002; Tunstall et al., 2002; Koo´ s et al., 2004; Venance et al., 2004; Tecuapetla et al., 2007, 2009; Taverna et al., 2008). Synaptic connectivity between MSNs is sparse (Czubayko and Plenz, 2002; Tunstall et al., 2002; Koo´ s et al., 2004; Venance et al., 2004; Taverna et al., 2008) and formed mainly on dendritic shafts and spines (Wilson and Groves, 1980; Somogyi et al., 1981). MSNs also receive strong GABAergic input from the different types of interneurons, with input from fast spiking (FS) cells mainly targeted to the soma and perisomatic regions (Kita et al., 1990; Bennett and Bolam, 1994; Koo´ s and Tepper, 1999; Taverna et al., 2007).

The connectivity between MSNs of the direct (striatonigral) and indirect (striatopallidal) pathways was recently reported (Taverna et al., 2008), showing a higher prevalence of connections formed by striatopallidal neurons onto target MSNs than those formed by striatonigral MSNs. MSNs of the two pathways also differ in the long-term synaptic plasticity of glutamatergic inputs and their dopaminergic modulation (Surmeier et al., 2007; Day et al., 2008). However, the short-term plasticity of afferent excitatory inputs does not differ significantly between direct- and indirect-pathway MSNs (Ding et al., 2008). In the striatum, GABAergic connectivity between MSNs is assumed to have a different functional role than the GABAergic synapses from interneurons onto MSNs (Koo´ s and Tepper, 1999; Koo´ s et al., 2004; Gustafson et al., 2006; Tecuapetla et al., 2007), with the latter suggested to mediate feed forward inhibition after cortical activation (Mallet et al., 2005). To understand the function of these respective intrastriatal synaptic pathways, it is necessary to determine their dynamic properties and how they differ across cell types. In this study, we analyzed the dynamic properties of synapses between identified neuronal pairs in the rodent striatum, in particular the lateral connections between striatonigral and striatopallidal MSNs, and the synaptic connections they receive from FS interneurons. These results have been partly reported in abstract form (Planert et al., 2008).

1.1 Materials and Methods

1.1.1 Slice preparation and recordings

All experiments were performed according to the guidelines of the Stockholm municipal committee for animal experiments. Parasagittal and coronal slices were obtained from rats and mice (postnatal days 14–18 and 21–36, respectively). To distinguish between striatonigral and striatopallidal MSNs, we used transgenic BAC mice expressing enhanced green fluorescent protein (EGFP) inD1 MSNs (Wang et al., 2006b). Slices were cut in ice-cold extracellular solution, kept at 35°C for 30 min, and then moved to room temperature before recordings. Whole-cell patch recordings were obtained from striatal neurons at a temperature of 35 ± 0.5°C. Neurons were visualized using infrared– differential interference contrast (IR-DIC) microscopy (Zeiss FS Axioskop). Recorded neurons were selected visually and up to four neighboring neurons with lateral somatic distances <100 µm were simultaneously recorded (see Fig. 1*A*,*B*). In experiments in which striatonigral MSNs were labeled, we used a mercury lamp (HBO 100; Zeiss) mounted on the same microscope and a fluorescent filter cube (green or red, depending on the use of GFP or fluorescent beads) to determine the subtype of MSNs, and then switched to IR-DIC to perform whole-cell recordings. Classification of nonlabeled MSNs and interneurons was performed during electrophysiological recordings and, when performed, verified by morphological staining. The extracellular solution (both for cutting and recording) contained the following (in mM): 125 NaCl, 25 glucose, 25 $NaHCO_3$, 2.5 KCl, 2 $CaCl_2$, 1.25 NaH_2PO_4, 1 $MgCl_2$. Recordings were amplified using Axoclamp 2B or MultiClamp 700B amplifiers (Molecular Devices), filtered at 2 kHz, digitized (5–20 kHz) using ITC-18 (InstruTECH), and acquired using Igor Pro (Wavemetrics). Patch pipettes were pulled with a Flaming/Brown micropipette puller P-97 (Sutter Instrument) and had an initial resistance of 5–10MΩ, containing the following (in mM): 110 K-gluconate, 10 KCl, 10 HEPES, 4 Mg-ATP, 0.3 GTP, 10 phosphocreatine, and in a subset of neurons 0.4–0.5% biocytin. A subset of experiments in retrogradely labeled rat slices was performed with higher internal chloride concentrations, with either 20 mM K-gluconate and 100 mM KCl, or 105 mM K-gluconate and 30 mM KCl. The latter concentrations were used for all experiments in mice. Liquid junction potential (~10 mV) was not corrected for in any of the recordings. Recordings were performed both in current- and voltage-clamp mode, with access resistance compensated throughout the experiments. Recordings were discarded when access resistance increased beyond 35 M Ω.

1.1.2 Retrograde labeling

Striatonigral neurons were labeled by stereotactic injection of fluorescent latex microspheres (Lumafluor) into the substantia nigra pars reticulata of juvenile rats (postnatal day 12). The beads are transported retrogradely by the axons that terminate at the site of injection. The injection procedure has been described in detail previously (Le Be´ et al., 2007). In short, rats were anesthetized with an intraperitoneal injection of a mixture of Fentanyl (Fentanyl; B. Braun Melsungen) and medetomidine (Domitor; Orion Pharma), diluted in 0.9% saline and administered at a final dose of 300µg/kg. The smooth surface of the skull was pierced with a 20 gauge Microlance syringe (BD Biosciences), and red microspheres were injected with a Hamilton syringe at a volume of 0.4 µl over 1 min. Stereotactic coordinates were as follows: 2.2 mm lateral from midline, 1.1 mm anterior to lambda, and 6.9 mm below the skull surface. To allow diffusion of the solution from the injection site, the syringe was left at the place of injection for at least 5 min.
Bupivacain (Marcain; 2.5 mg/ml; AstraZeneca) was used as local anesthetic before the wound was closed with chirurgical glue (Histoacryl; Aesculap). The analgesic karprofen (Rimadyl; Pfizer) was

administered subcutaneously at 5 mg/kg, and the rats were awakened with intraperitoneal injections of a mixture of atipamezole (Antisedan; Orion Pharma; 1 mg/kg) and naloxone (0.1 mg/kg), diluted in 0.9% saline. After surgery, the pups were returned to their mother's cage. Slices were visualized under fluorescent microscopy, and only slices in which the striatum was clearly labeled were used for electrophysiological recordings.

1.1.3 Stimulation protocols and analysis

Recorded neurons were subject to various stimulation protocols to determine the synaptic and intrinsic electrical properties. Synaptic connections were identified and characterized by stimulation of a presynaptic cell with a train (10, 20, 40, or 70 Hz) of eight strong and brief current pulses (0.5–2 nA; 3 ms), followed by a so-called recovery test pulse between 500 and 600 ms after the train, all reliably eliciting action potentials (APs). Postsynaptic neurons were held near -80 mV to ensure depolarizing responses to GABAergic synapses. For analysis of synaptic properties, the average postsynaptic trace of_20 sweeps was examined for the existence of synaptic responses. Synaptic responses were obtained in current-clamp and voltage-clamp modes, and in both cases exhibited similar dynamic properties. Parameters describing the dynamics of recorded synapses included the synaptic utilization parameter (U) (equivalent to the average release probability) and the time constants of recovery from depression (D) and facilitation (F). These parameters were extracted using the model for synaptic dynamics as previously described (Markram et al., 1998; Tsodyks et al., 1998). Amplitudes of postsynaptic responses are calculated from postsynaptic responses to presynaptic depolarizing pulses. To extract correct amplitudes of postsynaptic responses lying on the decay phase of previous responses, the synaptic decay was fitted by an exponential curve and subtracted. The amplitude of the postsynaptic response, PSPn, is a product of the fraction of available resources, Rn, and a facilitating utilization factor, un, scaled by the absolute synaptic efficacy, A_{se}, as follows:

$$\mathrm{PSP}_n = A_{\mathrm{se}} R_n u_{n\ldots} \quad (1)$$

The utilization factor is increased by each AP and decays back toward U in the time between AP_{s}, t_{ISI}. This process is described by utilization of the synaptic efficiency in the first AP (u_0 =U), and the recovery time constant from facilitation, F, as follows:

$$u_{n+1} = u^n \exp(-t_{\mathrm{ISI}}/F) + U(1- u_n \exp(-t_{\mathrm{ISI}}/F)). \quad (2)$$

Each AP uses the fraction un from the synaptic resources, Rn, which then recovers to a value of 1 at rate of D as follows:

$$R_{n+1}=R_n(1- u_n) \exp(- t_{\mathrm{ISI}}/D) +1- \exp(t_{\mathrm{ISI}}/D). \quad (3)$$

The model parameters describing each of the analyzed connections were extracted from the average synaptic responses.

1.1.4 Morphological staining

Slices in which recorded cells were biocytin filled were fixed in 0.1 M phosphate buffer (PB) containing 4% paraformaldehyde overnight before the staining procedure. Slices stained for light microscopy were first incubated with 0.6% H2O2 in methanol, rinsed in 0.01 M PBS, and thereafter incubated with the ABC elite kit (Vector Laboratories) for 3 h. The ABC complex was diluted with 0.3% Triton X-100 in 0.1 M PB. After rinsing with 0.01 M PBS, the slices were incubated with DAB (The ImmPACT DAB kit; Vector Laboratories) for 4–10 min. Slices were then mounted on gelatin-coated slides, dehydrated, cleared in xylene, and coverslipped with DPX (dibutylphthalate polystyrene xylene) (Sigma-Aldrich). Slices used for fluorescent microscopy were incubated overnight with streptavidin-Cy2 (1:1000 Jackson Immuno Research Laboratories); diluted in 0.1 M PB containing 1% Triton X-100. In between all experimental procedures, slices were washed with 0.01MPBS. Finally, they were placed on slides, let to dry, and thereafter mounted with glycerol containing 2.5% diazabicyclooctane (Sigma-Aldrich) and stored at -20°C.

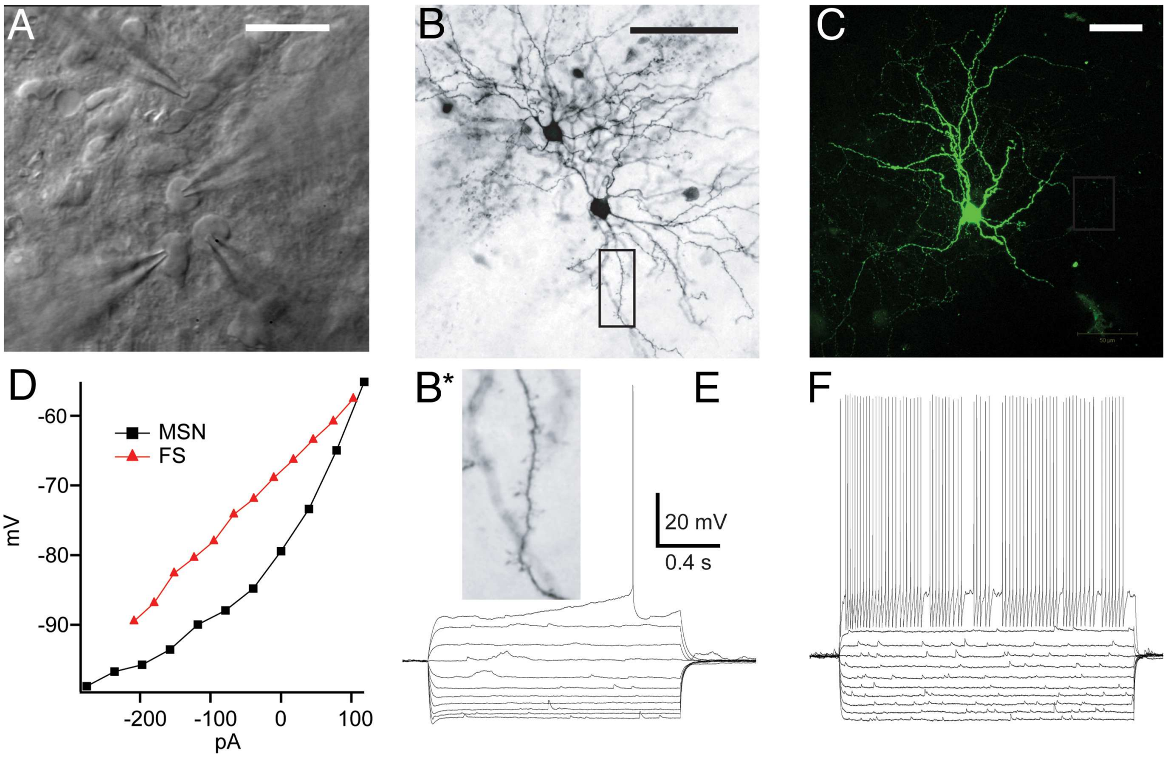

Figure 1. Patch recordings fromMSNand FS striatal neurons. ***A****, Infrared microscopy image of a multineuron patch experiment.* ***B****, Biocytin-filled pair of MSNs (rat; 18 d of age) stained for light microscopy. The enlarged image (****B*****) shows dendritic spines characteristic of MSNs.* ***C****, FS interneuron, biocytin loaded and stained for fluorescent microscopy with aspiny beaded dendrites (rat; 15 d of age).****D****, Example of the current–voltage relationship obtained from an MSN (black squares) and FS cell (red triangles). Note the rectification in the MSN, apparent from the change in curve slope.* ***E****, Response of an MSN to increasing step current injections showing the rectification in hyperpolarized steps, as well as characteristic ramp and delay preceding the action potential.* ***F****, A typical response of an FS cell to the same stimulation protocol as in* ***E****, showing high discharge rate, nonaccommodating discharge pattern, and the fast and deep afterhyperpolarization. Scale bars, 25µm.*

1.2 Results

Classification of recorded neurons

We recorded simultaneously from pairs, triplets, and quadruplets of neighboring (within 100 µm lateral somatic distance) striatal neurons (Fig. 1A–C). The first set of experiments was performed in rat striatal slices, in which neurons were not fluorescently labeled; therefore, differentiation could be done only between MSNs and interneurons. To differentiate between direct- and indirect-pathway MSNs, we then used two complementary methods, fluorescent retrograde labeling in rats and slices from BAC transgenic EGFP mice. Classification of MSNs or FS cells was done according to their electrical properties and, when performed, morphological staining. MSNs and FS cells were unambiguously distinguished from each other by their voltage responses to depolarizing and hyperpolarizing current steps (Kawaguchi et al., 1995; Koo´ s and Tepper, 1999; Taverna et al., 2007). The majority of recorded neurons were MSNs, characterized by a hyperpolarized resting membrane potential, strong inward rectification (Fig. 1D,E), depolarizing ramp response for near-threshold current steps, typical discharge response (Fig. 1E), and spiny dendrites (Fig. 1B). FS cells were characterized by their nonaccommodating or “stuttering” (Gupta et al., 2000) discharge patterns (Fig. 1F), high discharge rate, fast and deep afterhyperpolarization, narrow APs, and aspiny dendrites (Fig. 1C).

Synaptic connections onto MSNs in rat striatum.

Synaptic connectivity was examined for all recorded neuron pairs by evoking APs in presynaptic neurons by brief current injections (see Materials and Methods) and recording the responses in the other simultaneously recorded neurons. Synaptic responses in postsynaptic MSNs were measured at a membrane potential near -80 mV, both in current and voltage clamp. Synaptic responses were recorded within the first 30 min after achieving a whole-cell recording, and in most cases no apparent rundown was observed within that time frame. In rat slices, connectivity between MSNs was sparse (20%; n = 40 of 202 of tested MSN pairs) compared with connections from FS cells to MSNs (74%; n = 29 of 39). Apart from a single case of very weak electrical coupling (coupling coefficient,<0.3%), all connections formed onto MSNs were unidirectional. Synaptic strength differed between the two types of connections, measured as the amplitude of the first synaptic response (PSP) in the train (Fig. 2). FS→MSN connections were more than three times larger than MSN → MSN ones, with an average amplitude of 1.52mV(±2.37; ranging from 0.1 to 7.7 mV; n=31) compared with 0.45 mV (±0.27; range, 0.07–1.21 mV; n = 23; p = 0.02, Student’s t test) (Fig. 2C, Table 1). To assess differences in release probability between the two pathways, we performed a paired-pulse analysis, in which the amplitude ratio of the second and first responses in the train was calculated for a 50ms interval. Both pathways displayed on average paired-pulse depression; however, in MSN→MSN connections, the range of paired-pulse ratios was much larger than in FS→MSN connections (0.88 ± 0.54; range, 0.28 –2.6; compared with 0.64 ± 0.20, ranging 0.25–0.90, respectively) (Fig. 2D, Table 1). Paired-pulse facilitation was observed in seven MSN→MSN connections (see example in Fig. 2A, middle trace) but never in FS→MSN connections.

Differential synaptic dynamics

The variability observed in the paired-pulse properties of MSN→MSNconnections suggested that, in these synapses, facilitation and depression take place simultaneously and underlie the observed dynamics. To extract these properties, we used a phenomenological model for synaptic dynamics that captures a wide range of synaptic activity dependence (Markram et al., 1998; Tsodyks et al., 1998) and is relatively simple to apply to experimental data (see Materials and Methods). The commonly used protocol for this analysis is an AP train followed by a recovery test pulse (see Materials and Methods) (Fig. 3). Interestingly, the recovery test pulse revealed a large difference between the two pathways, in which connections between MSNs displayed strong facilitation (>50% increase) compared with the depression observed in FS→MSN synapses (Fig. 3C,D). The facilitation ratio between the recovery response and the first PSP in MSN→MSN connections was 1.51 (±1.1; ranging between 0.58 and 5.37). Recovery response facilitation was observed in most

(22 of 31) of these connections, in sharp contrast to the FS→MSN connections, which displayed depression in all cases (amplitude ratio, 0.63 ± 0.2; range, 0.24–0.95; n = 23). The facilitation of the recovery test response was present at different train frequencies (Fig. 3A) and at both current- and voltage-clamp recording configurations (Fig. 3*B*). We then used the measured synaptic amplitudes to extract the model parameters quantifying the synaptic dynamics (see Materials and Methods), in particular the time constants for facilitation (F) and depression (D). The relationship between these two time constants determines whether a synapse is depressing ($D > F$), facilitating ($F > D$), or is governed by both processes ($D \sim F$). The respective time constants were extracted for all analyzed synapses and showed clear separation between the two types of synapses (Fig. 3*E*). Whereas FS→MSN synapses were purely depressing, with a very short F (53±53 ms, ranging from 1 to 160 ms), a much longer D (902 ± 954 ms; range, 238–4332 ms), and a small F/D ratio of 0.16, MSN→MSN synapses had a clear facilitatory component alongside depression, as evident from their respective time constants (F, 859 ± 1009 ms; D, 222 ±189 ms) and the high F/D ratio of 4.76 (Fig. 3*F*). The dynamics of the different connections was similar when recorded in voltage- or current-clamp modes, with apparent depression in FS–MSN connections, and a facilitatory component in MSN–MSN connections (Fig. 3*B*). MSN–MSN connections differed only slightly between the two recording configurations, with a decrease in the recovery test response (RTR) facilitation ratio in current traces (1.08 ± 0.28; 0.99 ±0.32; n = 6). Our data show that MSN–MSN connections are sparser, smaller, and more diverse than connections from FS to MSNs. One possible explanation for this diversity is the division of MSNs into two differently projecting subpopulations, namely, the striatonigral and striatopallidal MSNs.

To identify MSNs according to their projection type, we used two alternative methods, retrograde labeling of striatonigral MSNs with fluorescent beads and transgenic EGFP mice (see Materials and Methods) (Fig. 4). In retrogradely labeled rat slices, we simultaneously recorded from labeled (dMSN, for putative direct-pathway MSNs) and nearby nonlabeled (iMSN, for putative indirect-pathway MSNs) neurons (Fig. 4*A*–*C*). Retrogradely labeled neurons were all MSNs, as verified by their electrical properties. In retrogradely labeled slices, we recorded from a total of 83 pairs, 8 of which had synaptic connections (6 connections between MSNs and 2 from FS to MSNs). Both MSN types also received synaptic connections from presynaptic iMSNs (iMSN→iMSN, 2 of 14; iMSN→dMSN, 3 of 10), and 1 connection was found between dMSNs (dMSN→dMSN, 1 of 13). From the six MSN–MSN connections, four had facilitation of the test response, and two were depressing connections (average amplitude ratio, 110±45%; n=6). Labeled and nonlabeled MSNs received synapses from FS cells (one of one FS→dMSN and one of one FS→iMSN connected pairs), both of which were depressing connections, with a clear decrease in the amplitude of the recovery test response (67 and 77% of first PSP, respectively).

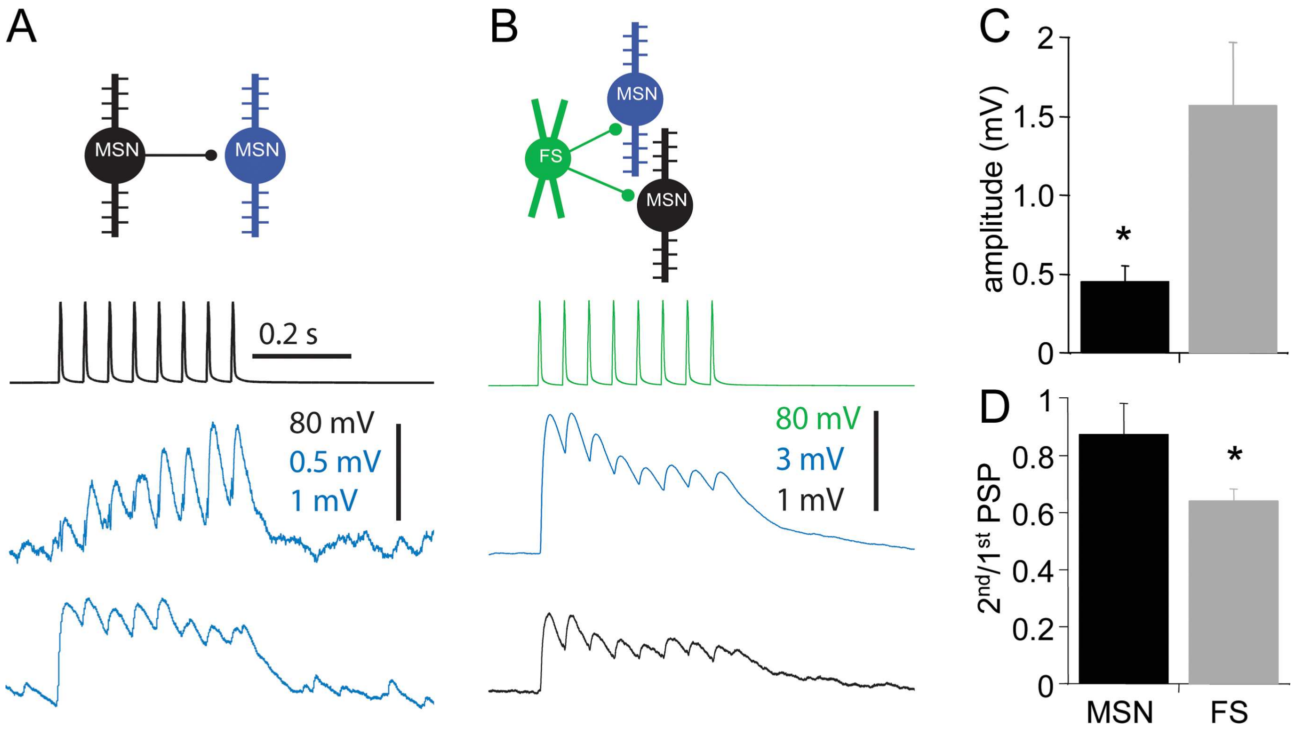

Figure 2. *Synaptic connections formed by MSNs and FS cells onto MSNs. A, Two examples of synaptic connectivity between MSNs. The presynaptic MSN was stimulated with a 20 Hz train of action potentials (top trace; black) and postsynaptic responses (bottom traces; blue) were recorded in postsynaptic MSNs. The middle trace shows a facilitating synaptic response, whereas the bottom one is of a depressing synapse, recorded from a different MSN. B, Synaptic connectivity from FS to MSN. An example of divergent connection from an FS interneuron (green) onto two target MSNs (blue and black). C, Synaptic amplitude of the two types of synapses, measured at the first synaptic response in the train (MSN–MSN connections in black, n 31; FS–MSN in gray, n 23). The difference was significant, with p 0.02, Student's t test. D, Paired-pulse depression in the respective pathways, as calculated from the amplitudes of the first and second responses (p 0.03, t test). The average paired-pulse ratio of MSN–MSN pairs was larger because of the occurrence of depressing and facilitating synapses, which were absent in FS–MSN connections. *p<0.05, Student's t test. Error bars indicate SEM.*

Connectivity of identified MSNs in mouse striatum

As an additional independent method for identifying MSN subpopulations, we used transgenic mice expressing EGFP in dMSNs (Wang et al., 2006b). We recorded from labeled and nonlabeled neighboring neurons in slices of D1-EGFP mice (see Materials and Methods) (Fig. 4*D*–*F*) and found synaptic interactions in 23 of 294 MSN–MSN tested connections (Fig. 5). From these MSN–MSN connections, a majority (74%; 17 of 23) was from presynaptic iMSNs and 6 connections (26%) had a presynaptic dMSN (for synaptic properties, see Table 1). The connections from dMSNs did not have significantly different amplitudes than those from iMSNs (0.28 and 0.39 mV, respectively; $p = 0.55$, *t* test). These connections displayed recovery test facilitation (110 ± 47%; ranging from 62 to 170%; $n = 6$), with two (of three) facilitating dMSN→iMSN connections and one facilitating dMSN→dMSN connection (the three others were depressing synapses). iMSNs formed connections onto dMSNs (13%; $n = 10$ of 80 pairs) and iMSNs (23%; $n = 7$ of 31 pairs), both of which had depressing and facilitating synapses (Fig. 5*A*). The connections from iMSNs onto the two types of target cells were not significantly different in their amplitude (0.27 ± 0.09 and 0.45 ± 0.44 mV, respectively; $p=0.17$, *t* test), paired-pulse ratio (of 111±59 and 95±48%; $p=0.67$), recovery test facilitation (151±64 and 139 ± 69%; $p = 0.98$) (Fig. 5*D*), as well as the utilization factor (*U*) (0.36 ± 0.18 and 0.34 ± 0.19; $p = 0.82$). In these connections, with presynaptic iMSNs, the type of postsynaptic MSNs did not determine the dynamics of the synaptic connection, as we saw in two cases in which a dMSN received both a depressing and a facilitating connection from two different iMSNs (Fig. 5*A*). In two separate cases, the same presynaptic iMSN contacted a dMSN and an iMSN with facilitating synapses, showing that the individual presynaptic MSN, but not the MSN type, determined the synaptic dynamics of the connection (see example in Fig. 5*A*).

Homogenous inhibition of both MSN subpopulations by FS cells

As in rat striatum, FS→MSN connectivity recorded in mice had higher prevalence than MSN→MSN connectivity (78%, 14 of 18; compared with 10%, 23 of 227), larger amplitude (4.21 ± 3.9 mV; 0.41 ± 0.35 mV; $p < 0.001$, Student's *t* test), and displayed only depressing dynamics.

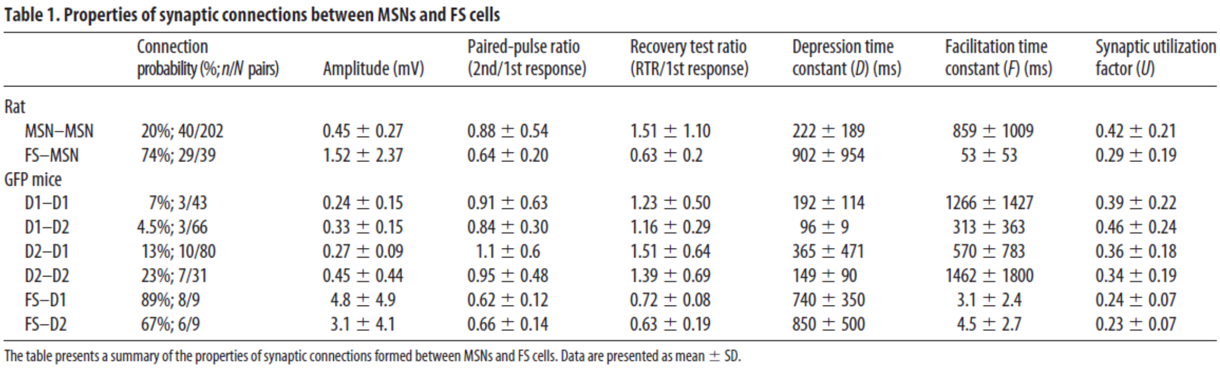

Table 1. Properties of synaptic connections between MSNs and FS cells

	Connection probability (%; *n*/*N* pairs)	Amplitude (mV)	Paired-pulse ratio (2nd/1st response)	Recovery test ratio (RTR/1st response)	Depression time constant (*D*) (ms)	Facilitation time constant (*F*) (ms)	Synaptic utilization factor (*U*)
Rat							
MSN–MSN	20%; 40/202	0.45 ± 0.27	0.88 ± 0.54	1.51 ± 1.10	222 ± 189	859 ± 1009	0.42 ± 0.21
FS–MSN	74%; 29/39	1.52 ± 2.37	0.64 ± 0.20	0.63 ± 0.2	902 ± 954	53 ± 53	0.29 ± 0.19
GFP mice							
D1–D1	7%; 3/43	0.24 ± 0.15	0.91 ± 0.63	1.23 ± 0.50	192 ± 114	1266 ± 1427	0.39 ± 0.22
D1–D2	4.5%; 3/66	0.33 ± 0.15	0.84 ± 0.30	1.16 ± 0.29	96 ± 9	313 ± 363	0.46 ± 0.24
D2–D1	13%; 10/80	0.27 ± 0.09	1.1 ± 0.6	1.51 ± 0.64	365 ± 471	570 ± 783	0.36 ± 0.18
D2–D2	23%; 7/31	0.45 ± 0.44	0.95 ± 0.48	1.39 ± 0.69	149 ± 90	1462 ± 1800	0.34 ± 0.19
FS–D1	89%; 8/9	4.8 ± 4.9	0.62 ± 0.12	0.72 ± 0.08	740 ± 350	3.1 ± 2.4	0.24 ± 0.07
FS–D2	67%; 6/9	3.1 ± 4.1	0.66 ± 0.14	0.63 ± 0.19	850 ± 500	4.5 ± 2.7	0.23 ± 0.07

The table presents a summary of the properties of synaptic connections formed between MSNs and FS cells. Data are presented as mean ± SD.

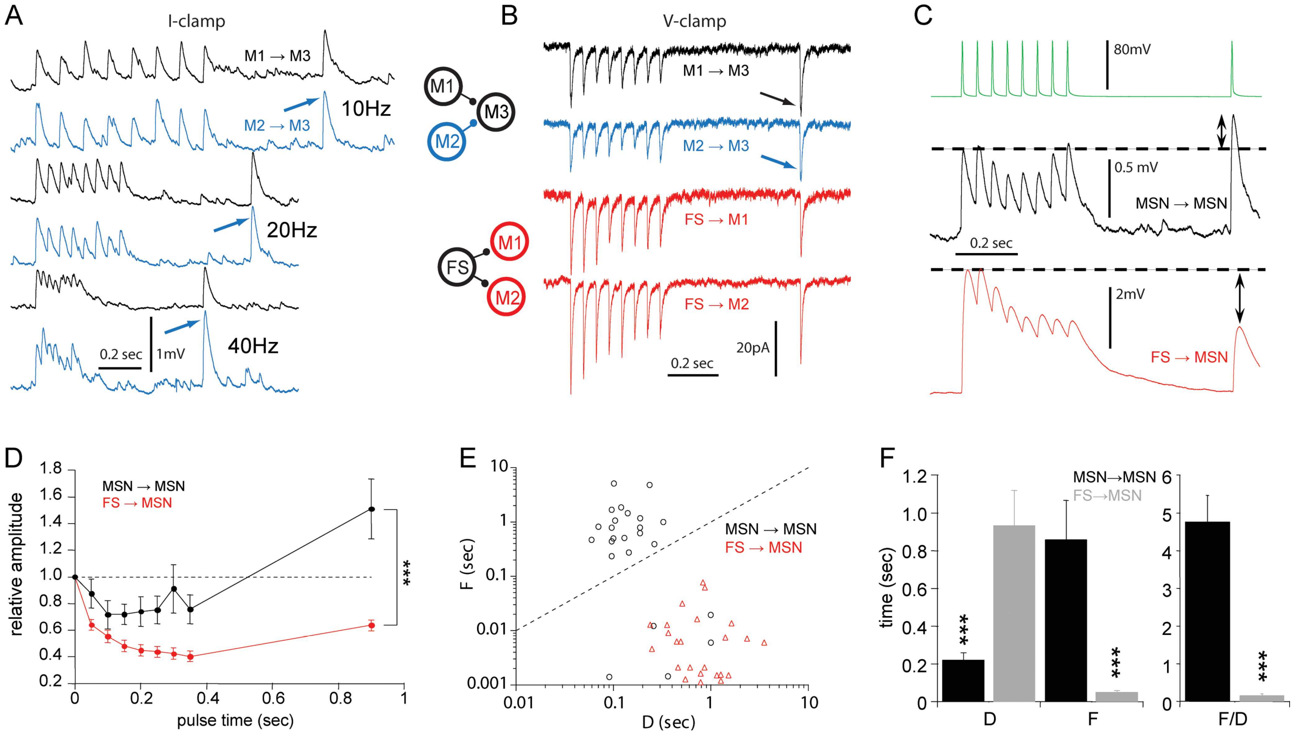

Figure 3. *Differential synaptic dynamics of feedback and feedforward connections.* ***A****, An example of converging MSN–MSN connectivity. A postsynaptic MSN (M3) received direct connections from two neighboring MSNs (M1 and M2). The connection was tested in different train frequencies (10, 20, 40 Hz trains of 8 action potentials), showing frequency-dependent depression and facilitation. Note the increase in amplitude of the recovery test response (denoted by blue arrows), revealing the underlying facilitatory component.* ***B****, Examples of divergent synaptic connectivity from FS to two neighboring MSNs as recorded in voltage clamp (red traces, bottom). Note the depression of the recovery test response after 0.55 s after a 20 Hz train. The top traces are of the same connections as in* ***A****, acquired in voltage-clamp mode.* ***C****, MSNs receive different types of input from neighboring MSNs and FS cells. Two examples of synaptic responses to 20 Hz trains (green) and a recovery response are depicted. Note the facilitation of the recovery response*

in the MSN→MSN connection (black) compared with the depression of the FS→MSN response (red). ***D****, Average responses of all analyzed connections normalized to the amplitude of the first PSP (FS–MSN connections in red, n_23; MSN–MSN in black, n_31).* ***E****, Facilitation and depression time constants of all analyzed connections are plotted against each other in a logarithmic plot. The dashed line represents the F=D curve, showing that all FS→MSN, but not all MSN→MSN connections, were depressing.* ***F****, The synaptic dynamics of the two connection types are significantly different, as seen by the values of the time constants for facilitation (F) and depression (D), and the ratio (right bar graph). ***p<0.001, Student's t test. Error bars indicate SEM*

The high connection probability, combined with the homogeneity in dynamic properties, suggested that both direct- and indirect-pathway MSNs are similarly inhibited by FS interneurons. Indeed, both iMSNs (67%; *n* = 6 of 9) and dMSNs (89%; *n* = 8 of 9) received inhibitory connections from FS cells with very similar dynamic properties. Moreover, in two experiments, we found individual FS cells forming divergent connections on both MSN types (one example depicted in Fig. 6*A*), further suggesting unspecific inhibition mediated by FS cells. The synaptic properties of FS→dMSN and FS→iMSN were not significantly different in terms of their amplitudes (4.8 ± 4.9, *n* = 8; and 3.1 ± 4.1, *n* = 6), paired-pulse depression (62 ± 12 and 66±14%), recovery test response (72±8 and 63±19%), and dynamic model parameters (*U*, 0.24 ± 0.07 and 0.23 ± 0.07; *D*, 0.74 ± 0.35 and 0.85 ± 0.5 s; *F*, 3.1 ± 2.4 and 4.5 ± 2.7 ms) (Fig. 6*B*,*C*, Table 1). These data show that both MSN subpopulations receive ubiquitous and homogeneous inhibition from FS cells, which is, moreover, mediated by the same pool of presynaptic interneurons.

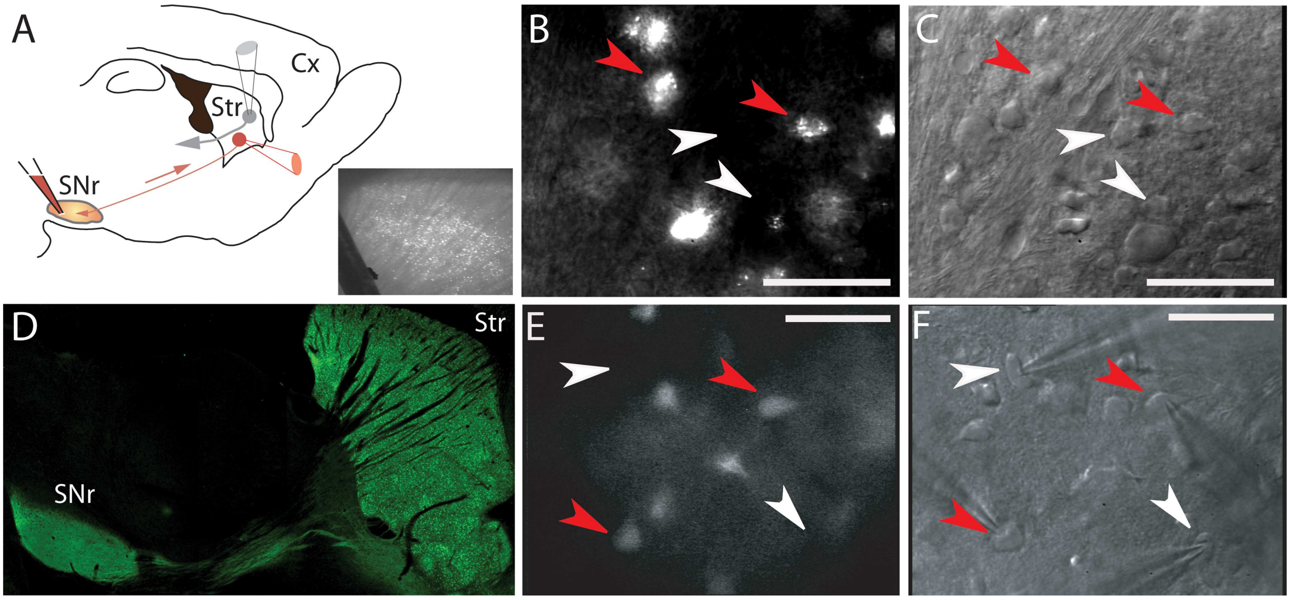

Figure 4. *Fluorescent identification of direct-pathway MSNs.* ***A****, Retrograde labeling of rat striatonigral MSNs by injection of fluorescent beads into the substantia nigra pars reticulata. The beads are transported by the axons to the cell bodies and can then be visualized under fluorescence microscopy.* ***B****, Individual striatal neurons after retrograde labeling. The red arrows designate retrogradely labeled striatonigral MSNs, and the white arrows show the position of unlabeled neurons, which are MSNs or interneurons.* ***C****, The same neurons as in* ***B*** *under infrared microscopy.* ***D****, Confocal image of the striatum and substantia nigra pars reticulata of a BAC transgenic D1-EGFP mouse (image by courtesy of Emmanuel Valjent and Gilberto Fisone, Karolinska Institute, Stockholm, Sweden).* ***E****, Individual striatal neurons in slices of EGFP mouse. The labeled neurons are visible under epifluorescence microscopy and can be selected for recording.* ***F****, The same neurons as in* ***E****, under IR microscopy. The red arrows designate the fluorescent neurons selected to be recorded under IR optics. Scale bars, 50µm. SNr, Substantia nigra pars reticulata; Str, striatum; Cx, cortex.*

1.3 Discussion

In this study, we showed fundamental differences in the dynamic properties of two inhibitory pathways within the striatal microcircuitry. Inhibition by FS cells is robust, homogenous, and exerted by the same FS cells onto both striatonigral and striatopallidal projection neurons. In contrast,MSN–MSNconnectivity is sparser, weaker, and exhibits diverse activity-dependent synaptic dynamics. The connectivity prevalence between MSNs depended on the type of presynaptic MSN; however, the dynamic properties were not determined by the type of interconnected MSNs. The differences between the FS→MSN and MSN→MSN connectivity are clear in both species and throughout different developmental stages, suggesting that they indeed constitute a basic organizational principle in the striatal microcircuitry.

Robust feedforward inhibition from FS cells onto MSNs

Inhibition mediated by FS cells onto MSNs had very different dynamics than that observed between MSNs. FS→MSN synaptic connections mediated large, depressing responses with negligible facilitation, which were strikingly homogenous across different target cells. We show that both neighboring directand indirect-pathway MSNs are inhibited by FS cells, with similar amplitudes and dynamics. It is still not clear whether and to what degree FS cells have preferences for any of the MSN projection types; however, as exemplified in our data, the same FS cells target MSNs of both projection types (Fig. 6*A*). FS cells therefore may not selectively inhibit one striatal projection or the other, but rather efficiently and similarly inhibit a large fraction of their neighboring MSNs of both types. The depressing nature of the FS→MSN synapse makes it tuned to faithfully transmit the onset of FS activity, enabling FS cells to mediate potent synchronized inhibition after cortical excitation (Mallet et al., 2005; but see Berke, 2008). The role of such inhibition by FS cells may be in preventing target MSNs from discharge after excitatory input, but it may also be effective in synchronizing the output of target MSNs without necessarily silencing them completely, but rather by delaying discharge (Koo´ s and Tepper, 1999). Our results suggest that both types of inhibition are very different in terms of their respective dynamics regardless of the postsynaptic MSN type.

This was also shown to be the case for glutamatergic input to MSNs, in which the dynamics of thalamic input was very different from that of cortical input, for both striatopallidal and striatonigral MSNs (Ding et al., 2008). FS→MSN connectivity was severalfold more prevalent than MSN–MSN connectivity, in accord with previous reports (Koo´ s and Tepper, 1999; Koo´ s et al., 2004; Gustafson et al., 2006; Taverna et al., 2007; Tecuapetla et al., 2007). This big difference in connectivity can be partly attributed to the electrotonic attenuation of synaptic responses at distal dendrites compared with the little attenuation of perisomatic inputs from FS cells (Tepper et al., 2008). However, even in experiments in which high intracellular chloride concentrations were used to improve the detection of GABAergic inputs (Koo´ s et al., 2004; Taverna et al., 2008; Tecuapetla et al., 2009), feedback connectivity was sparse. Interestingly, a similar connectivity pattern is found in the neocortical microcircuit, in which projection neurons (pyramidal cells) also constitute the vast majority of neurons and are sparsely interconnected (Markram et al., 1997), whereas connectivity from GABAergic FS interneurons onto pyramidal cells is severalfold higher (Holmgren et al., 2003). This suggests that FS cells in the respective microcircuits, in addition to their similar intrinsic properties (Kawaguchi, 1995; Kawaguchi et al., 1995), share similar network properties and function in mediating feed forward inhibition to their respective principal targets.

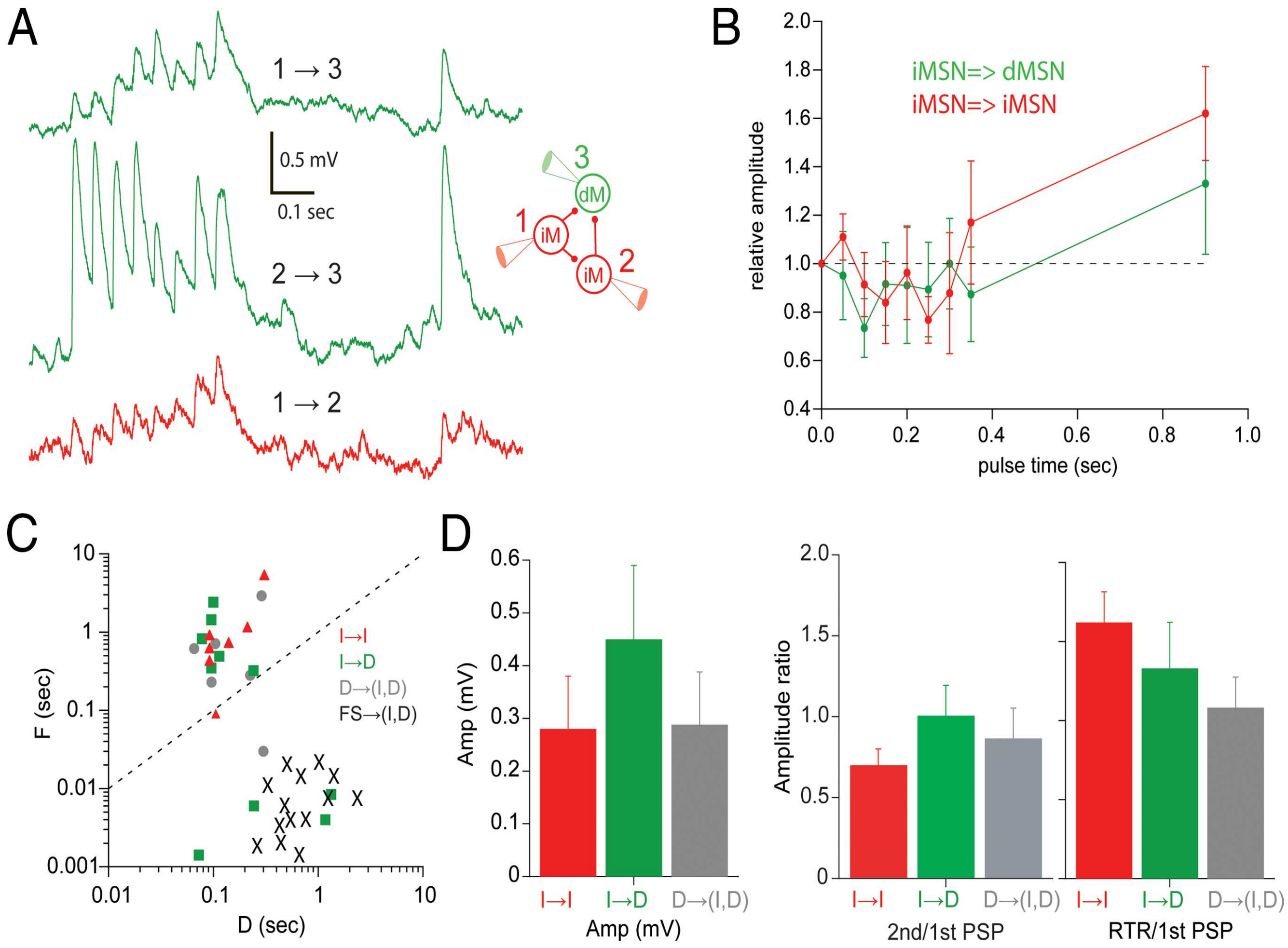

Figure 5. *Synaptic connections between EGFP-identified MSNs. A, A network of neighboring MSNs in ventral striatum displaying divergent and convergent synaptic connections. Cell 3 is a direct-pathway MSN (dM) receiving convergent input from two indirect MSNs (iM) with different dynamic properties. Note the facilitation in the 133 connection (top trace) compared with the depressing connection received by cell 3, and the facilitating connections onto both targets of cell 1. B, Average amplitudes, normalized to the amplitude of the first PSP, for connections from iMSNs onto dMSNs (in green; n=10) and iMSNs (in red; n=7).*

Note the facilitation of the recovery test response, which is absent in FS→MSN connections (Figs. 3, 6). C, Facilitation and depression time constants of connections between identified MSNs are plotted against each other in a logarithmic plot. iMSN→iMSN connections are marked with red triangles, iMSN→dMSN in green squares, presynaptic dMSN connections in gray circles, and FS→MSN connections in black "X." D, Synaptic properties of connections from presynaptic iMSNs did not significantly differ according to the postsynaptic MSN type and were not significantly different from connections between MSNs in which presynaptic neurons were dMSNs. Error bars indicate SEM.

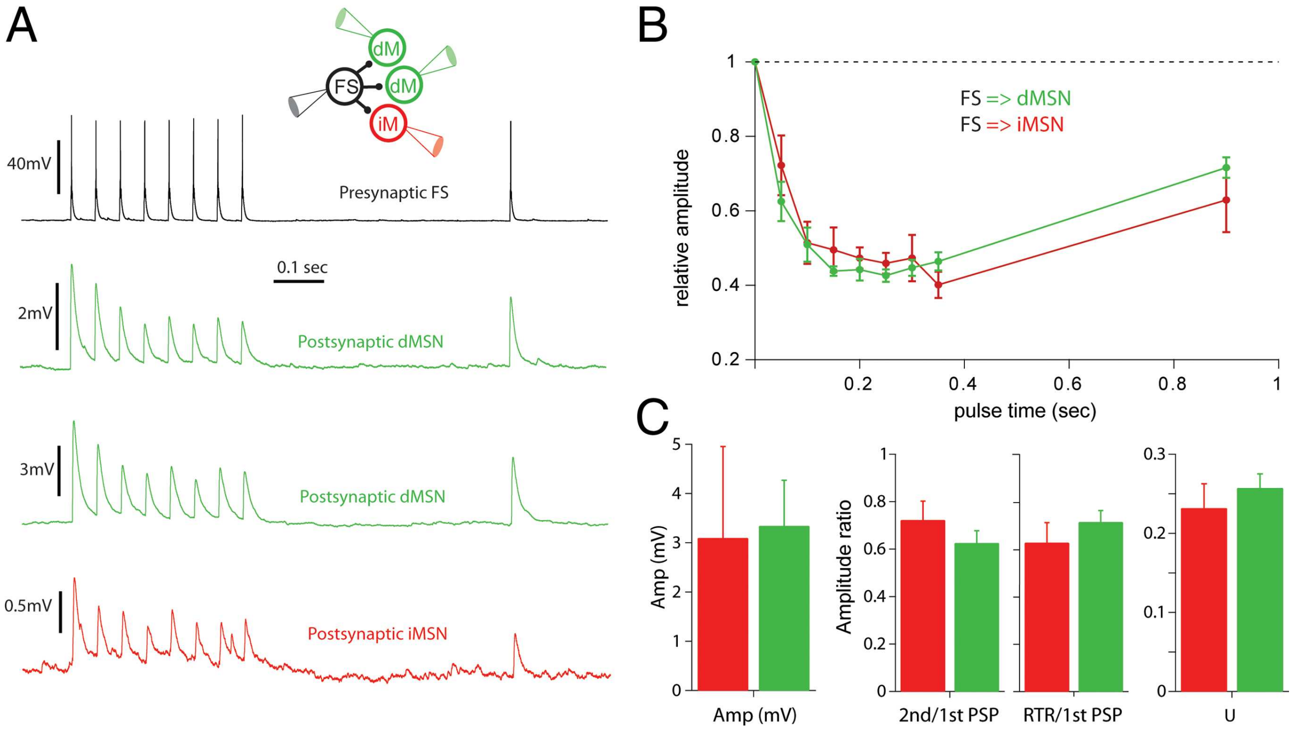

Figure 6. *Synaptic connections from FS cells onto both types of MSNs. A, An example of a divergent connection from a single FS cell onto three target MSNs of different projection types. Note the similarity in the dynamics of the responses on the different MSN types. B, Average amplitudes normalized to the amplitude of the first PSP, for connections from FS onto iMSNs (in red; n 6) and dMSNs (in green; n 9). C, Synaptic properties of connected FS cells did not differ significantly according to the postsynaptic MSN type. Both B and C show the high degree in homogeneity in the FS→MSN pathway onto both projection types of MSNs. Error bars indicate SEM.*

Connectivity between MSNs of different types

Synaptic connections between MSNs of both types displayed a large diversity in terms of the dynamic properties, with cases of depression, facilitation, and mixed responses in which synaptic depression was followed by facilitation of the recovery test response (Fig. 3*A*). This was in sharp contrast to the homogenous dynamics of FS→MSN connections. This variability in dynamics was, surprisingly, not accounted for by the projection identity of the presynaptic and postsynaptic neurons, since all four possible combinations (presynaptic and postsynaptic iMSN/dMSN) had cases of facilitating as well as depressing synapses (Fig. 5). One aspect of MSN–MSN connectivity that did, however, depend on the presynaptic MSN subtype was the prevalence of connectivity.

As reported recently (Taverna et al., 2008), we also observed a non-random organization of MSN interconnectivity, in which synapses formed by iMSNs seemed to be more common than those formed by presynaptic dMSNs. The reasons for this difference are still not clear but may be related to properties of the axonal arborisation and the dendritic targeting preferences of the respective types. The fact that these differences were observed both in rats as well as D1-EGFP mice suggests that it is not an artifact attributable to the particular transgenic mouse used.

Whereas the projection type of connected MSNs did not determine the synaptic dynamics, individual presynaptic neurons induced similar response dynamics in their targets, as seen in divergent connections, both from presynaptic MSNs and FS cells (Figs. 5, 6). Interestingly, this is not the typical scenario in other microcircuits, in which the same presynaptic neuron may induce drastically different synaptic responses in different types of postsynaptic targets (Thomson et al., 1993; Markram et al., 1998; Reyes et al., 1998).

Variability in the dynamics of MSN–MSN synaptic transmission

Unlike the very dominant facilitation observed at certain types of cortical synapses (Thomson et al., 1993), the facilitation in MSN→MSNconnections was commonly masked by a simultaneously occurring depressing component. The interplay between these processes is likely to cause the variability we observed in MSN→MSN connectivity and may also underlie previous reports of both facilitation and depression mediated by presynaptic MSNs (Czubayko and Plenz, 2002; Venance et al., 2004; Rav-Acha et al., 2005; Gustafson et al., 2006). One possible explanation for the observed variability is the postsynaptic dendritic location of MSN–MSN synapses (Wilson and Groves, 1980; Somogyi et al., 1981; Tepper et al., 2008). Unlike FS–MSN synapses, which target a closer and more confined perisomatic region, synapses between MSNs target dendrites with variable thickness and at various electrotonic distances from the soma and dendritic branching point The dendritic locus of MSN–MSN inhibition enables it to affect the nonlinear processes of dendritic integration as well as the plasticity of nearby excitatory inputs, which also target MSN dendrites (Plenz, 2003; Carter et al., 2007; Wilson, 2007; Tepper et al., 2008). In addition to these functional properties, the dendritic location also shapes the apparent dynamics of the synaptic responses (Banitt et al., 2005). Synaptic activation causes a local conductance increase as well as reduction of the synaptic driving force, both of which induce a depressing component in synaptic responses. This “apparent depression” strongly depends on the location of the synaptic contact and is likely to contribute to the variability we observed in synaptic dynamics.

Similar recovery test facilitation was observed in other neural microcircuits in the prefrontal cortex (Wang et al., 2006a) and in the hippocampus (Hefft and Jonas, 2005). As in the MSN–MSN connections we observed, responses typically displayed depression during the burst of action potentials, but facilitated after a pause of several hundreds of milliseconds. This facilitation was observed both in current- and voltage-clamp modes, and was also observed when postsynaptic neurons were recorded in a cesiumbased pipette solution, suggesting that it is mainly dictated by presynaptic processes. The biophysical mechanisms underlying the observed synaptic dynamics were not explored in this study; however, it is predicted that protocols affecting the release process such as changing extracellular calcium concentrations or loading the presynaptic neurons with CsCl (Hull et al., 2009) would significantly alter the dynamics of these connections. Presynaptic calcium channels are subject to multiple modulatory processes that may underlie the various forms of synaptic facilitation (for review, see Catterall and Few, 2008). The variability in synaptic dynamics in MSN–MSN connections was not explained by the type of connected neurons but it may reflect intrinsic variability in both presynaptic and postsynaptic elements. In our study, we did not record neuronal positions with respect to the patch and matrix striatal compartments, which may also contribute to the observed variability in dynamics, as recently suggested for synaptic strength (Tecuapetla et al., 2009).

1.4 Summary

Our study shows that MSN→MSN and FS→MSNinhibitory pathways in the striatum have fundamentally different functional properties, with highly homogenously depressing, reliable inhibition from FS onto both projection pathways, and sparse and variable interconnectivity among MSNs of both direct and indirect projection systems. These results suggest that the functional role of inhibition from FS cells might be not in separating the activity of the two striatal projections, but rather in shaping striatal output for both.

1.5 References

1. Banitt Y, Martin KA, Segev I (2005) Depressed responses of facilitatory synapses. J Neurophysiol 94:865– 870.
2. Barnes TD, Kubota Y, Hu D, Jin DZ, GraybielAM (2005) Activity of striatal neurons reflects dynamic encoding and recoding of procedural memories. Nature 437:1158 –1161.
3. Bennett BD, Bolam JP (1994) Synaptic input and output of parvalbuminimmunoreactive neurons in the neostriatum of the rat. Neuroscience 62:707–719.
4. Berke JD (2008) Uncoordinated firing rate changes of striatal fast-spiking interneurons during behavioral task performance. J Neurosci 28:10075/10080.
5. Bevan MD, Booth PA, Eaton SA, Bolam JP (1998) Selective innervation of neostriatal interneurons by a subclass of neuron in the globus pallidus of the rat. J Neurosci 18:9438–9452.
6. Carter AG, Soler-Llavina GJ, Sabatini BL (2007) Timing and location of synaptic inputs determine modes of subthreshold integration in striatal medium spiny neurons. J Neurosci 27:8967– 8977.
7. Catterall WA, Few AP (2008) Calcium channel regulation and presynaptic plasticity. Neuron 59:882–901.
8. Czubayko U, Plenz D (2002) Fast synaptic transmission between striatal spiny projection neurons. Proc Natl Acad Sci U S A 99:15764 –15769.
9. Day M, Wokosin D, Plotkin JL, Tian X, Surmeier DJ (2008) Differential excitability and modulation of striatal medium spiny neuron dendrites. J Neurosci 28:11603–11614.
10. Ding J, Peterson JD, Surmeier DJ (2008) Corticostriatal and thalamostriatal synapses have distinctive properties. J Neurosci 28:6483– 6492.
11. Graveland GA, DiFiglia M (1985) The frequency and distribution of medium-sized neurons with indented nuclei in the primate and rodent neostriatum. Brain Res 327:307–311.
12. Graybiel AM, Aosaki T, Flaherty AW, Kimura M (1994) The basal ganglia and adaptive motor control. Science 265:1826 –1831.
13. Grillner S, Hellgren J, Me´nard A, Saitoh K, Wikstro¨m MA (2005) Mechanisms for selection of basic motor programs—roles for the striatum and pallidum. Trends Neurosci 28:364 –370.
14. Gupta A, Wang Y, Markram H (2000) Organizing principles for a diversity of GABAergic interneurons and synapses in the neocortex. Science 287:273–278.
15. Gustafson N, Gireesh-Dharmaraj E, Czubayko U, Blackwell KT, Plenz D (2006) A comparative voltage and current-clamp analysis of feedback and feedforward synaptic transmission in the striatal microcircuit in vitro. J Neurophysiol 95:737–752.
16. Hefft S, Jonas P (2005) Asynchronous GABA release generates long-lasting inhibition at a hippocampal interneuron-principal neuron synapse. Nat Neurosci 8:1319 –1328.
17. Holmgren C, Harkany T, Svennenfors B, Zilberter Y (2003) Pyramidal cell communication within local networks in layer 2/3 of rat neocortex. J Physiol 551:139 –153.
18. Hull C, Adesnik H, Scanziani M (2009) Neocortical disynaptic inhibition requires somatodendritic integration in interneurons. J Neurosci 29:8991– 8995.
19. Kawaguchi Y (1995) Physiological subgroups of nonpyramidal cells with specific morphological characteristics in layer II/III of rat frontal cortex. J Neurosci 15:2638 –2655.
20. Kawaguchi Y, Wilson CJ, Augood SJ, Emson PC (1995) Striatal interneurones: chemical, physiological and morphological characterization. Trends Neurosci 18:527–535.
21. Kita H, Kosaka T, Heizmann CW (1990) Parvalbumin-immunoreactive neurons in the rat neostriatum: a light and electron microscopic study. Brain Res 536:1–15.

22. Koo´ s T, Tepper JM (1999) Inhibitory control of neostriatal projection neurons by GABAergic interneurons. Nat Neurosci 2:467– 472.
23. Koo´ s T, Tepper JM, Wilson CJ (2004) Comparison of IPSCs evoked by spiny and fast-spiking neurons in the neostriatum. J Neurosci 24:7916 –7922.
24. Le Be´ JV, Silberberg G, Wang Y, MarkramH (2007) Morphological, electrophysiological, and synaptic properties of corticocallosal pyramidal cells in the neonatal rat neocortex. Cereb Cortex 17:2204 –2213.
25. Mallet N, Le Moine C, Charpier S, Gonon F (2005) Feedforward inhibition of projection neurons by fast-spiking GABA interneurons in the rat striatum in vivo. J Neurosci 25:3857–3869.
26. Markram H, Lu¨bke J, Frotscher M, Roth A, Sakmann B (1997) Physiology and anatomy of synaptic connections between thick tufted pyramidal neurones in the developing rat neocortex. J Physiol 500:409–440.
27. Markram H, Wang Y, TsodyksM (1998) Differential signaling via the same axon of neocortical pyramidal neurons. Proc Natl Acad Sci U S A 95:5323–5328.
28. McHaffie JG, Stanford TR, Stein BE, Coizet V, Redgrave P (2005) Subcortical loops through the basal ganglia. Trends Neurosci 28:401– 407.
29. Planert H, Grillner S, Robertson B, Silberberg G (2008) Intrinsic properties and synaptic connectivity of different subtypes of the striatal medium spiny neuron. Soc Neurosci Abstr 34:670.8.
30. Plenz D (2003) When inhibition goes incognito: feedback interaction between spiny projection neurons in striatal function. Trends Neurosci 26:436–443.
31. Rav-Acha M, Sagiv N, Segev I, Bergman H, Yarom Y (2005) Dynamic and spatial features of the inhibitory pallidal GABAergic synapses. Neuroscience 135:791– 802.
32. Reyes A, Lujan R, Rozov A, Burnashev N, Somogyi P, Sakmann B (1998) Target-cell-specific facilitation and depression in neocortical circuits. Nat Neurosci 1:279 –285.
33. Somogyi P, Bolam JP, Smith AD (1981) Monosynaptic cortical input and local axon collaterals of identified striatonigral neurons. A light and electron microscopic study using the Golgi-peroxidase transport-degeneration procedure. J Comp Neurol 195:567–584.
34. Surmeier DJ, Ding J, Day M, Wang Z, ShenW (2007) D1 and D2 dopaminereceptor modulation of striatal glutamatergic signaling in striatal medium spiny neurons. Trends Neurosci 30:228 –235.
35. Taverna S, Canciani B, PennartzCM (2007) Membrane properties and synaptic connectivity of fast-spiking interneurons in rat ventral striatum. Brain Res 1152:49 –56.
36. Taverna S, Ilijic E, Surmeier DJ (2008) Recurrent collateral connections of striatal medium spiny neurons are disrupted in models of Parkinson’s disease. J Neurosci 28:5504 –5512.
37. Tecuapetla F, Carrillo-Reid L, Bargas J, Galarraga E (2007) Dopaminergic modulation of short-term synaptic plasticity at striatal inhibitory synapses. Proc Natl Acad Sci U S A 104:10258 –10263.
38. Tecuapetla F, Koo´ s T, Tepper JM, Kabbani N, YeckelMF (2009) Differential dopaminergic modulation of neostriatal synaptic connections of striatopallidal axon collaterals. J Neurosci 29:8977– 8990.
39. Tepper JM, Wilson CJ, Koo´ s T (2008) Feedforward and feedback inhibition in neostriatal GABAergic spiny neurons. Brain Res Rev 58:272–281.
40. Thomson AM, Deuchars J, West DC (1993) Single axon excitatory postsynaptic potentials in neocortical interneurons exhibit pronounced paired pulse facilitation. Neuroscience 54:347–360.
41. Tsodyks M, Pawelzik K, Markram H (1998) Neural networks with dynamic synapses. Neural Comput 10:821– 835.

42. Tunstall MJ, Oorschot DE, Kean A, Wickens JR (2002) Inhibitory interactions between spiny projection neurons in the rat striatum. J Neurophysiol 88:1263–1269.
43. Venance L, Glowinski J, Giaume C (2004) Electrical and chemical transmission between striatal GABAergic output neurones in rat brain slices. J Physiol 559:215–230.
44. Wang Y, Markram H, Goodman PH, Berger TK, Ma J, Goldman-Rakic PS (2006a) Heterogeneity in the pyramidal network of the medial prefrontal cortex. Nat Neurosci 9:534 –542.
45. Wang Z, Kai L, Day M, Ronesi J, Yin HH, Ding J, Tkatch T, Lovinger DM, Surmeier DJ (2006b) Dopaminergic control of corticostriatal long-term synaptic depression in medium spiny neurons is mediated by cholinergic interneurons. Neuron 50:443– 452.
46. Wilson CJ (2007) GABAergic inhibition in the neostriatum. Prog Brain Res 160:91–110.
47. Wilson CJ, Groves PM (1980) Fine structure and synaptic connections of the common spiny neuron of the rat neostriatum: a study employing intracellular inject of horseradish peroxidase. J Comp Neurol 194:599 – 615.

2. Introduction: Striatal cellular properties conserved from lampreys to mammals

In the mammalian striatum, 95% of all neurons are GABAergic medium spiny projection neurons (MSNs; cf. Tepper et al. 2007). They are characterised by a negative resting potential due to the presence of potassium channels of the inward rectifier type (Kir) that are open at negative potentials, but closed when the membrane potential is brought to more depolarised levels by synaptic excitatory drive. This property of MSNs makes them difficult to activate by the glutamatergic input fromcortex and thalamus (Wilson & Kawaguchi, 1996; Tepper et al. 2004; Grillner et al. 2005). The responsiveness of MSNs is, however, regulated by the degree of dopaminergic modulatory drive (Surmeier et al. 2007; Redgrave et al. 2008). Without the presence of a dopamine input, mammals become hypokinetic and acquire Parkinsonian symptoms. Conversely, an enhanced level of dopamine leads to hyperkinesias with an unintended initiation of motor programmes. Kir was recently shown to be a characteristic feature of MSNs in reptiles (Barral et al. 2010), which would suggest that Kir is an important property of striatal function in all amniotes (Kawaguchi et al. 1989; Farries & Perkel, 2000). Other characteristic features of MSNs are hyperpolarised resting potentials and a ramping responsewith a long delay to the first action potential due to low-voltage-activated A-type K+ channels (Kawaguchi et al. 1989; Uchimura et al. 1989; Nisenbaum &Wilson, 1995). Cyclostomes (jawless fish like lampreys) represent the first vertebrate group to emerge in evolution. They deviated from the evolutionary line leading up to mammals already 530–560 million years ago, around 200 million years before reptiles emerged (Olsen, 2007). Although a striatum is present in all vertebrates, no information regarding the presence of Kir is available in amphibians, fish or cyclostomes (anamniotes). Recent findings in the lamprey striatum show that it contains spiny GABAergic projection neurons that express dopamine D1 and D2 receptors, tachykinins and enkephalin (Pombal et al. 1997b, 2001; Auclair et al. 2004; Ericsson et al. 2010; Robertson et al. 2010). Striatum receives input from pallium (cortex in mammals) and thalamus, as well as a dopaminergic, 5-HT and histaminergic input (Brodin et al. 1990a,b; Jimenez et al. 1996; Pombal et al. 1997a). The lamprey striatum thus receives the same type of input and expresses the same molecular markers as in mammals and other amniotes. Dopamine depletion with 1-methyl-4-phenyl-1,2,3,6-tetrahydropyridine (MPTP) renders the lamprey hypokinetic, as in Parkinson's, an effect that can be counteracted by dopamine agonists (Thompson et al. 2008). It thus appears that also with regard to function, the role of the basal ganglia is conserved. In this study we wanted to characterise neurons in the lamprey striatum in terms of their electrophysiological, morphological and synaptic input, and isolate some of the key properties supporting generic striatal function in vertebrates.

2.1 Methods

Ethical approval

All experimental procedures conformed to the guidelines of the Stockholm municipal committee for animal experiments.

Slice preparation

Coronal brain slices, 300–500 μm thick, were prepared from 46 lampreys (Lampetra fluviatilis), as described earlier (Ericsson et al. 2007). Usually only one brain slice per animal containing the striatum, located lateral to the medial telencephalic ventricle (Fig. 1A and B), in both hemispheres was obtained due to the small size of the striatum. The striatum can be clearly seen as awell-defined band of cell bodies (Fig. 1A–C).These cells areGABAergic and express substance P and enkephalin, and D1 and D2 receptors (Pombal et al. 1997b; Robertson et al. 2007, 2010). Slices were kept at 4–8°C in artificial cerebrospinal fluid (aCSF) of the following composition (in mM): 125 NaCl, 2.5 KCl, 1 MgCl2, 1.25 NaH2 PO4, 2 CaCl2 , 25 NaHCO3 and 20 glucose. The aCSF was oxygenated continuously with 95% O2 and 5% CO2 (pH 7.4) and was also used for perfusion during recordings at the same temperature (Badkontroller V, Luigs & Neumann, Ratingen, Germany).

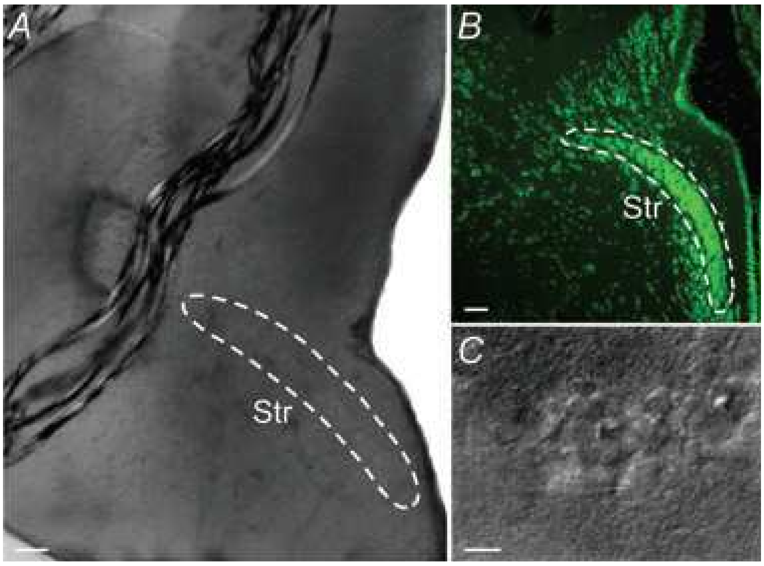

Figure 1. *Anatomical location of the striatum (Str) A, coronal acute brain slice in the recording chamber showing the striatal cell band inside the white lines. B, fluorescent Nissl staining of a coronal section displaying the band of striatal cell bodies. C, photograph of individual striatal neurons in the recording chamber. Scale bars = 100 μm in A and B, 15 μm in C.*

Electrophysiology and morphological reconstruction

Patch-clamp electrodes (7–12MΩ) were filled with (in mM): 102 KCH3SO4, 1.2 MgCl2 , 10 Hepes, 1 CaCl2, 10 EGTA, 3.94 Mg-ATP, 0.3 Na-GTP, 5 phosphocreatine sodium salt and 10 glucose (osmolarity 265–275 mosmol l^{-1}) or with an alternative solution with a higher chloride concentration: 105 potassium gluconate, 30 KCl, 10Hepes, 4Mg-ATP, 0.3Na-GTP and 10 phosphocreatine sodium salt (osmolarity 270 mosmol l^{-1}). Patch electrodes were prepared from borosilicate glass microcapillaries (Harvard Apparatus, Edenbridge, UK) using a two-stage puller (PP-830, Narishige, Japan). Whole-cell recordings were performed in current- or voltage-clamp mode using a Multiclamp 700B amplifier (Molecular Devices, Sunnyvale, CA, USA) and digitised at 10–50 kHz by a PC. Bridge balance andpipette capacitance compensation were automatically adjusted on the amplifier and all membrane potential values were corrected for the liquid junction potential. Neurons were visualised (see example in Fig. 1A and C) with DIC/infrared optics (Zeiss Axioskop 2FS plus, Munich, Germany) and electrodes were advanced using remote micromanipulators (Luigs & Neumann). Data was acquiredwith theClampex software and analysed in Clampfit (pCLAMP, Molecular Devices). Neurons were intracellularly stained by injection of 0.3–0.5% neurobiotin (Vector Laboratories, Burlingame, CA, USA) during recordings. Brain slices were fixed overnight in 4% formalin and 14% picric acid in 0.1 M phosphate buffer (PB) and analysed by either confocal or conventional light microscopy. For confocal imaging (Carl Zeiss LSM 510 Meta, München, Germany), slices were first incubated in streptavidin-Cy2 (1:1000, Jackson Immunoresearch Laboratories, West Grove, PA, USA) in 0.3% Triton X-100 and 1%BSA in 0.1 MPB overnight. The sliceswere then washed in 0.01 Mphosphate buffered saline (PBS) before being dehydrated in alcohol and transferred to methyl salicylate(Merck,NJ, USA) prior tomounting in DPX(Fluka/Sigma-Aldrich, StLouis,MO,USA).Confocal image reconstructionswere made and analysed using Zeiss LSM Image Browser and ImageJ software (Rasband WS, National Institutes of Health, Bethesda, MD, USA). Some slices were instead processed with the Vectastain Elite ABC kit (Vector Laboratories). Slices were thoroughly washed in 0.01 M PBS and incubated in 0.6% hydrogen peroxidase in methanol for 20 min, rinsed in PBS and transferred to the ABC solution for 3 h. After rinsing in PBS, slices were incubated in diaminobenzidine (DAB; ImmPACT DAB, Vector Laboratories) for 5min, then rinsed and dehydrated in alcohol prior to mounting in DPX. Subsequently, neurons were visualised in a light microscope (Olympus BX51, Melville, NY, USA) and photomicrographs were taken using Cell A (Olympus). Formalin fixed lamprey brain sections, 20 µm thick, were stained with a green fluorescent Nissl stain (1:1000; Molecular Probes Europe BV, Leiden, theNetherlands) for analysis of striatal morphology.

Electrophysiological analysis

Neurons that had stable responses with large over-shooting (reaching above 0 mV) action potentials (mean amplitude ∼54 mV) during step depolarisations in current clamp recordings were considered healthy and were subsequently analysed (see for example Fig. 2A).

Most recordings were performed in current clamp mode, with injections of hyperpolarising and depolarising current steps to investigate voltage responses. Action potentials were triggered by positive current pulses and the amplitude measured relative to the firing threshold.

The time delay to the first action potential was measured on the first current injection step that elicited an action potential, in a series of increasing steps from a baseline around −75 mV. The input resistance of neurons was calculated by dividing the steady-state voltage response by the applied current injection. A rectification index was defined as the ratio between the input resistance at very hyperpolarised potentials (around −100 to −120 mV) and the input resistance at the resting potential, where no obvious Na+ conductances had been activated. Thus, large rectification would inversely correspond to a low index since the input resistance at hyperpolarised levels is low while it is significantly higher at more depolarised levels. To quantify the voltage ‘sag’ sometimes seen at hyperpolarised potentials, a sag index was calculated. The sag index was defined as the difference of the most hyperpolarised voltage and the steady-state voltage deflection of that pulse (Sag ΔV in Fig. 4A) divided by the steady-state deflection. Thus, a large voltage sag correspond to a high sag index, so for example an index of 1 would correspond to an amplitude of the hyperpolarised voltage that was twice as large as the steady-state response.

The average action potential frequency in a spike train was measured between the first and the last action potential during a 1 s suprathreshold current injection. Spontaneous synaptic inputs were recorded using an alternative intracellular solution with 30mM KCl in the pipette solution to ensure that GABAergic events were detected more easily as depolarising events at the resting potential. These were measured in current clamp mode and analysed bymonitoring the frequency of events before and during bath application of drugs. The following drugs were used and applied directly in the extracellular bath: the K+ channel blocker 4-aminopyridine (4-AP, 100–500 μM, Sigma-Aldrich, St Louis, MO, USA), Barium chloride (100 μM Sigma- Aldrich), the monovalent cation current Ih antagonist ZD 7288 (50 μM, Tocris Bioscience, Ellisville, MO, USA), the AMPA receptor antagonist NBQX disodium salt (40 μM, Tocris) and the GABAA receptor antagonist gabazine (40 μM, Tocris).

Statistics

Results are presented asmeans±standard deviation (SD) and statistical comparisons between means were made with Student’s two-tailed paired t test with GraphPad Prism Software (GraphPad Software, San Diego, CA, USA).

2.2 Results

Whole-cell recordings were obtained from 74 neurons that were classified into two main subgroups based on the presence or absence of inward rectification observed by injection of depolarising and hyperpolarising current steps. Pronounced inward rectification is a hallmark of MSNs in amniotes and clearly differentiates these neurons from other striatal interneurons and is therefore of special interest (Kawaguchi *et al.* 1989; Grillner *et al.* 2005; Barral *et al.* 2010). It is identified by lower input resistance at more negative potentials due to the opening of K+ (Kir) channels (Uchimura *et al.* 1989).

An example of an inwardly rectifying neuron is depicted in Fig. 2*A*. The rectification in lamprey striatal neurons was quantified by calculating the ratio between the input resistance at −120 mV and at resting potential (Fig. 2*B* and *C*). Two clusters of neurons with rectification ratios below or above 0.5 were apparent when plotting the rectification ratios (Fig. 2*B*). Forty-eight neurons (65%) had rectification values below 0.5 and displayed clear inward rectification, seen by visual inspection of the voltage responses to stepwise hyperpolarising and depolarising current injections at subthreshold values, and are referred to as inwardly rectifying neurons (IRNs). The population of neurons with rectification values above 0.5 did not show marked inward rectification (Fig. 6) and are referred to as ‘non-IRNs’.We recognise that some neurons classified as non-IRNs here still exhibit a certain degree of inward rectification as indicated by the inward rectification ratio in Fig. 2*B*. No neurons fired action potentials at rest. The basic membrane properties of the two groups are summarised in Table 1.

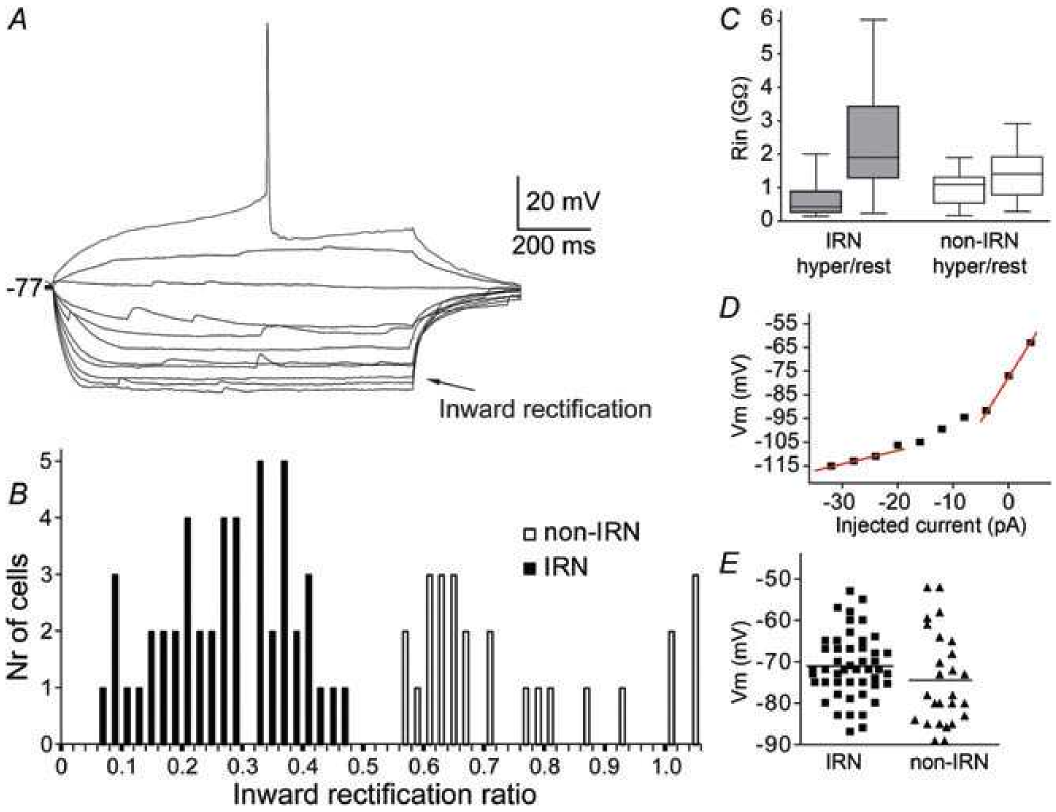

Figure 2. Properties of IRNs and distribution of parameters of both IRNs and non-IRNs
A, voltage responses of an IRN to hyperpolarising and depolarising 1 s current steps of 4 pA per step, elicited from rest at −77 mV. Inward rectification is seen as relatively small voltage responses at hyperpolarised potentials (arrow) with each step and increasingly larger responses at more depolarised levels. The rectification ratio is 0.34. B, histogram of the inward rectification ratio for all neurons. Neurons with ratio below 0.5 form a population defined as IRNs and those above 0.5 as non-IRNs. C, plot of the input resistance (Rin) of IRNs and non-IRNs, measured at a hyperpolarised potential (−120 mV) and at resting membrane potentials. D, I–V plot of the steady-state voltage deflections to current steps of the neuron displayed in A. Note the steeper slope at more depolarised potentials. E, distribution of the resting membrane potentials of recorded neurons.

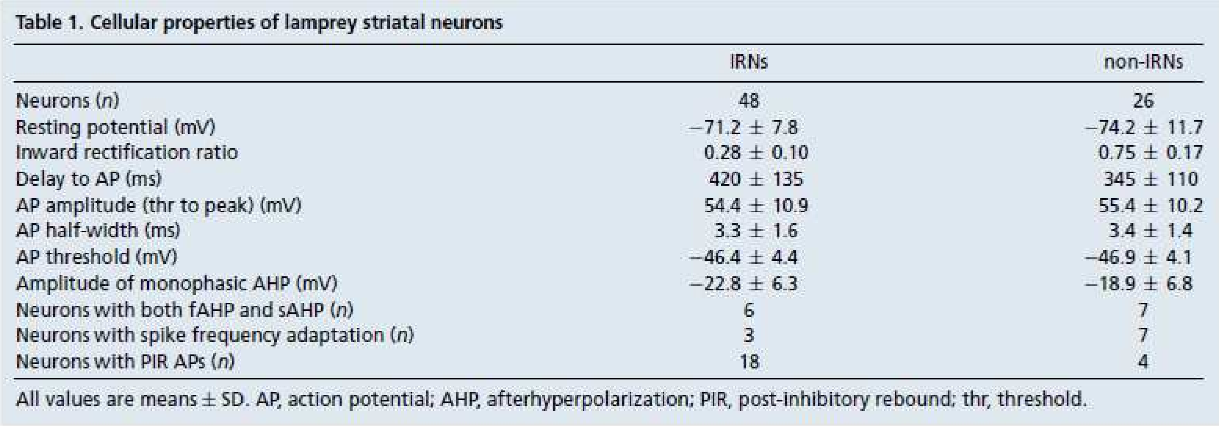
Table 1. Cellular properties of lamprey striatal neurons

	IRNs	non-IRNs
Neurons (*n*)	48	26
Resting potential (mV)	−71.2 ± 7.8	−74.2 ± 11.7
Inward rectification ratio	0.28 ± 0.10	0.75 ± 0.17
Delay to AP (ms)	420 ± 135	345 ± 110
AP amplitude (thr to peak) (mV)	54.4 ± 10.9	55.4 ± 10.2
AP half-width (ms)	3.3 ± 1.6	3.4 ± 1.4
AP threshold (mV)	−46.4 ± 4.4	−46.9 ± 4.1
Amplitude of monophasic AHP (mV)	−22.8 ± 6.3	−18.9 ± 6.8
Neurons with both fAHP and sAHP (*n*)	6	7
Neurons with spike frequency adaptation (*n*)	3	7
Neurons with PIR APs (*n*)	18	4

All values are means ± SD. AP, action potential; AHP, afterhyperpolarization; PIR, post-inhibitory rebound; thr, threshold.

2.2.1 Inwardly rectifying neurons

Basic electrophysiological properties.

IRNs displayed a characteristic voltage response due to inward rectification, hyperpolarised resting membrane potentials and a ramping response to depolarising current injections resulting in a long delay to the first action potential. Figure 2A shows the typical appearance of an IRN with an inward rectification ratio of 0.34, with an overall mean ratio for the IRN population of 0.28±0.10, ranging from 0.07 to 0.45 (Fig. 2B). Many cells (25%) displayed very strong rectification (ratio <= 0.20). The input resistancewas much lower at hyperpolarised membrane potential levels than at rest within the IRN population (Fig. 2C). The strongest rectification was normally seen below .90 mV, similar to findings in rodents although not as pronounced (Kawaguchi et al. 1989; Jiang & North, 1991; Cepeda et al. 2008).The steady state I.V curve in Fig. 2Dshows the characteristic difference in slope between hyperpolarised and more depolarised membrane potential levels, as is evident also from the current steps in Fig. 2A. IRNs had a mean resting potential of -71.2±7.8mV, with 65% of the neurons having values between -70 mV and -87 mV (see Fig. 2E for distribution). Most IRNs (87.5%) displayed a monophasic AHP (Fig. 3A). The mean size of the monophasic AHP for IRNs was -22.8±6.3mV, as measured with reference to the threshold of the action potential, rather than the resting membrane potential. The voltage dependence of the monophasic AHP is illustrated in Fig. 3A. The size of the AHP was increased upon depolarisation and was reversed at levels around -75 to -80 mV, indicating that the underlying current was a K+ current. The time to peak of the AHP was variable (Fig. 3B) with a mean of 30.5±19.9ms for the neurons with monophasic AHPs. Six IRNs (12.5%) displayed a biphasic AHP with the time to the second maximum ranging from 41ms to 170 ms, and with a mean of 89.8±45.7ms. The mean amplitude of the slow AHP (sAHP) was -15.8±5.0mV. The time to the peak of the fast AHP (fAHP) component was 9.1±4.0ms. Half of these neurons showed a marked spike frequency adaptation with comparable properties to the neuron displayed in Fig. 6G.

Seventy per cent of IRNs showed reliable and regular spiking with a limited spike frequency adaptation during sustained current injections (Fig. 3C and D), while the other 30% of neurons had some broadening of action potentials, firing failure at depolarised levels and sometimes irregular firing patterns. Action potentials had a threshold of -46.4±4.4mV, a half-width of 3.3±1.6ms and amplitude of 54.4±10.9mV (see Table 1). Fifty per cent of IRNs could discharge at frequencies of 15 Hz or above for a sustained period and a few (6%) up to at least 50Hz. Most neurons appeared to saturate at their maximum firing frequencies, while the remainder showed action potential inactivation at further depolarisation. Some of the IRNs showed a time and voltagedependent sag in their response to hyperpolarising current steps (Fig. 4D), contributing with a time-dependent component of the inward rectification. The sag was estimated by a sag index (see Methods), as exemplified by the cell in Fig. 4D with a sag index of 0.31. Only a minority (33%) of the IRNs (Fig. 4F), however, had a sag index 0.2 or above, a value not reached by any of the non-IRNs. The sag was most pronounced at hyperpolarised potentials and in many of these neurons it was not visible at voltages more depolarised than at−85mV.At the termination of the hyperpolarising steps that were elicited from rest, a post-inhibitory rebound (PIR) depolarisation with spiking occurred (Fig. 4*D*) in 60% of these neurons with a sag index of 0.2 or larger. The larger the hyperpolarising steps, the greater the PIR depolarisation and the number of action potentials generated (up to 8 action potentials). PIR spikes could, however, also be elicited in a subset of IRNs without a sag when the hyperpolarising pulses were injected from depolarised baselines around−60mVbut not at the more hyperpolarised resting state.

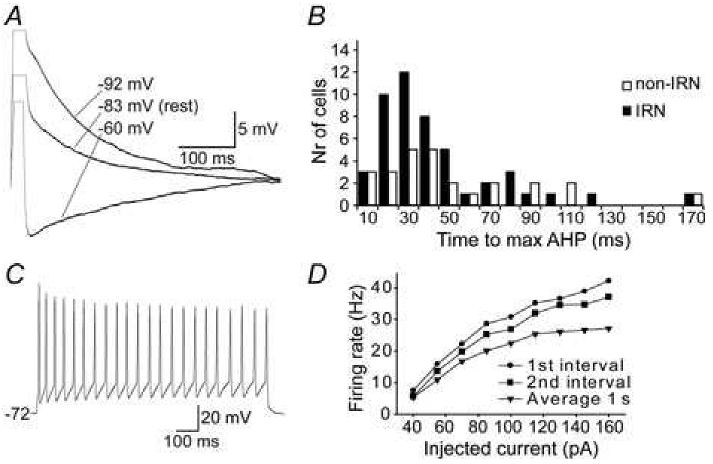

Figure 3. Afterhyperpolarisation (AHP) and firing properties of IRNs

A, the AHP of an IRN following the action potential elicited by a 5 ms positive current pulse. The AHP is shown at three different baseline potentials (−60, −83 and −92 mV), achieved by continuous current injections, to reveal the voltage dependence of the AHP. The AHP is reversed between −60 mV and −83 mV. B, frequency histogram of the time to maximum AHP for IRNs (black) and non-IRNs (white). C, response to suprathreshold current injections, showing the firing properties of the neuron in A. D, plot of firing rate as a function of the injected current during a 1 s current pulse in the neuron in C. The round markers indicates the instantaneous frequency of the first interval in the elicited train of action potentials and the squares the second interval. The triangles show the average firing frequency over the entire train of action potentials.

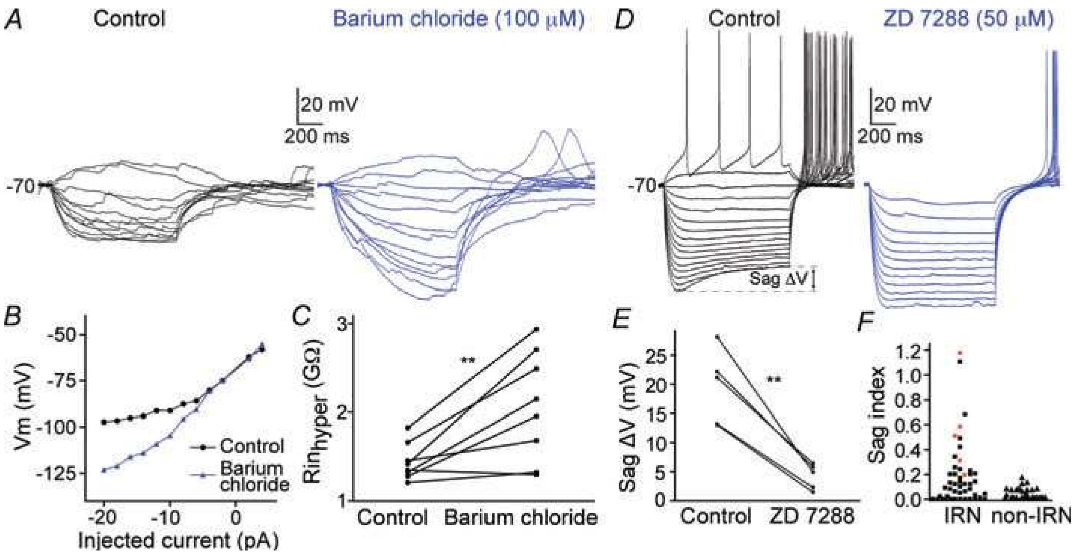

Figure 4. Pharmacological analyses of Kir and Ih in IRNs

A, voltage responses of an IRN before (left) and during bath application of barium chloride (right) that blocks Kir-channels. B, I–V plot of the cell in A, that shifts from being upwardly concave (control) to a close to straight line (barium chloride). C, the input resistance at hyperpolarised potentials is increased during Ba2+ application. D, the left voltage traces shows an IRN that also displays an Ih-induced sag (see Sag ΔV) with a sag index of 0.31, followed by a post-inhibitory rebound with action potentials at the end of the hyperpolarising current steps. Under control conditions (left) the Ih sag is seen clearly at hyperpolarised levels while bath application of the Ih antagonist ZD 7288 almost completely removes the sag (right). E, the sag is reduced after application of ZD 7288 (50 µM, n = 5). F, plot of the sag index for each IRN and non-IRN. The paler squares indicate the neurons in which ZD 7288 was applied.

Pharmacological analysis of inward rectification in IRNs.

The Kir channels have been investigated in different species and cell types, including rat dorsal and ventral striatal cells, and they are known to be blocked by extracellular barium chloride at 100 μM (Standen & Stanfield, 1978; Uchimura *et al.* 1989; Nisenbaum & Wilson, 1995). Through bath application of barium chloride at this concentration, we show that the inward rectification is significantly reduced at subthreshold levels (Fig. 4A–C, n =8). Figure 4A shows an IRN before and during Ba2+ application,with increased voltage deflections between each current stimulation and prolonged time-constants. The I–V relationship (Fig. 4B) changes from an upwardly concave curve to an almost straight line, reflecting a near constant input resistance below rest after the blockade with Ba2+. The effect of Ba2+ was quantified by comparing the input resistance at hyperpolarised potentials (around −110 mV) before and during barium and it increased significantly from 1.44±0.2 GΩto 2.06±0.6 GΩ(P <0.01, n =8; Fig. 4C).

The degree of rectification was associated with the change in input resistance, so that neurons with less rectification showed less change and the one neuron in Fig. 4C that did not increase its input resistance was also clearly defined as a non-IRN based on its inward rectification ratio (0.93). The application of Ba2+ was also accompanied by a depolarisation of neurons by 5–10mV.

The effect of Ba2+ on the inward rectification in striatal neurons suggest that it is due to Kir-channels, and thus also due to a K+ conductance.

Pharmacological analyses of Ih and A-type K+ current contribution to IRNs.

One-third of the IRNs had a voltage-dependent sag (Fig. 4D and F) that was examined by bath application of 50 µM ZD 7288, an antagonist of the monovalent cation current Ih known to cause a voltage sag in other neurons (Harris & Constanti, 1995). Following ZD 7288 application, the sag decreased markedly from 19.5±6.4mV to 4.3±2.2mV (P <0.01, n =5; Fig. 4D and E). Figure 4D also shows that the inward rectification was reduced but maintained at a lower level after application of ZD 7288. In one neuron, Ba2+ was added 10 min following application of ZD 7288, effectively removing all inward rectification (data not shown). ZD 7288 also affected the PIR depolarisation and the accompanying action potentials. The time to the first rebound action potential increased from104±24 ms to 235±48 ms (P <0.05, n =4), and the number of rebound action potentials was reduced by 1–4 action potentials (Fig. 4D). These data clearly indicate that the sag is mediated by activation of an Ih current and partly also the accompanying PIR. The characteristic ramping response and long delay to the first action potential in rat MSNs is mainly due to activation of a low-voltage-activated K+ current, IA, activated at subthreshold membrane potentials and that inactivates after hundreds of milliseconds (Surmeier et al. 1991; Nisenbaum & Wilson, 1995; Shen et al. 2004). In lamprey, as well as mammals, this A-type K+ current is selectively depressed at low concentrations of 4-AP (100 µM), while high concentrations also reduce the high-voltage-activated A-type K+ current (Rogawski et al. 1985; Surmeier et al. 1991; Nisenbaum & Wilson, 1995; Hess & El Manira, 2001). During investigation of the low-voltage-activated A-type K+ channels, neurons were held at very hyperpolarised levels to ensure that these channels were not voltage inactivated before the depolarising steps were given (Fig. 5A). 4-AP reduced the time delay to the first action potential (Fig. 5A and B) at a concentration of both 100 µM (P <0.05, control: 518±93 ms; 100 µM: 211±8ms, n =3) and 500 µM (P <0.01, control: 522±84 ms; 500 µM: 234±47 ms, n =5). Similar results were obtained through voltage inactivation of the A-type K+ current by membrane depolarisation before current injections (Fig. 5C and D). The delay to the first action potential was reduced from 460±92 ms to 151±99 ms by changing the baseline membrane potential from−90 mV to −60 mV (P <0.01, n =5). It should be noted, however, that the long delays to first spike are present at rest in neurons (Fig. 2A and Table 1). These results suggest that an A-type K+ current contributes to the ramping response with a long delay to the first spike, upon a depolarisation from a hyperpolarised level.

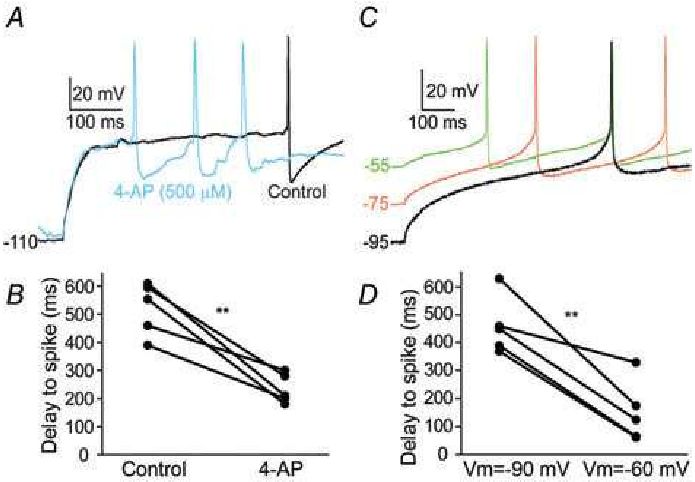

Figure 5. Pharmacological analyses of the A-type K+ current contribution to IRNs

A, voltage response to the first depolarising current step that elicits an action potential (black line, control) displaying the long delay to first action potential. During bath application of the IA antagonist 4-AP at 100 and 500 μM action potentials are evoked after a much shorter delay. Data only shown for 500 μM. B, the time delay to the first action potential is reduced by several hundred milliseconds by 4-AP (500 μM, n = 5). C, the ramping response to first spike is also reduced by eliciting action potentials from different baseline potentials. The more depolarised baseline potential (from lower to middle to upper traces), the shorter th time-delay to first action potential. D, at −60 mV, th time delay to first action potential is significantly shorter than at −90 mV (n = 5).

Synaptic input to IRNs.

Lamprey striatal neurons receive glutamatergic spontaneous synaptic input (Ericsson *et al.* 2007). We show that striatal neurons also receive a continuous GABAergic input (Fig. 6*A* and *B*). Application of the GABAA receptor blocker gabazine (40 μM) strongly reduced the spontaneous input (*P* <0.01, control: 5.48±1.61 Hz; gabazine: 2.48±1.36 Hz, *n* =5). Further application of NBQX (40 μM) blocked almost all of the remaining synaptic input (*P* <0.01, gabazine: 2.48±1.36 Hz; NBQX+gabazine: 0.10±0.17 Hz, *n* =5). To facilitate the detection ofGABAergic input at the resting membrane potential, these experiments were performed with an intracellular solution containing 30mM chloride, thus shifting the reversal potential for GABAA responses to a predicted value around −35 mV.

2.2.2. Non-inwardly rectifying neurons

Basic electrophysiological properties.

Non-IRNs represent a somewhat heterogeneous group (n = 26) and are defined as having a rectification ratio larger than 0.5 (0.75 ± 0.17, ranging from 0.56 to 1.05, see Fig. 2B), and I–V traces with a close to linear relationship (Fig. 7A and B). The mean resting membrane potential was −74.2 ± 11.7 mV (Table 1), and 69% of the neurons had resting potentials below −70 mV (Fig. 2E). Most neurons demonstrated long delays to the first action potential (345± 110 ms) with amplitudes of 55.4 ± 10.2 mV (Table 1). The action potential threshold was −46.9 ± 4.1 mV and the half-width 3.4 ± 1.4 ms. When the non-IRNs are taken as a group there are, except for the rectification ratio and the lack of Ih (Fig. 4F), no prominent differences in cellular properties compared to IRNs (see Table 1). One subgroup of non-IRNs displayed a fast monophasic AHP following the action potential (69%; Fig. 7C), while the other exhibited a biphasic AHP (Fig. 7F). The average time to peak of the monophasic AHP (Fig. 7C) was 29.4±16.4ms, and the amplitude −18.9±6.8mV, as estimated from the threshold of the action potential. The monophasic AHP reversed at the same membrane potential level as in IRNs, i.e. around −75 to −80 mV (Fig. 7C). Seventy-three per cent of non-IRNswith monophasic AHPs showed regular spiking with action potential frequencies ranging from 15 to 40Hz with limited spike frequency adaptation. Three of the neurons with a monophasic AHP appeared to represent a separate subcategory of non-IRNs. They displayed significantly shorter times to peak AHP (8.3±3.2ms), narrow action potentials (1.75±0.06 ms, cf. Table 1) and high frequency spiking up to 60 Hz with very modest spike frequency adaptation, as measured over 1 s, and over 80Hz for the first interval (example in Fig. 7D and E). In addition, two of these neurons had very low input resistance, both at hyperpolarised potentials (340±70M┐) and at rest (490±7M┐). The non-IRNs that displayed biphasic AHPs (27%, Fig. 7F) had a time to the second peak of 90.4±42.1ms (Fig. 3B) with an amplitude of −17.4±3.6mV. The time to the fAHP component was 10.3±4.3ms. The majority of these neurons showed a marked spike frequency adaptation (Fig. 7G and H), and a frequency range from 10–30 Hz.

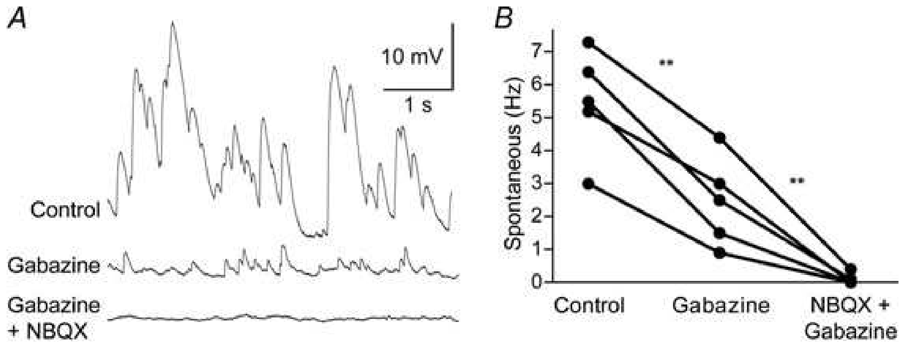

Figure 6. Spontaneous synaptic input to IRNs
A, current clamp recordings of spontaneous synaptic input at −85 mV. The upper trace shows synaptic input during control conditions, the second during bath application of the GABAA receptor antagonist gabazine (40 μM) and the third during bath application of gabazine and the AMPA receptor antagonist NBQX (40 μM) simultaneously. B, gabazine significantly reduces the spontaneous synaptic input and additional application of NBQX almost completely blocks all spontaneous synaptic input. All spontaneous synaptic input recordings were performed with intracellular solutions containing moderate concentrations of Cl− so that GABAergic input is reversed at more depolarised potentials (theoretically around −35 mV).

2.2.3. Morphology and topography

Morphological properties.
A total of 12 IRNs and 12 non- IRNs were labelled. There was no apparent difference in somatic characteristics of IRNs and non-IRNs as both had fusiform or spherical shapes. The somata diameters ranged from8 to 15 μm and the cell bodies were located within the striatal cell band or just lateral to the cell band where substance P expressing striatal neurons are located (Fig. 8A–E; Nozaki & Gorbman, 1986). Most labelled neurons (8 IRNs and 8 non-IRNs) had two major processes that extended in opposite directions diagonally from the soma (see for example Fig. 8B and C), while the rest had either three to five processes or only one process. Each neuron generally had one thinner, uniform process and one thicker process with a broad base of 2–3 μm that gradually became thinner and progressed with a thickness of 0.5–1 μm. The thin processes are putative axons that originated either directly from the soma or by branching off in a right angle

from the base of a proximal dendrite. These processes were difficult to follow due to their thin diameters. Most of our reconstructions within the coronal plane probably represent dendrites, based on their non-uniform thickness and oblique branching. Figure 8F shows original confocal reconstructions, including the two non-IRNs in Fig. 8C, demonstrating themoderate branching exhibited by some cells. Many processes, especially those in the area between the striatum and the ventricle, had varicosities about 2µm apart from each other. Neurons in the lamprey striatum have been described to have dendritic spines (Pombal et al. 1997b). Figure 8G shows an overview of a spiny IRN located in the caudal striatum, visualised with DAB staining. The spiny dendritic process is shown in close-up in Fig. 8H.

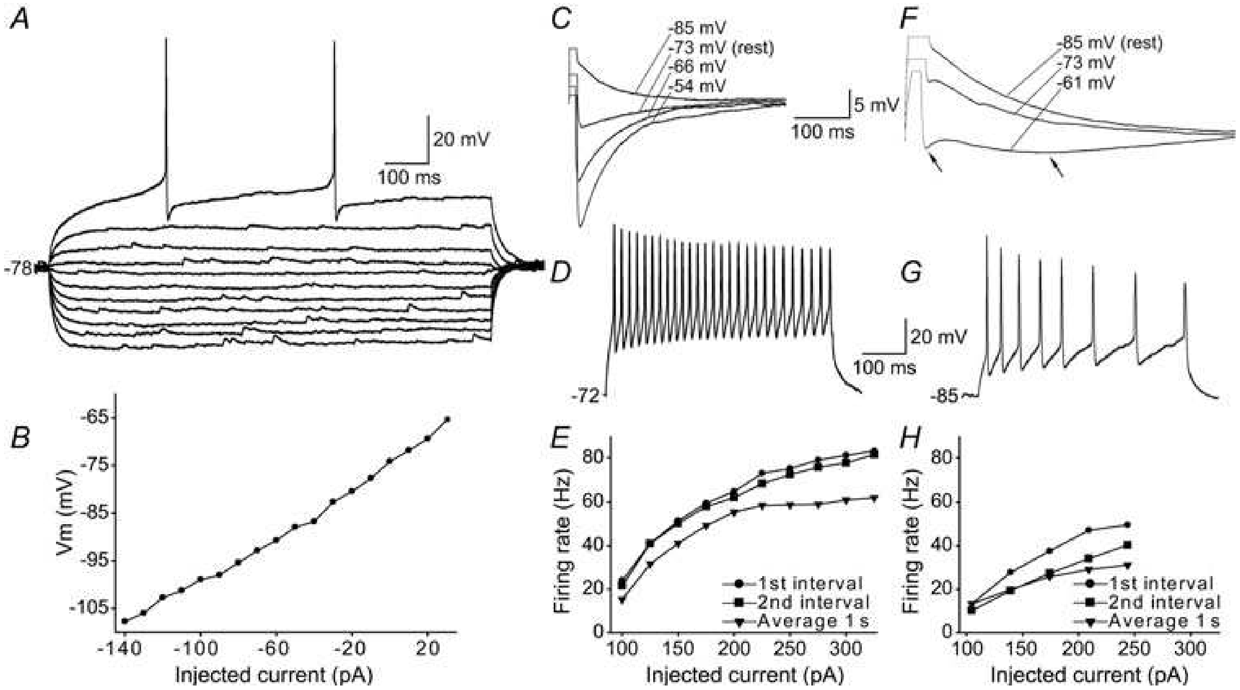

Figure 7. Properties of non-IRNs

A, voltage responses of a non-IRN to hyperpolarising and depolarising 1 s current steps of 10 pA per step, elicite from rest at −78 mV. The displayed neuron lacks inward rectification with a rectification ratio of 0.78 and also lacks any obvious sag. B, I–V plot of the steady-state voltage deflections to current steps of the neuron displayed in A showing close to a linear relationship. C, monophasic afterhyperpolarisation (AHP) response after an action potential elicited by a 5 ms positive current injection. The voltage dependence of the AHP is shown by recordings at four different baseline potentials. The reversal of the AHP takes place between −73 and −85 mV in this neuron Scale bar for both panels C and F. D, response to suprathreshold current injections in another non-IRN with large, fast AHP showing its firing properties. Same scale bar for panels D and G. E, plot of firing rate as a function of the injected current during a 1 s current pulse of the neuron in D. The round markers shows the instantaneous frequency of the first interval in the train of action potentials, the squares the second interval and the triangles the average firing frequency over the entire train of action potentials. This cell also had low input resistance (Rin,hyper = 290 MΩ, Rin,rest = 380 MΩ) compared to lamprey striatal neurons in general (compare to Fig. 3A). F, voltage recording of another non-IRN showing a biphasic AHP (arrows) response after the action potential, shown at three different baseline potentials. G, response to suprathreshold current injections in a neuron with biphasic AHP showing spike frequency adaptation. H, plot of firing rate as a function of the injected current of the neuron above.

Another spiny dendrite, visualised by confocal microscopy, is displayed in Fig. 8*I*. Spines appeared as thin, short stubs extending from the dendrite or as bulbs located directly on the dendritic shaft. All spiny dendrites were IRNs and they were always distal dendrites but not in perisomatic domains. We could not confirmthat spineswere present in all IRNs, even when well stained. This may possibly relate to the orientation of the distal dendrites in the striatal slices.

Projections of IRNs and non-IRNs.

IRNs located in the rostral striatum had relatively short projections in the coronal plane (Fig. 8*A* and *B*). Instead, most of these processes turned in a perpendicular direction after 50–150 μm and continued in the rostrocaudal direction (*n* =6/7) towards the pallidal regions of the lamprey (Ericsson *et al.* 2010). However, IRNs located more caudally (Fig. 8*D*) sent longer processes (up to 250 μm) within the same coronal plane and with more branching and two of these IRNs had processes that also projected rostrocaudally. IRNs extended processes towards both the medial telencephalic ventricle and the medial and lateral pallium (Fig. 8*A–D*) within the coronal plane.

The processes of non-IRNs were mainly distributed within the coronal plane and only one neuron had a clear rostrocaudal projection. Many processes were long (300–700 μm) and in nine neurons they approached or reached into the lateral and ventrolateral pallium.

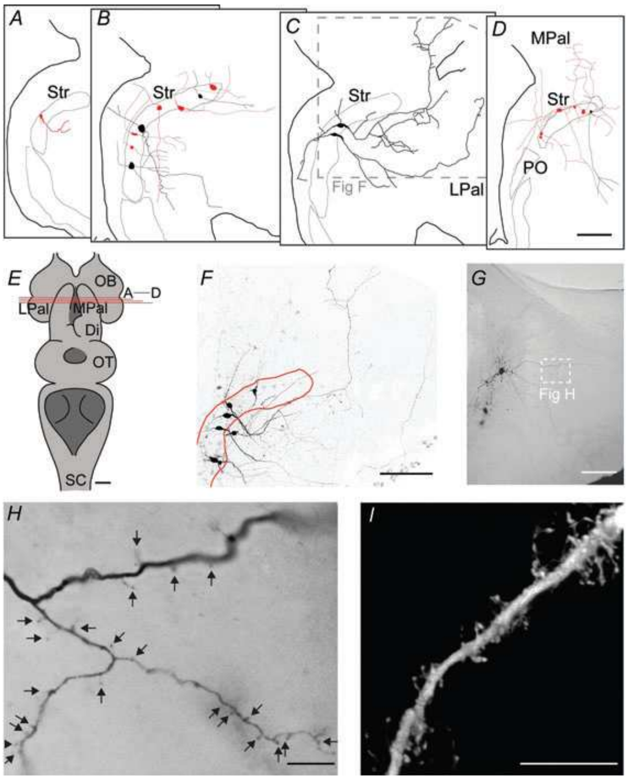

Figure 8. Morphology and topography of striatal neurons

A–D, schematic representations of IRNs (pale) and non-IRNs (black), in sections from rostral to caudal according to E. E, overview of the lamprey brain, including the level of coronal sectioning shown in A–D. F, confocal image showing the morphological properties of the two non-IRNs shown in C, among 4 other labelled but unrecorded neurons. See inset in C for the location in the coronal section. G, overview of a spiny IRN by light microscopy of a DAB-stained slice. H, close-up of spiny dendrites in the IRN shown in G, according to white inset. I, confocal image of another spiny dendrite labelled in the striatum. Scale bars = 100 μm in A–D, F and G; 1mm in E; 10 μm in H and I. Abbreviations are as follows: Di, diencephalon; LPal, lateral pallium; MPal, medial pallium; OB, olfactory bulb; PO, nucleus preopticus; OT, optic tectum; Str, striatum.

Comparison of IRNs to neurons of other vertebrates

IRNs share many of the intrinsic properties of mammalian MSNs, i.e. a fast inward rectification due to Kir-channels, hyperpolarised resting membrane potentials and a long delay to the first action potential due to activation of the low-voltage-activated A-type K+ current (Rogawski et al. 1985; Kawaguchi et al. 1989; Jiang & North, 1991; Nisenbaum & Wilson, 1995; Shen et al. 2007). The majority of lamprey IRNs (65%) exhibit inward rectification due only to Kir. These IRNs may serve a similar function as in mammals, where it contributes to maintain MSNs at hyperpolarised potentials until Kir-channels close upon strong excitatory input (Wilson & Kawaguchi, 1996; Stern et al. 1998; Grillner et al. 2005). Interestingly, however, around one-third of the IRNs also exhibits a large Ih-induced sag that increases the conductance at hyperpolarised potentials further and amplifies their inward rectification ratio. This subpopulation of IRNs clearly differs from rodent MSNs. Hyperpolarising current steps often triggered post-inhibitory rebound action potentials in this group of IRNs (see Fig. 4A). Potentially, a synchronised barrage of inhibitory activity limited in duration may elicit PIR spikes and thereby output from the striatum.

We show that striatal neurons receive both GABAergic and glutamatergic input, and it seems likely that the former is provided by local GABAergic microcircuits since the striatum contains almost exclusively GABAergic neurons (Robertson et al. 2007). The glutamatergic input presumably originates from the thalamostriatal or the lateral and medial palliostriatal fibres (Pombal et al. 1997a; Northcutt & Wicht, 1997). In experiments where the synaptic input was blocked, the resting potential did not change markedly, indicating that it was not significantly influenced by the synaptic input. Once depolarised, the input resistance of IRNs was shown to increase to high values with a mean of 2400MΩ, as compared to rodent MSNs with maximum input resistances around 600MΩ depending on the preparation (Kawaguchi, 1993; Tepper et al. 2004; Cepeda et al. 2008). This difference may be related to the small size of lamprey neurons, but also to the distribution and density of ion channels. Inward rectification in rodents appears more pronounced than in lamprey, possibly due to a higher expression of Kir channels. In rodents, MSNs represent roughly 95% of the striatal neurons (Tepper et al. 2004) whereas only 65% of lamprey neurons are classified as IRNs. The population of IRNs, as defined here, may possibly be larger, as a fraction of non-IRNs have a ratio close to the dividing ratio of 0.5. Striatal neurons are known to project to an area close to eminentia thalami, containing GABAergic projection neurons that target the mesencephalic and dienchephalic locomotor regions (MLR and DLR), as well as tectum (M´enard et al. 2007; M´enard & Grillner, 2008; Robertson et al. 2007, 2009; Stephenson-Jones et al. 2010). This area is suggested to be homologous to that of the mammalian globus pallidus. Recent findings also show striatal projections to an area in the caudolateral tegmentum containing GABAergic neurons projecting to tectum (Robertson et al. 2009). New recordings from retrogradely labelled striatal projection neurons suggest that different subsets of IRNs project to the different output regions of the basal ganglia in lamprey (Ericsson et al. 2010), thus corresponding to striatal projections in other vertebrates, and showthat IRNs represent the striatal output neurons.

Comparison of non-IRNs to neurons of other vertebrates

In the mammalian striatum, only interneurons lack inward rectification (Tepper & Bolam, 2004). A subgroup of non-IRNs had properties similar to the mammalian parvalbumin-expressing fast spiking interneurons, characterised by fast-spiking frequencies, very low spike frequency adaptation, low input resistance, narrow action potentials and short delays to AHPs (Kawaguchi, 1993; Tepper & Bolam, 2004). Another subgroup was distinguished by their biphasic AHPs and marked spike frequency adaptation. The fast component of the AHP appears to be fairly similar in all lamprey striatal neurons and reversed around −75 to −80 mV. The main current mediating this AHP is likely to be the high-threshold transient A-type K+ current, which has been investigated in detail in the lamprey spinal cord (Hess & El Manira, 2001; Cangiano *et al.* 2002). The second, slower component seen in some neurons shows similar properties to the slow AHP in lamprey spinal neurons, due primarily to apamin-sensitive calcium-dependent K+ channels (Cangiano *et al.* 2002) with a residual 20% mediated by a Slack-like subtype of sodium-dependent K+ channel (Wall´en *et al.* 2007). The morphological data of non-IRNs showed that many of their dendritic processes are within the coronal plane where their cell bodies are located. However, we assume that non-IRNs and especially those resembling the fast-spiking type neurons represent interneurons. Few afferents to the striatum actually innervate the cell layer (Pombal *et al.* 1997*b*) and rather target the periventricular neuropil or the area between the striatal cell layer and the lateral pallium. It thus seems likely that the dendrites of putative interneuronswould not respect the boundaries of the cell layer.Although the presumed axons of these cells were too thin to be traced in order to confirm that they only contact other striatal neurons, the results discussed above (e.g. Ericsson *et al.* 2010) with all output neurons identified as IRNs, further strengthen the possibility that they are interneurons. In the lamprey striatum there is a pronounced acetylcholinesterase activity and cells have been found to express choline acetyltransferase immunoreactivity (Pombal *et al.* 1997*b*, 2001), suggesting the presence of cholinergic neurons. In rodents, large aspiny cholinergic interneurons represent around1%of the striatal cell population (Rymar *et al.* 2004). In the present sample of cells (*n* =74), no neurons could clearly be identified as cholinergic cells.

Concluding remarks

Our data further strengthen previous findings suggesting that the basic properties of the striatal neurons had already been developed early in vertebrate evolution, before the lamprey diverged from the main vertebrate line around 560 million years ago. Lamprey striatal neurons express some of the hallmarks of mammalian striatal neurons, including inward rectification due to Kir channels. About one-third of these neurons also display *I*h-mediated voltage sags, whichwould ascertain that after an inhibitory hyperpolarisation there will be an *I*h depolarisation that is often accompanied by PIR spikes. These characteristics may be unique to non-mammalian species. This study is the first detailed electrophysiological study of the striatal cell properties in anamniotes and indicates that the principal neuronal type and the fast-spiking interneuron were present some 250–300 million years before the anamniote–amniote transition. Thus, the basic design of the striatum and the basal ganglia circuitry implied in decision-making and action selection of motor behaviour are present even in the less evolved lamprey, supporting a limited behavioural repertoire.

2. 4 References

1. Auclair F, Lund J & Dubuc R (2004). Immunohistochemical distribution of tachykinins in the CNS of the lamprey Petromyzon marinus. *J Comp Neurol* **479**, 328–346.
2. Barral J, Galarraga E, Tapia D, Flores-Barrera E, Reyes A & Bargas J (2010). Dopaminergic modulation of spiny neurons in the turtle striatum. *Cell Mol Neurobiol* **30**, 743–750.
3. Brodin L, Hokfelt T, Grillner S & Panula P (1990*a*). Distribution of histaminergic neurons in the brain of the lamprey *Lampetra fluviatilis* as revealed by histamineimmunohistochemistry. *J Comp Neurol* **292**, 435–442.
4. Brodin L, Theordorsson E, Christenson J, Cullheim S, H¨okfelt T, Brown J, Buchan A, Panula P, Verhofstad A & GoldsteinM (1990*b*). Neurotensin-like peptides in the CNS of lampreys: chromatographic characterization and immunohisto chemical localization with reference to aminergic markers. *Eur J Neurosci* **2**, 1095–1109.

5. Cangiano L,Wall´en P & Grillner S (2002). Role of apaminsensitive KCa channels for reticulospinal synaptic transmission to motoneuron and for the afterhyperpolarization. *J Neurophysiol* **88**, 289–299
6. Cepeda C, Andr´e V, Yamazaki I,Wu N, Kleiman-Weiner M & Levine M (2008). Differential electrophysiological properties of dopamine D1 and D2 receptor-containing striatal medium-sized spiny neurons. *Eur J Neurosci* **27**, 671–682.
7. Ericsson J, Robertson B &Wikstrom MA (2007). A lamprey striatal brain slice preparation for patch-clamp recordings. *J Neurosci Methods* **165**, 251–256.
8. Ericsson J, Stephenson-Jones MR, Samuelsson E, Robertson B, Hill R, Hellgren J & Grillner S (2010). The lamprey provides a vertebrate blueprint of the mammalian basal ganglia. Meeting abstract, 142.8, Federation of European Neuroscience Societies Forum.
9. Farries MA & Perkel DJ (2000). Electrophysiological properties of avian basal ganglia neurons recorded in vitro. *J Neurophysiol* **84**, 2502–2513.
10. Grillner S, Hellgren J, Menard A, Saitoh K &Wikstrom MA (2005). Mechanisms for selection of basic motor programs – roles for the striatum and pallidum. *Trends Neurosci* **28**, 364–370.
11. Grillner S,Wallen P, Saitoh K, Kozlov A & Robertson B (2008). Neural bases of goal-directed locomotion in vertebrates – an overview. *Brain Res Rev* **57**, 2–12.
12. Harris NC & Constanti A (1995). Mechanism of block by ZD 7288 of the hyperpolarization-activated inward rectifying current in guinea pig substantia nigra neurons in vitro. *J Neurophysiol* **74**, 2366–2378.
13. Hess D & El Manira A (2001). Characterization of a highvoltage- activated IA current with a role in spike timing and locomotor pattern generation. *Proc Natl Acad Sci U S A* **98**, 5276–5281.
14. Jiang ZG & North RA (1991). Membrane properties and synaptic respo Jimenez AJ, Mancera JM, Pombal MA, Perez-Figares JM & Fernandez-Llebrez P (1996). Distribution of galanin-like
15. immunoreactive elements in the brain of the adult lamprey *Lampetra fluviatilis*. *J Comp Neurol* **368**, 185–197.
16. Kawaguchi Y (1993). Physiological, morphological, and histochemical characterization of three classes of interneurons in rat neostriatum. *J Neurosci* **13**, 4908–4923.
17. Kawaguchi Y,Wilson CJ & Emson PC (1989). Intracellular recording of identified neostriatal patch and matrix spiny cells in a slice preparation preserving cortical inputs. *J Neurophysiol* **62**, 1052 1068.
18. M´enard A & Grillner S (2008). Diencephalic locomotor region in the lamprey – afferents and efferent control. *J Neurophysiol* **100**, 1343–1353.
19. M´enard A, Auclair F, Bourcier-Lucas C, Grillner S & Dubuc R (2007). Descending GABAergic projections to the mesencephalic locomotor region in the lamprey *Petromyzon marinus*. *J Comp Neurol* **501**, 260–273.
20. Nisenbaum ES &Wilson CJ (1995). Potassium currents responsible for inward and outward rectification in rat neostriatal spiny projection neurons. *J Neurosci* **15**, 4449–4463.
21. Northcutt RG &Wicht H (1997). Afferent and efferent connections of the lateral and medial pallia of the silver lamprey. *Brain Behav Evol* **49**, 1–19.
22. Nozaki M & Gorbman A (1986). Occurrence and distribution of substance P-related immunoreactivity in the brain of adult lampreys, *Petromyzon marinus* and *Entosphenus*
23. *tridentatus*. *Gen Comp Endocrinol* **62**, 217–229.
24. Olsen BD (2007). Understanding biology through evolution, 3rd edn, Vol. 25, p. 149.

25. Pombal MA, El Manira A & Grillner S (1997*a*). Afferents of the lamprey striatum with special reference to the dopaminergic system: a combined tracing and immunohistochemical study. *J Comp*
26. *Neurol* **386**, 71–91.
27. PombalMA, ElManira A & Grillner S (1997*b*). Organization of the lamprey striatum – transmitters and projections. *Brain Res* **766**, 249–254.
28. Pombal MA, Marin O & Gonzalez A (2001). Distribution of choline acetyltransferase-immunoreactive structures in the lamprey brain. *J Comp Neurol* **431**, 105–126.
29. Redgrave P, Gurney K, Reynolds J (2008).What is reinforced by phasic dopamine signals? *Brain Res Rev* **58**, 322–339.
30. Robertson B, Auclair F, M´enard A, Grillner S & Dubuc R (2007). GABA distribution in lamprey is phylogenetically conserved. *J Comp Neurol* **503**, 47–63.
31. Robertson B, Jones M, Samuelsson E, Hill R, Hellgren J & Grillner S (2009). The lamprey basal ganglia – a vertebrate blue-print. Meeting abstract, 566.10, Society for Neuroscience.
32. Robertson B, Stephenson-Jones MR, Ericsson J, Diaz Heijtz R & Grillner S (2010). The direct and indirect pathways of lamprey basal ganglia. Meeting abstract, 220.2, Federation of European Neuroscience Societies Forum.
33. Rogawski MA, Beinfeld MC, Hays SE, Hokfelt T & Skirboll LR (1985). Cholecystokinin and cultured spinal neurons. Immunohistochemistry, receptor binding, and neurophysiology. *Ann N Y Acad Sci* **448**, 403–412.
34. Rymar VV, Sasseville R, Luk KC & Sadikot AF (2004). Neurogenesis and stereological morphometry of calretininimmunoreactive GABAergic interneurons of the neostriatum. *J Comp Neurol* **469**, 325–339.
35. ShenW, Hernandez-Lopez S, Tkatch T, Held JE & Surmeier DJ (2004). Kv1.2-containing K+ channels regulate subthreshold excitability of striatal medium spiny neurons. *J Neurophysiol* **91**, 1337–1349.
36. Shen W, Tian X, Day M, Ulrich S, Tkatch T, Nathanson NM & Surmeier DJ (2007). Cholinergic modulation of Kir2 channels selectively elevates dendritic excitability in striatopallidal neurons. *Nat Neurosci* **10**, 1458–1466.
37. Standen NB & Stanfield PR (1978). A potential and time-dependent blockade of inward rectification in frog skeletal muscle fibres by barium and strontium ions. *J Physiol* **280**, 161–191.
38. Stephenson-Jones M, Samuelsson E, Ericsson J, Robertson B & Grillner S (2010). The core architecture of the basal ganglia – insights from evolution. Meeting abstract, P-64, International Basal Ganglia Society Meeting X.
39. Stern EA, Jaeger D &Wilson CJ (1998). Membrane potential synchrony of simultaneously recorded striatal spiny neurons in vivo. *Nature* **394**, 475–478.
40. Surmeier D, Ding J, Day M,Wang Z & ShenW(2007). D1 and D2 dopamine-receptor modulation of striatal glutamatergic signaling in striatal medium spiny neurons. *Trends Neurosci* **30**, 228–235.
41. Surmeier DJ, Stefani A, Foehring RC & Kitai ST (1991). Developmental regulation of a slowly-inactivating potassium conductance in rat neostriatal neurons. *Neurosci Lett* **122**, 41–46.
42. Tepper JM & Bolam JP (2004). Functional diversity and specificity of neostriatal interneurons. *Curr Opin Neurobiol* **14**, 685–692.
43. Tepper JM, Koos T &Wilson CJ (2004). GABAergic microcircuits in the neostriatum. *Trends Neurosci* **27**, 662–669.
44. Tepper J, Abercrombie E & Bolam J (2007). Basal ganglia macrocircuits. *Prog Brain Res* **160**, 3–7.

45. Thompson RH, M´enard A, Pombal M & Grillner S (2008). Forebrain dopamine depletion impairs motor behavior in lamprey. *Eur J Neurosci* **27**, 1452–1460.
46. Uchimura N, Cherubini E & North RA (1989). Inward rectification in rat nucleus accumbens neurons. *J Neurophysiol* **62**, 1280–1286.
47. Wall´en P, Robertson B, Cangiano L, Low P, Bhattacharjee A, Kaczmarek LK & Grillner S (2007). Sodium-dependent potassium channels of a Slack-like subtype contribute to the slow afterhyperpolarization in lamprey spinal neurons. *J Physiol* **585**, 75–90.
48. Wilson C & Kawaguchi Y (1996). The origins of two-state spontaneous membrane potential fluctuations of neostriatal spiny neurons. *J Neurosci* **16**, 2397–2410.

2.4.1 Author contributions

J.E. conducted the experiments and primary data analysis and developed the experimental design together with M.W., G.S. and S.G.; B.R. provided expertise in neuroanatomical C methods; all authors took part in the evaluation of the experimental data. J.E. wrote the manuscript in interaction with all authors, who also approved the final version of the manuscript.

2.4.2 Acknowledgements

This work was supported by the Swedish Research Council, HEALTH-F2-2008-201716 select-and-act, ICT-STREP 216100-LAMPETRA, and the Karolinska Institute. We are grateful to Dr Peter Wall´en for valuable comments on the manuscript.

3. Introduction: Evolutionary Conservation of the Basal Ganglia as a Common Vertebrate Mechanism for Action Selection

All animals must select actions to achieve their goals, but despite the common need, it is unclear whether animals employ common neural mechanisms for this function. In mammals, where action selection is well studied, a group of subcortical nuclei, the basal ganglia, are thought to play a pivotal role in this process by fulfilling a dual role in selection [1–4]. Direct striatal projections to the basal ganglia output nuclei (globus pallidus interna [GPi] and substantia nigra pars reticulata [SNr]) disinhibit various motor areas and thereby select actions. In contrast, indirect projections to these areas via intrinsic basal ganglia nuclei (globus pallidus externa [GPe] and subthalamic nucleus [STN]) serve to suppress actions by exciting the output nuclei and increasing the inhibition on the motor areas. Both pathways act together to select an action by disinhibiting a selected motor program and inhibiting other competing actions. Elements of this arrangement may represent a conserved mechanism for action selection because at least the input layer of this circuitry, the striatum, has been identified in all classes of vertebrates [5–7]. In contrast, it is unclear whether dedicated output (pallidal) structures are part of a conserved circuitry for selection, because they have not been identified in jawless vertebrates [5]. Developmental studies have even suggested that the pallidum is unlikely to exist in lamprey (a jawless vertebrate), because genes that are important for the development of the pallidum (Nkx2.1, shh) were not expressed in the embryonic ventral subpallium [8–10]. These studies, however, are inconclusive because they were performed at a developmental stage at which the forebrain GABAergic neurons, including potential pallidal neurons, were not yet present [11–15]. An even more recent evolutionary addition to the basal ganglia circuitry may have been the ‘‘indirect’’ pathway, as a mechanism for suppressing actions. Components of this pathway including the STN and the GPe have only been conclusively identified in advanced vertebrates, namely, avian and mammalian species [16–20]. Consequently, it is unclear whether lower vertebrates utilize a potentially simpler neural organization for selection, or whether features of the mammalian basal ganglia, such a the indirect pathway, are present in all vertebrates as essential components of a common circuitry for selection. Our aim was to use lamprey, which has a well-described motor system and a limited behavioral repertoire and occupies a key position in phylogeny, with their ancestors having diverged from the main vertebrate lineage at the dawn of vertebrate evolution approximately 560 million years ago (Mya) [21], to identify the basic circuitry for action selection and determine how this evolved to accommodate the increased behavioral repertoires of advanced vertebrates. Using anatomical and electrophysiological techniques, we show that a sequential theory for the evolution of the basal ganglia in vertebrates is likely to be wrong because all major components of the basal ganglia, including homologs of the mammalian GPi, GPe, and STN, together with direct and indirect pathways, are present in lamprey. Our results suggest that this architecture represented evolution’s blueprint for the vertebrate basal ganglia and may form the basis of action selection in all vertebrates. In addition, our results suggest that the mammalian basal ganglia evolved through a functional replication of these circuits, instead of a sequential adaptation, of this ancestral architecture.

3.1 Results

Anatomical and Electrophysiological Evidence for a Lamprey Pallidum

As the first step in elucidating whether dedicated output nuclei (pallidum) are a feature of the jawless vertebrate basal ganglia, we explored whether a putative pallidal area ventrolateral to eminentia thalami (Figure 1A), which contains GABAergic neurons that project to the tectum and other motor areas GPi and GPe. In mammalian species, the GPi and GPe contain GABAergic projection neurons that express the calciumbinding protein parvalbumin and receive input from both substance P- and enkephalin-expressing striatal medium spiny neurons [22].

Injections of neurobiotin, ventrolateral to the eminentiathalami, resulted in retrogradely labeled cells in the striatum (Figures 1B and 1C; n = 6), both within and surrounding the neuronally dense striatal band (Figure 1C). The complementary experiment with a tracer injected into the striatum (Figure 1D; n = 6) showed that striatal fibers project to this area, ventrolateral to the eminentia thalami, but do not pass further dorsally (Figure 1E). These fibers were small with varicosities, characteristic of fibers with synaptic contacts. Cells ventrolateral to the eminentia thalami expressed GABA and parvalbumin (Figure 1F, n = 5; Figure 1G, n = 4). Processes containing enkephalin and substance P, respectively, were also observed in this ventrolateral location and, as with the striatal fibers, few of these continued dorsally to innervate the area lateral to the eminentia thalami (Figure 1H, n = 9; Figure 1I, n = 9). Previous experiments have shown that this region contains GABAergic projection neurons that innervate brainstem motor regions, including the optic tectum, mesencephalic, and diencephalic locomotor regions [13–15]. We conclude that this area receives projections from striatum and expresses the same molecular markers as the mammalian GPe/GPi.

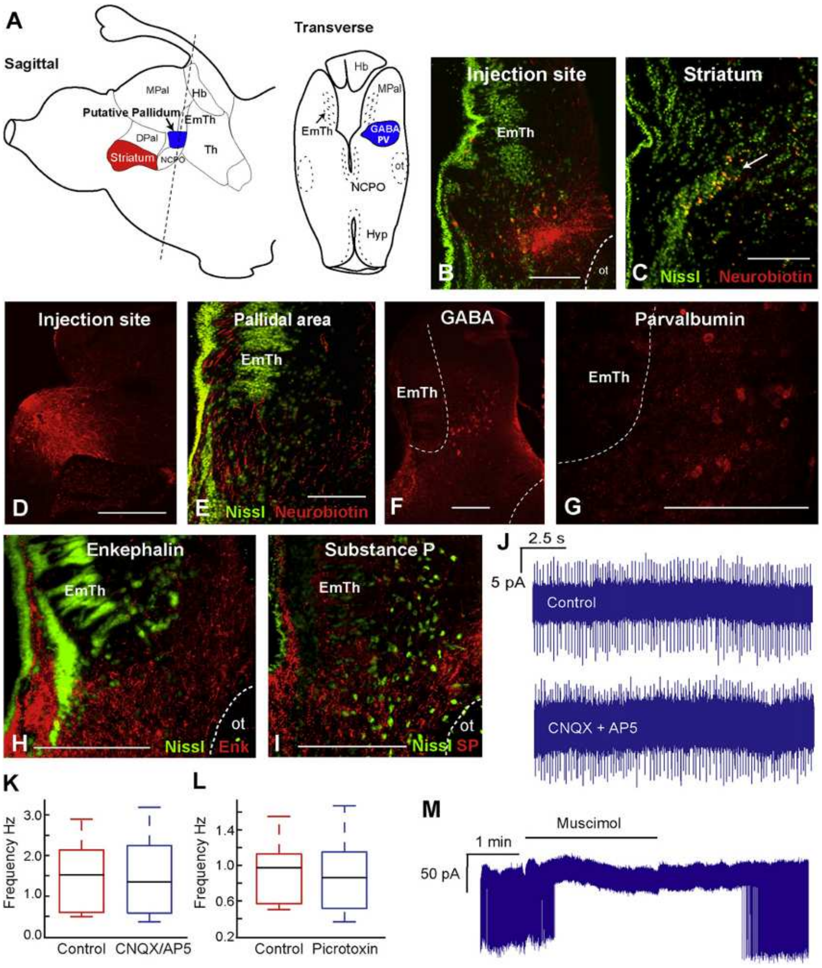

***Figure 1**. Anatomical and Electrophysiological Evidence for a Lamprey Pallidum (A) Schematic drawings of sagittal and transverse sections through the lamprey brain, indicating the location of the striatum and the putative pallidum. (B and C) Neurobiotin injection (red) into the putative pallidal region (B) resulting in retrogradely labeled striatal cells (C). (D and E) Injection into the striatum (D) resulting in labeled efferent fibers in the putative pallidal region (E). (F) GABA immunoreactive cells at the level of the eminentia thalami. (G) Parvalbumin immunoreactive cells at the level of the eminentia thalami. (H) Enkephalin immunoreactive fibers in the putative pallidal region. (I) Substance P immunoreactive fibers in the putative pallidal region. (J) Loose-patch recordings of a spontaneous repetitively firing retrogradely labeled neuron (from the tectum) before (mean frequency 5.10 6 1.01 Hz) and after (mean frequency 4.31 6 1.41 Hz) the application of the glutamatergic antagonists CNQX (40 mM) and AP5 (40 mM). (K and L) Box plots showing the normalized range and average instantaneous frequency of pallidal neurons before and after application of glutamatergic receptor antagonists (control, mean = 1.5 6 0.86 Hz; CNQX and AP5, mean = 1.37 6 1.01 Hz) (K) or GABAA receptor antagonist picrotoxin 50 mM (control, mean = 0.92 6 0.41 Hz; picrotoxin, mean = 0.86 6 0.51 Hz) (L). (M) Loose-patch recording of a pallidal neuron before, during, and after the application of muscimol. Scale bars (B), (C), (E), (F), (G), (H), and (I) represent 200 mm; (D) represents 500 mm. The following abbreviations are used: DPal, dorsal pallium; EmTh, eminentia thalami; Hb, habenula; Hyp, hypothalamus; MPal, medial pallium; NCPO, nucleus of the postoptic commissurae; ot,optic tract*

In mammalian species, these GABAergic pallidal projection neurons have been shown to tonically inhibit motor areas as a result of their high level of spontaneous activity. If the lamprey pallidal neurons have a similar physiological role, they should also be tonically active at rest. Spontaneous firing was observed in most (n = 18/29) of the neurons recorded with the loose-patch configuration, for up to 20 min. In loose-patch recordings, these neurons fired with instantaneous firing frequencies ranging between 1 and 25 Hz, with a mean around 4 Hz. In whole-cell recordings, firing frequencies were lower, ranging from 1 to 12 Hz (n = 8/13). These firing frequencies are lower than those of mammalian pallidal neurons in vitro and may reflect the lower temperatures at which our recordings were made (6°C versus 37°C). To test whether these tonically active neurons were projection neurons, we recorded from pallidal neurons that were retrogradely labeled from the optic tectum (n = 19). Approximately 70% of these retrogradely labeled cells were spontaneously active (13 out of 19), suggesting that the pallidum may tonically inhibit areas of the brain that it projects to. Retrogradely labeled cells in the areas surrounding the putative pallidum, either caudally in the thalamus or rostrally in the medial pallium, did not display any spontaneous activity (data not shown).

If the lamprey pallidal neurons tonically inhibit motor regions at rest, as they do in other species, then the activity of these neurons should not rely on synaptic input. Indeed, the spontaneous activity was not significantly altered by blocking the glutamatergic or GABAergic synaptic input with CNQX 40 mM and AP-5 50–200 mM (n = 10; Figures 1J and 1K) or picrotoxin (50 mM; n = 5). The tonic activity thus appears to be an inherent property and suggests that these pallidal neurons could inhibit motor regions in the absence of synaptic input. Application of muscimol (5 mM, n = 4), a GABAA agonist, blocked all spontaneous activity in 3 out of 4 neurons and was strongly reduced in the remaining case (Figure 1M; mean frequency 3.82 6 2.65 Hz before; 0.13 6 0.22 Hz in muscimol; and 2.92 6 2.30 Hz after washout). This suggests that GABAergic input from the striatum could potentially silence these neurons and thereby disinhibit the motor areas.

Everything taken together, this area, ventrolateral to eminentia thalami, appears to be homologous to the avian and mammalian GPi and GPe based on the input from striatum, the presence of substance P and enkephalin immunoreactive fibers, expression of GABA and parvalbumin, and the electrophysiological properties of its projection neurons (see also Discussion). We will therefore refer to this area as the lamprey pallidum (GPi and GPe) and the neurons located within this area as pallidal neurons for the remainder of this manuscript.

Connectivity of the Putative Pallidum

Tonically active GABAergic neurons of the pallidum, in other species, inhibit motor programs by projecting to critical motor areas in the brainstem or via the thalamus to the cortex. In order to explore which areas might influence and be influenced by the tonic inhibitory output of the lamprey pallidum, we examined its connectivity. A bidirectional tracer, neurobiotin, was injected in the pallidum (Figure 2A [red]; Figure 2B, n = 6). This resulted in retrogradely labeled cells in the striatum (Figure 2C; depicted as red dots in Figure 2A) but also in cells in a subthalamic region (Figure 2D). A few cells were also observed in the dorsomedial lateral pallium and in the dorsal thalamus (Figure 2A). These latter populations were labeled after injections lateral to the eminentia thalami (blue in Figure 2A), but no labeling was observed in either the striatum or the subthalamic region, giving further support that the projections from the striatum and the subthalamic region may terminate ventrolateral to the eminentia thalami but that the other populations may have been labeled from fibers of passage. Anterogradely labeled fibers from the injections in the pallidum (red in Figure 2A) were observed in an area that has physiologically been described as the diencephalic locomotor region (DLR) [23] and in the subthalamic region in the same area as the retrogradely labeled neurons were observed (Figure 2D). More caudally, fibers were present in the pretectum and the deeper and intermediate layers of the optic tectum (Figure 2E). In the mesencephalon, fibers were observed in the torus semicircularis, isthmic region, and ventrolateral mesencephalon (Figures 2A and 2F), an area that has recently been described as a homolog of the substantia nigra pars reticulata (SfN abstract, M. Jones et al., 2009; FENS abstracts, J. Ericsson et al., 2010; B. Robertson et al., 2010). Fibers also innervated the ventral mesencephalon in both the mesencephalic locomotor region (MLR) [13] and an area lateral to the MLR that contains cholinergic neurons that project to the optic tectum [15, 24, 25], which may potentially represent the pedunculopontine nucleus (Figure 2F). The major projections of these tonically active GABAergic pallidal neurons are therefore both to critical brainstem motor areas and other potential intrabasal ganglia nuclei that may, through reciprocal connections, influence the level of pallidal activity (Figure 2G). Together with physiological data and the previous data showing that the projection neurons in this area are GABAergic [13–15], this suggests that the pallidal nucleus may be responsible for the tonic inhibition of motor regions that is observed in lamprey [13, 14] (SfN abstract, B. Robertson et al., 2007).

Separate, Intermingled Pallidal Populations Project to Each of the Motor Areas and the Subthalamic Region

In order to test whether separate pallidal populations could select actions by independently disinhibiting each of the motor regions, we explored whether the pallidal populations projecting to each of these areas arose from distinct subpopulations. Injections in the optic tectum, MLR, DLR, and the subthalamic region resulted in retrogradely labeled neurons in the pallidum (Figures 3A–3L; n = 13, 6, 6, 7). Dual injections in two of these motor regions at a time never resulted in doublelabeled pallidal neurons, suggesting that the pallidal populations that project to one motor region were separate from those projecting to another motor region (Figures 3A–3I; n = 3 each).
The same is true for the population of pallidal neurons that project to the subthalamic region; these were distinct from those that project to the optic tectum (Figures 3J–3L, n = 3). This suggests that multiple intermingled parallel pathways through the pallidumcould independently regulate each motor area (Figure 3M).

Anatomical and Electrophysiological Evidence for a Lamprey Subthalamic Nucleus

The reciprocal connections between the pallidum and neurons in the subthalamus suggest that a component of the indirect pathway, the subthalamic nucleus, may be present in lamprey.
Neurons in the lamprey subthalamus, retrogradely labeled following an injection in the pallidum (Figure 4A; n = 3), were all immunoreactive for glutamate (Figures 4B and 4C), suggesting that this nucleus may have an excitatory influence on pallidal projection neurons as it does in the mammalian species. In contrast, retrogradely labeledneurons locatedcloser to the thalamus did not express glutamate. Neurons in the subthalamic region were located in prosomere 4 of the lamprey prosomeric map (Figure 4D; see [26]), the same developmental location as the avian and mammalian subthalamic nuclei [18]. Both in vitro and in vivo mammalian subthalamic neurons exhibit spontaneous activity and postinhibitory rebound (PIR) spikes and a voltage sag in response to membrane hyperpolarization [27]. To address whether these characteristics were also observed in lamprey subthalamic neurons, we performed loose-patch (n = 2) and whole-cell (n = 6) patch clamp recordings, with one neuron recorded in both configurations.
All recorded neurons were tonically active; in loose patch, the recorded neurons showed instantaneous frequencies ranging from 2.8 to 26.3 Hz (Figure 4E), recorded over several minutes. Maximum firing frequency, induced by depolarizing current pulses, was 20.3 6 2.1 Hz when averaged over 1 s (Figure 4G) and with a maximum instantaneous frequency of 45.5 Hz, measured over the first interval. Upon strong depolarization, neurons either ceased firing after hundreds of milliseconds or fired with distinct pauses (see bottom trace in Figure 4G). In addition, all cells exhibited PIR action potentials following hyperpolarizing pulses and displayed a pronounced voltage sag presumably mediated by an Ih current (a hyperpolarization-activated cation current) (Figure 4H). Together, these results suggest that even anamniote vertebrates have a nucleus

molecularly, physiologically, and anatomically homologous to the mammalian subthalamic nucleus (Figure 4I).

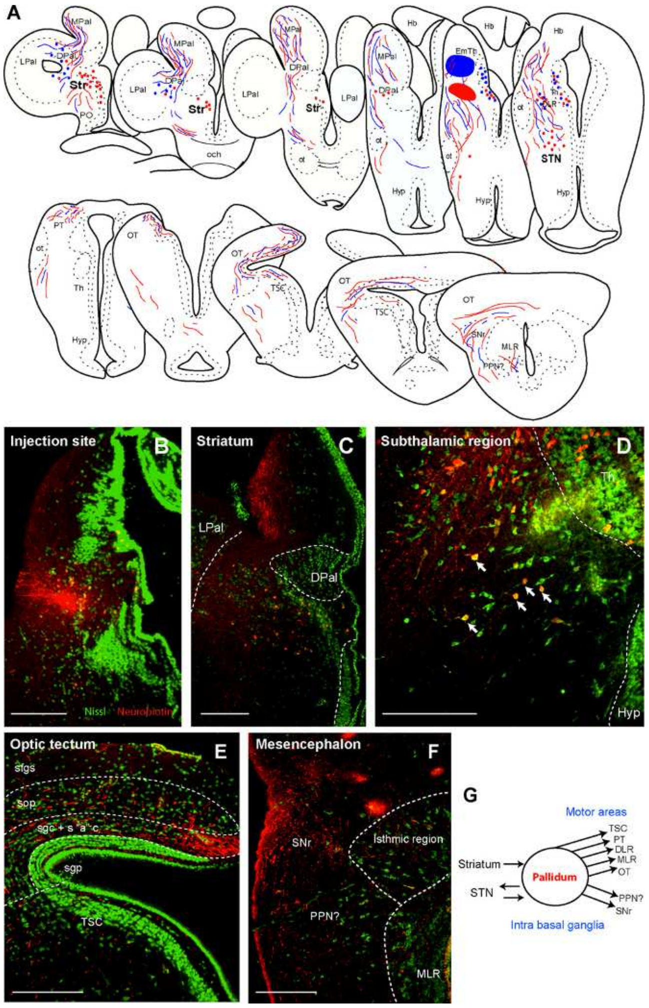

__Figure 2__. Connectivity of the Pallidum (A–F) Schematic transverse sections through the lamprey brain showing the location of retrogradely labeled cells (red and blue dots) and anterogradely labeled fibers (red and blue lines) from two injection sites (neurobiotin) adjacent to the eminentia thalami (A). Note that the red injection gives rise to labeled striatal and subthalamic cells, whereas the blue injection does not. Injection site in the pallidum (B) resulted in retrogradely labeled neurons in the striatum and the lateral pallium (C), retrograde and anterograde labeling in the subthalamic region and the thalamus (D), anterograde labeling in the deep and intermediate layers of the optic tectum (E), and anterograde labeling in the caudal mesencephalon (F). All sections are counterstained with green fluorescent Nissl stain. Scale bars (B), (C), (E), and (F) represent 200 mm; (D) represents 100 mm. The following abbreviations are used: DLR, diencephalic locomotor region; DP, dorsal pallidum; DPal, dorsal pallium; EmTh, eminentia thalami; Hb, habenula; Hyp, hypothalamus; LPal, lateral pallium; MLR, mesencephalic locomotor region; MPal, medial pallium; och, optic chiasm; OT, optic tectum; ot, optic tract; PPN, putative pedunculopontine nucleus; PT, pretectum; sfgs, stratum fibrosum et griseum superficiale; sgc + s''a''c, stratum griseum centrale + stratum ''album'' centrale; sgp, stratum griseum periventriculare; SNr, substantia nigra pars reticulata; sop, stratum opticum; STN, subthalamic nucleus; Str, striatum; Th, thalamus; TSC, torus semicircularis.

Substance P and Enkephalin Immunoreactive Striatal Neurons Project to the Pallidum

If an indirect pathway exists in lamprey, as the presence of a subthalamic nucleus suggests, then there should be two separate populations of medium spiny neurons (MSNs) that express either enkephalin or substance P. Immunohistochemistry revealed that striatal neurons retrogradely labeled from the putative pallidum (Figures 5A and 5E) were immunoreactive for substance P or enkephalin (Figures 5B–5D, n = 3; Figures 5F–5H, n = 3). The substance P immunoreactive neurons were located in the rostral striatum and arranged in a tight cluster ventral to the striatal band, which is in accordance with previously published data [28]. In contrast, the enkephalin immunoreactive neurons were observed more caudally and were mainly confined to the striatal band (see Figure S1 available online). This topographic segregation in populations has not been observed in other species [5] and may indicate that each population develops in different domains before migrating, in jawed vertebrates, to form an intermingled population.

Double staining for substance P and enkephalin showed that there was no overlap in the immunofluorescence in the pallidum (Figures 6A and 6D). This suggests that the substance P- and enkephalin-expressing striatal neurons form distinct populations and may form the input layers of the direct and indirect pathways.

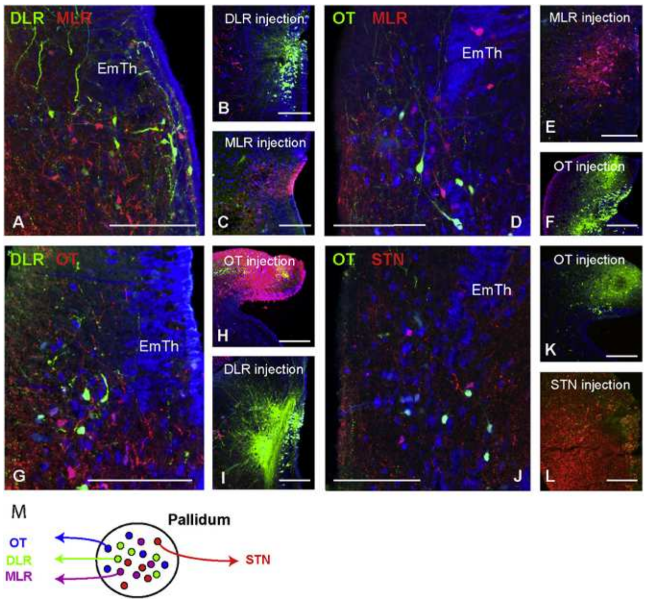

***Figure 3**. Separate Pallidal Subpopulations Projecting to Brainstem Motor Regions and the Subthalamic Nucleus Are Intermingled (A–L) Retrograde (Alexa Fluor 488-conjugated 10 kDa dextran) labeled neurons (green) from injections into the optic tectum and the diencephalic locomotor region and retrograde neurobiotin- labeled neurons (red) from injections into the mesencephalic locomotor region, optic tectum, and subthalamic region (A), (D), (G), and (J). Corresponding injection sites (B), (C), (E), (F), (H), (I), (K), and (L). Scale bars represent 200 mm. (M) Schematic drawing showing that separate populations of pallidal neurons that project to both motor areas and a subthalamic area are intermingled. For abbreviations, see Figure 2 legend.*

Substance P and Enkephalin Fibers Differentially Contact Separate Pallidal Projection Neurons

To test whether the substance P- and enkephalin-expressing striatal neurons contact separate pallidal subpopulations associated with the direct and indirect pathways, we retrogradely labeled pallidal neurons from either the putative subthalamic nucleus (Figure 6B; n = 3) or the optic tectum (Figure 6E; n = 4). The subthalamic projecting neurons were mainly contacted by enkephalin immunoreactive fibers, and 87% 6 11% of all putative contacts were immunoreactive for enkephalin (Figures 6A and 6C; n = 9). This arrangement closely mimics the mammalian organization because there is a predominant indirect (enkephalin-GPe-STN) pathway [22].
In contrast, neurons projecting to the optic tectum were predominantly contacted by substance P immunoreactive fibers (80% 6 13%). The processes and somata of these neurons were peppered with numerous substance P putative synaptic contacts (Figures 6D and 6F; n = 12) as with the direct (substance P-GPi-motor areas) pathway. Despite the different pallidal subpopulations being intermingled in one pallidal nucleus, it appears that the predominant functional arrangement of direct and indirect circuits is present even in the phylogenetically oldest group of vertebrates (Figure 7). As in mammals, this functional arrangement is complicated by the fact that ‘‘direct’’ or ‘‘indirect’’ projecting MSNs contact both GPe-like and GPi-like neurons [29, 30]; consequently, crosstalk between these pathways, at the pallidal level, is also a conserved feature of the basal ganglia.

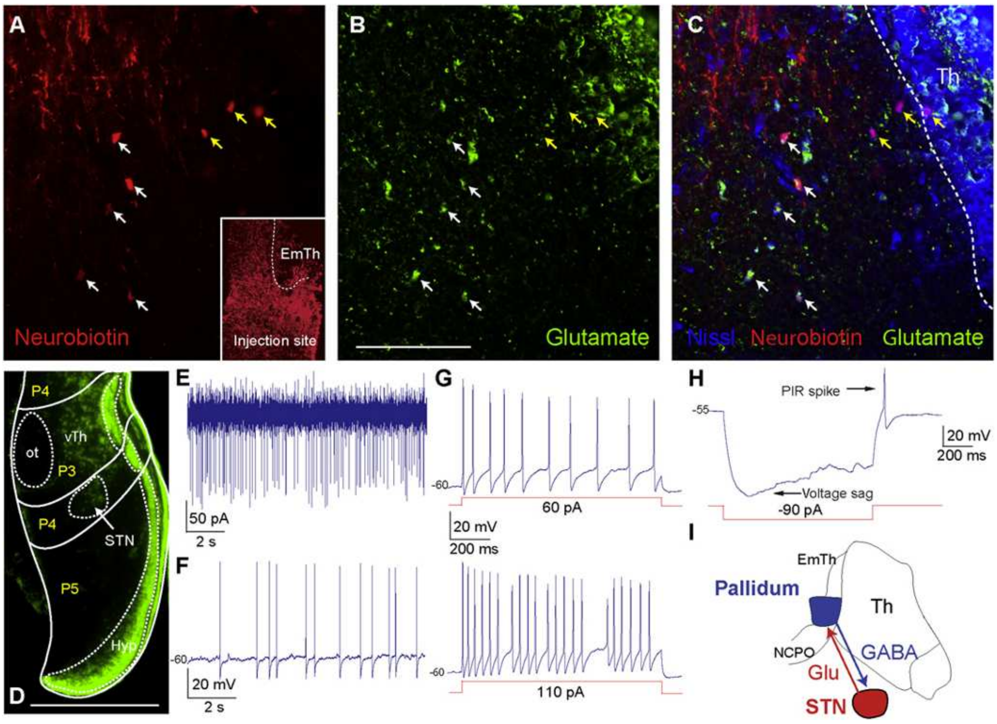

Figure 4. *Anatomical and Electrophysiological Evidence for a Lamprey Subthalamic Nucleus (A) Retrogradely labeled neurons in the subthalamic region following an injection in the pallidum. (B) Glutamate immunoreactive neurons in the subthalamus and thalamus. (C) Merged image including blue fluorescent Nissl stain. (D) Transverse section through the diencephalon showing the prosomeric locations of different populations as previously described [26]. The subthalamus is located in prosomere 4. (E) Loose-patch recording of a spontaneous repetitively firing neuron (mean firing frequency 8 Hz). (F) Whole-cell recording of a spontaneously active neuron firing action potentials with a lower frequency around 1 Hz, from a baseline potential of 260 mV without any current injection. (G) Firing behavior of the*

neuron in (F) at different current injections shown in red. (H) Hyperpolarization-activated voltage sag and postinhibitory rebound (PIR) action potential as a response to a hyperpolarizing current step. (I) Schematic sagittal section through the lamprey diencephalon, showing the location of the pallidum and the subthalamic nucleus. Scale bars (A), (B), and (C) represent 200 mm; (D) represents 500 mm. The following abbreviations are used: NCPO, nucleus of the postoptic commissure; Glu, glutamate. See Figure 2 legend

3.2 Discussion

Our results show that in contrast to a sequential theory for the evolution of the basal ganglia, all of the major components of the basal ganglia including the striatum, an intermingled GPi and GPe, and a STN exist in the phylogenetically oldest group of vertebrates. Our results suggest that these nuclei, interconnected through direct and indirect pathways, represent evolution’s blueprint for the vertebrate basal ganglia and form a core network that potentially, as was hypothesized, evolved as the vertebrate solution to how to select actions [4]. We propose that during evolution, this processing unit has been reused to perform the same computations for different kinds of motor, emotional, and cognitive information, serving as a core selection architecture in the mammalian parallel loops. By changing the input and output of this ancestral architecture and processing different modalities, each loop (functional module) will develop a different functional consequence. Selective activation of the limbic module, for example, has recently been shown to select the preference for reward, whereas the motor module is known to select actions [31, 32]. In evolution, the reuse of an existing feature for a new function has been termed ‘‘exaptation’’ [33], and our results suggest that this process together with the classical adaptation has played a major role in shaping the evolution of the vertebrate brain. The current study provides the first direct evidence that the pallidum exists in a jawless vertebrate. Our data suggest that it is homologous to an intermingled GPi and GPe, based on connectivity, molecular expression, and electrophysiological properties, as already concluded in the Results. In contrast to our current results, previous developmental studies claimed that lamprey was unlikely to have a pallidum as a result of the lack of Nkx2.1 expression in the ventral telencephalon [8, 9]. One explanation for why Nkx2.1 was not observed in the ventral telencephalon is that the expression of Nkx2.1 occurs later in this area than at embryonic day 26, which was tested. This is likely, because the GABAergic neurons in the forebrain, which during development also rely on the expression of Nkx2.1, do not appear in lamprey until later in development in the larval stages [12]. This transcription factor is also crucial for the development of striatal and cortical interneurons [34], and these have been observed in lamprey, including the cholinergic interneurons, neurons resembling the fast spiking interneurons, and GABAergic neurons in the pallium [25] (SfN abstract, J. Ericsson et al., 2010). Together with the evidence that we provide here, it would appear either that the pallidum and striatal interneurons that rely on the expression of Nkx2.1 are present in lamprey and have developed under different transcriptional control or, more likely, that the pallidum differentiates later in development than in other vertebrates.

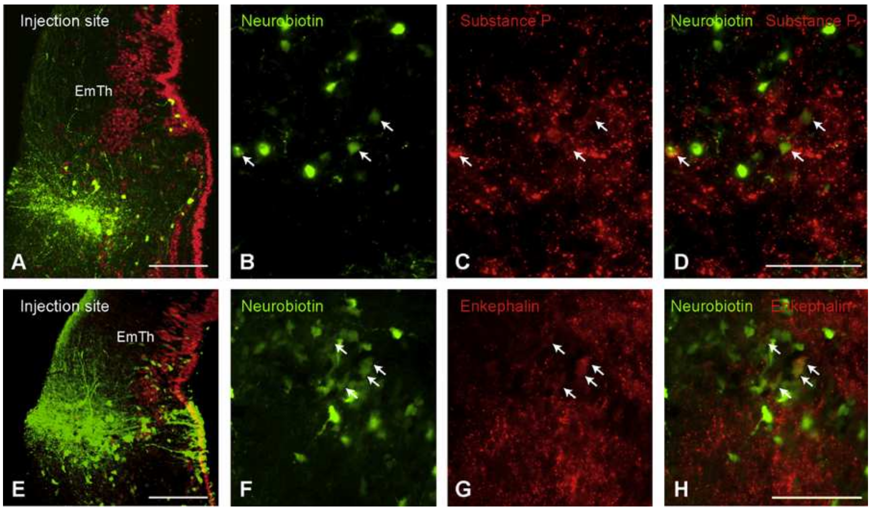

***Figure 5**. Substance P and Enkephalin Are Expressed in Striatal Projection Neurons*
(A) Injection site in the putative pallidum, counterstained with red fluorescent Nissl stain.
(B) Neurobiotin retrogradely labeled neurons in the striatum following an injection in the putative pallidum.
(C) Substance P immunoreactive cells in the striatum.
(D) Merged image.
(E) Injection site in the putative pallidum, counterstained with red fluorescent Nissl stain.
(F) Neurobiotin retrogradely labeled neurons in the striatum following an injection in the putative pallidum.
(G) Enkephalin immunoreactive cells in the striatum.
(H) Merged image. Scale bars (A) and (E) represent 200 mm; (B), (C), (D), (F), (G), and (H) represent 100 mm. The following abbreviation is used: EmTh, eminentia thalami.

The pallidal arrangement thatweshowhere with substance and enkephalin neurons projecting to an intermingled GPi and GPe is likely to be present in other nonmammalian vertebrates. This organization has previously been demonstrated in birds [18], whereas in reptiles, lungfish, sharks, and amphibians, substancePand enkephalin fibers innervate the entire pallidum instead of separate nuclei, but in these species, a subdivision of the GPi and GPe pallidal populations remains to be demonstrated [35–38]. The arrangement of the mammalian pallidum differs from other vertebrates because the substance P and enkephalin neurons predominantly project to separate nuclei, the GPi and GPe, respectively [39]. Despite this gross morphological change, our data suggest that the functional arrangement of direct (striatum [substance P]-GPi-motor areas) and indirect (striatum [enkephalin]-GPe-STN) pathways appear to be conserved in jawless vertebrates. Our results suggest that the indirect pathway is an integral part of all vertebrate basal ganglia and evolved before jawed and jawless vertebrates diverged over 560 mya [21]. An additional feature of the basal ganglia in other vertebrates is a secondary parallel direct pathway through the basal ganglia, culminating in the substantia nigra pars reticulata (for review see [5]). This dual-output nucleus is also likely to have been part of the ancestral basal ganglia because data suggest that a homolog of this nucleus is also present in lamprey (SfN abstract, M. Jones et al., 2009; FENS abstracts, J. Ericsson et al., 2010; B. Robertson et al., 2010). The evidence for a lamprey homolog of this nucleus will be presented in a forthcoming study (M.S.-J., E.S., B.R., and S.G., unpublished data). A limited number of GABAergic projection neurons are also present in the ventrolateral pallium that target MLR but not tectum [13, 15]. It was inferred by Pombal et al. [7] that these cells might receive projections from striatum, and consequently be in a pallidal nucleus, but this has yet to be confirmed. In contrast to this view, cells in the same area provide input to striatum, as does the pallium in other vertebrates [7]. Functionally, as mentioned in the Introduction, the basal ganglia are known from computational, physiological, and behavioral data to play an important role in action selection [4, 40–43]. In mammals, the direct pathway has been shown to induce actions by reducing the tonic inhibitory output of the pallidal output nuclei (GPi/SNr) [3, 31]. In contrast, the indirect circuitry, when selectively activated, suppresses actions by increasing the inhibition of thalamic and brainstem motor areas [31]. As a result of their tonic activity and inhibitory projections to brainstem and diencephalic locomotor regions, the GPi-like neurons are good candidates for providing the tonic inhibition of motor areas that is observed in lamprey [13, 14]. In addition, removal of this inhibition has been shown to either induce actions or significantly lower the threshold for initiation [13, 14]. This suggests that the anatomical architecture may also function in a similar way to mammals because altering the level of inhibition through the direct or indirect striatal projections should either increase or decrease the inhibition on motor areas and select or suppress actions.

Although the circuitry may be conserved, the behavioral impact of the basal ganglia depends on its input and output connections. In lamprey, we show that the majority of basal ganglia output is directed toward brainstem motor areas, including the optic tectum, pretectum, MLR, and DLR. This suggests that the basic function of the basal ganglia is to influence the selection of actions from brainstem motor areas. In the mammalian species, the simplified direct and indirect circuitry has been suggested to control limbic and associative functions in addition to motor selection [32, 44, 45]. These different modalities are thought to be processed in homologous parallel loops (functional modules), each of which contain the same direct and indirect circuitry [39, 46].

Because we now show that this core circuitry is likely to have been present in the common ancestor of all vertebrates it suggests that during evolution, each of the modules has arisen from a replication of the ancestral architecture and that the input and output of this core computational unit has changed rather than the internal organization of the circuitry. As a result of this, we propose that during evolution, these circuits have been coopted, through a process of exaptation, to serve multiple functions through homologous parallel repeats of this architecture. Even though our data suggest that the basal ganglia evolved mainly through exaptation, we do not rule out the possibility that additions to this core architecture may have arisen through adaptation.

Possible additions may have occurred at the microcircuit or cellular level, especially in the striatum where the types and the electrophysiological properties of neurons have been shown to be diverse in mammals [47, 48] and to differ from nonmammalian species [49]. These striking results show that the detailed basal ganglia circuitry found in mammals had already emerged in the phylogenetically oldest group of vertebrates. It has thus been conserved, most likely as a common mechanism for action selection, in all vertebrates, from lampreys to primates. The presence of the complete basal ganglia circuitry in all vertebrates suggests that this architecture may have evolved before vertebrates and invertebrates diverged. Although the composition of any such invertebrate system remains to be elucidated, recent work has suggested that the central complex may play a similar function to the basal ganglia in Drosophila [50]. This raises the intriguing possibility that the basal ganglia may be present as a common mechanism for selection in all animals with bilateral symmetry, and not just in vertebrates.

Our data challenge the classical view that brains have evolved from simple to complex through sequential adaptation. Our results indicate instead that the complexity of mammalian brains at least in part has evolved through multiplication and functional reuse of existing ancestral circuits, a process that is also thought to have occurred in other areas of the brain including the hindbrain [51, 52]. This process of functional reuse of an existing feature is known in evolutionary biology as exaptation, and our results suggest that this has been an important process in the evolution of the brain.

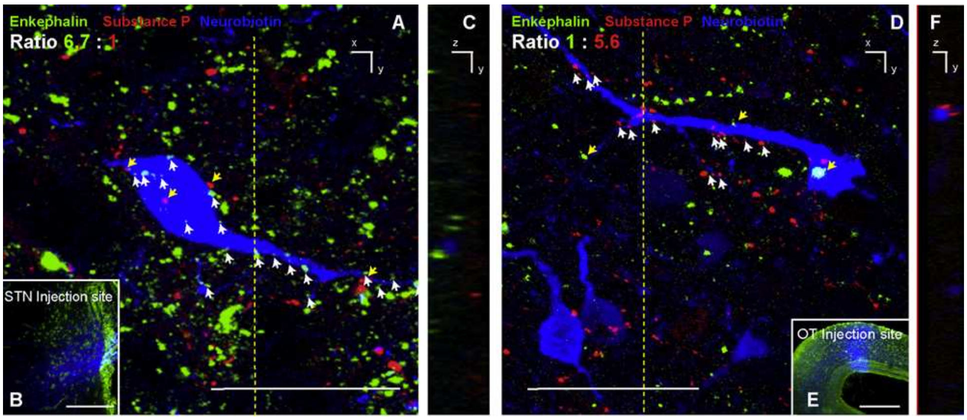

***Figure 6**. Substance P and Enkephalin Fibers Differentially Contact Separate Pallidal Projection Neurons (A–C) Confocal projection of a pallidal neuron retrogradely labeled (blue) (A) from an injection (neurobiotin) in the subthalamic region (B) with substance P (red, yellow arrows) and enkephalin (green, white arrows) immunoreactive fibers. The yellow dotted line indicates the plane in which the z-y axis of the confocal projection is shown (C). (D–F) Confocal projection of a pallidal neuron retrogradely labeled (blue) (D) from an injection in the optic tectum (E) with substance P (red, white arrows) and enkephalin (green, yellow arrows) immunoreactive fibers. The yellow dotted line indicates the plane in which the z-y axis of the confocal projection is shown (F). Scale bars (A) and (D) represent 50 mm; (B) and (E) represent 200 mm*

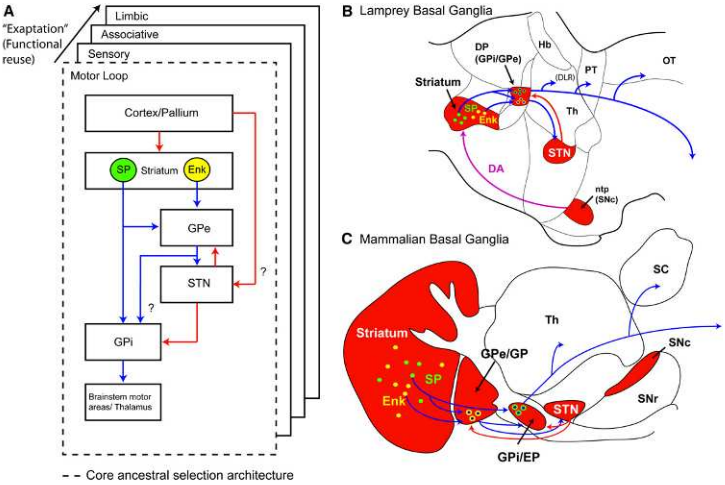

***Figure 7.** Comparison of the Mammalian and Lamprey Basal Ganglia (A) Schematic showing the evolutionarily conserved functional module in the form of a motor loop and subsequent functional repeats of this architecture that have likely evolved through exaptation. Blue and red arrows indicate GABAergic or glutamatergic projections respectively (A–C). The question marks indicate features that are clearly present in the mammalian architecture but have not been explored in lamprey, including the hyperdirect pathway and possible GPe and GPi projections. (B) Schematic sagittal section through the lamprey brain showing the location of the known basal ganglia nuclei and their connectivity; for data regarding the ntp (SNc), see [7]. (C) Schematic section of a mouse brain offering a comparison to lamprey for the topographic location and known mammalian basal ganglia connectivity. The following abbreviations*

are used: DA, dopamine; DP, dorsal pallidum; Enk, enkephalin; EP, entopeduncular nucleus; GP, globus pallidus; GPe, external segment of the globus pallidus; GPi, internal segment of the globus pallidus; Hb, habenula; ntp, nucleus tuberculi posterior; SNc, substantia nigra pars compacta; SNr, substantia nigra pars reticulata; SP, substance P; STN, subthalmic nucleus; Th, thalamus

Experimental Procedures

Experiments were performed on a total of 53 adult river lampreys (*Lampetra fluviatilis*). For ethical committee approval and guidelines adhered to, see Supplemental Experimental Procedures.

Anatomy

The dissection, injections, fixation, and sectioning of the lamprey brains for anatomical experiments were performed as previously described ([53]; see also Supplemental Experimental Procedures). Injections of Neurobiotin (Vector; 20% in distilled water) or Alexa Fluor 488-dextran 10 kDa (12% in distilled water; Molecular Probes Europe BV) was pressure injected unilaterally into the medial pallium (n = 9), striatum (n = 6), subthalamic nucleus (n = 7), optic tectum (n = 12), MLR (n = 6), and DLR (n = 6).

Immunohistochemistry

Primary antibodies immunoreactive for substance P, enkephalin, parvalbumin, GABA, and glutamate were used. Sections were subsequently incubated with different secondary antibodies (1:500; Jackson Immunoresearch) and Neurotrace (1:500; Molecular Probes); see Supplemental Experimental Procedures for details of primary and secondary antibodies used.

Electrophysiology

Slices for electrophysiological recordings were made as previously described ([54]; see also Supplemental Experimental Procedures for details). Anatomical landmarks (eminentia thalami and optic tract) or retrograde labeling was used to identify neurons in the pallidum for whole-cell (n = 13) and loose-patch recordings. Retrograde labeling from the pallidum was used to identify neurons in the subthalamus (n = 7).

Supplemental Information

Supplemental Information includes one figure and Supplemental Experimental Procedures and can be found with this article online at doi:10. 1016/j.cub.2011.05.001.

Acknowledgments

This paper is dedicated to the loving memory of Ebba Samuelsson. Grant Sponsors include the EU Cortex training program, FP6 MEST-CT-2005- 019729 (to S.G. for M.S.-J.); EU, FP5 ‘‘Neurobotics’’ 001917 (to S.G.); Swedish Research Council, VR-M 3026, VR-NT 621-2007-6049 (to S.G.); Karolinska Institute’s research funds (to B.R.); FP7 Select-and-Act (to S.G.); and Karolinska Institute’s doctoral funds (to J.E. and E.S.).

3.2 References

1. Graybiel, A.M. (1998). The basal ganglia and chunking of action repertoires. Neurobiol. Learn. Mem. 70, 119–136.
2. Grillner, S., Hellgren, J., Me´ nard, A., Saitoh, K., and Wikstro¨ m, M.A. (2005). Mechanisms for selection of basic motor programs—roles for the striatum and pallidum. Trends Neurosci. 28, 364–370.
3. Hikosaka, O., Takikawa, Y., and Kawagoe, R. (2000). Role of the basal ganglia in the control of purposive saccadic eye movements. Physiol. Rev. 80, 953–978.
4. Redgrave, P., Prescott, T.J., and Gurney, K. (1999). The basal ganglia: A vertebrate solution to the selection problem? Neuroscience 89, 1009– 1023.
5. Reiner, A., Medina, L., and Veenman, C.L. (1998). Structural and functional evolution of the basal ganglia in vertebrates. Brain Res. Brain Res. Rev. 28, 235–285.
6. Pombal, M.A., El Manira, A., and Grillner, S. (1997). Organization of the lamprey striatum - transmitters and projections. Brain Res. 766, 249–254.
7. Pombal, M.A., El Manira, A., and Grillner, S. (1997). Afferents of the lamprey striatum with special reference to the dopaminergic system: A combined tracing and immunohistochemical study. J. Comp. Neurol. 386, 71–91.
8. Murakami, Y., Ogasawara, M., Sugahara, F., Hirano, S., Satoh, N., and Kuratani, S. (2001). Identification and expression of the lamprey Pax6 gene: Evolutionary origin of the segmented brain of vertebrates. Development 128, 3521–3531.
9. Murakami, Y., Uchida, K., Rijli, F.M., and Kuratani, S. (2005). Evolution of the brain developmental plan: Insights from agnathans. Dev. Biol. 280, 249–259.
10. Osorio, J., Mazan, S., and Re´ taux, S. (2005). Organisation of the lamprey (Lampetra fluviatilis) embryonic brain: Insights from LIM-homeodomain, Pax and hedgehog genes. Dev. Biol. 288, 100–112.
11. Robertson, B., Auclair, F., Me´ nard, A., Grillner, S., and Dubuc, R. (2007). GABA distribution in lamprey is phylogenetically conserved. J. Comp. Neurol. 503, 47–63.
12. Mele´ ndez-Ferro, M., Pe´ rez-Costas, E., Villar-Cheda, B., Abalo, X.M., Rodrı´guez-Mun˜ oz, R., Rodicio, M.C., and Anado´ n, R. (2002). Ontogeny of gamma-aminobutyric acid-immunoreactive neuronal populations in the forebrain and midbrain of the sea lamprey. J. Comp. Neurol. 446, 360–376.
13. Me´ nard, A., Auclair, F., Bourcier-Lucas, C., Grillner, S., and Dubuc, R. (2007). Descending GABAergic projections to the mesencephalic locomotor region in the lamprey Petromyzon marinus. J. Comp. Neurol. 501, 260–273.
14. Me´ nard, A., and Grillner, S. (2008). Diencephalic locomotor region in the lamprey—afferents and efferent control. J. Neurophysiol. 100, 1343– 1353.
15. Robertson, B., Saitoh, K., Me´ nard, A., and Grillner, S. (2006). Afferents of the lamprey optic tectum with special reference to the GABA input: Combined tracing and immunohistochemical study. J. Comp. Neurol. 499, 106–119.
16. Afsharpour, S. (1985). Light microscopic analysis of Golgi-impregnated rat subthalamic neurons. J. Comp. Neurol. 236, 1–13.
17. Bergman, H., Wichmann, T., and DeLong, M.R. (1990). Reversal of experimental parkinsonism by lesions of the subthalamic nucleus. Science 249, 1436–1438. 18. Jiao, Y., Medina, L., Veenman, C.L., Toledo, C., Puelles, L., and Reiner,
A. (2000). Identification of the anterior nucleus of the ansa lenticularis in birds as the homolog of the mammalian subthalamic nucleus. J. Neurosci. 20, 6998–7010.
19. Nakanishi, H., Kita, H., and Kitai, S.T. (1987). Electrical membrane properties of rat subthalamic neurons in an in vitro slice preparation. Brain Res. 437, 35–44.
20. Nakanishi, H., Kita, H., and Kitai, S.T. (1990). Intracellular study of rat entopeduncular nucleus neurons in an in vitro slice preparation: Electrical membrane properties. Brain Res. 527, 81–88.

21. Kumar, S., and Hedges, S.B. (1998). A molecular timescale for vertebrate evolution. Nature 392, 917–920.

22. Albin, R.L., Young, A.B., and Penney, J.B. (1989). The functional anatomy of basal ganglia disorders. Trends Neurosci. 12, 366–375.

23. ElManira, A., Pombal, M.A., and Grillner, S. (1997). Diencephalic projection to reticulospinal neurons involved in the initiation of locomotion in adult lampreys Lampetra fluviatilis. J. Comp. Neurol. 389, 603–616.

24. de Arriba Mdel, C., and Pombal, M.A. (2007). Afferent connections of the optic tectum in lampreys: An experimental study. Brain Behav. Evol. 69, 37–68.

25. Pombal, M.A., Marı´n, O., and Gonza´ lez, A. (2001). Distribution of choline acetyltransferase-immunoreactive structures in the lamprey brain. J. Comp. Neurol. 431, 105–126.

26. Pombal, M.A., and Puelles, L. (1999). Prosomeric map of the lamprey forebrain based on calretinin immunocytochemistry, Nissl stain, and ancillary markers. J. Comp. Neurol. 414, 391 422.

27. Bevan, M.D., and Wilson, C.J. (1999). Mechanisms underlying spontaneous oscillation and rhythmic firing in rat subthalamic neurons. J. Neurosci. 19, 7617–7628.

28. Auclair, F., Lund, J.P., and Dubuc, R. (2004). Immunohistochemical distribution of tachykinins in the CNS of the lamprey Petromyzon marinus. J. Comp. Neurol. 479, 328–346.

29. Kawaguchi, Y., Wilson, C.J., and Emson, P.C. (1990). Projection subtypes of rat neostriatal matrix cells revealed by intracellular injection of biocytin. J. Neurosci. 10, 3421–3438.

30. Wu, Y., Richard, S., and Parent, A. (2000). The organization of the striatal output system: A single-cell juxtacellular labeling study in the rat. Neurosci. Res. 38, 49–62.

31. Kravitz, A.V., Freeze, B.S., Parker, P.R., Kay, K., Thwin, M.T., Deisseroth, K., and Kreitzer, A.C. (2010). Regulation of parkinsonian motor behaviours by optogenetic control of basal ganglia circuitry. Nature 466, 622–626.

32. Lobo, M.K., Covington, H.E., 3rd, Chaudhury, D., Friedman, A.K., Sun, H., Damez-Werno, D., Dietz, D.M., Zaman, S., Koo, J.W., Kennedy, P.J., et al. (2010). Cell type-specific loss of BDNF signaling mimics optogenetic control of cocaine reward. Science 330, 385–390.

33. Gould, S., and Vrba, E.S. (1982). Exaptation; A missing term in the science of form. Paleobiology 8, 4–15.

34. Marı´n, O., and Rubenstein, J.L. (2001). A long, remarkable journey: Tangential migration in the telencephalon. Nat. Rev. Neurosci. 2, 780–790.

35. Anderson, K.D., and Reiner, A. (1990). Extensive co-occurrence of substance P and dynorphin in striatal projection neurons: An evolutionarily conserved feature of basal ganglia organization. J. Comp. Neurol. 295, 339–369.

36. Marı´n, O., Smeets, W.J., and Gonza´ lez, A. (1998). Basal ganglia organization in amphibians: Chemoarchitecture. J. Comp. Neurol. 392, 285–312.

37. Northcutt, R.G.,Reiner, A.,andKarten, H.J. (1988).Immunohistochemical study of the telencephalon of the spiny dogfish, Squalus acanthias. J. Comp. Neurol. 277, 250–267.

38. Reiner, A., and Northcutt, R.G. (1987). An immunohistochemical study of the telencephalon of the African lungfish, Protopterus annectens. J. Comp. Neurol. 256, 463–481.

39. Alexander, G.E., and Crutcher, M.D. (1990). Functional architecture of basal ganglia circuits: Neural substrates of parallel processing. Trends Neurosci. 13, 266–271.

40. Aldridge, J.W., and Berridge, K.C. (1998). Coding of serial order by neostriatal neurons: A ‘‘natural action’’ approach to movement sequence. J. Neurosci. 18, 2777–2787.

41. Cromwell, H.C., and Berridge, K.C. (1996). Implementation of action sequences by a neostriatal site: A lesion mapping study of grooming syntax. J. Neurosci. 16, 3444–3458.

42. Gurney, K., Prescott, T.J., Wickens, J.R., and Redgrave, P. (2004). Computational models of the basal ganglia: From robots to membranes. Trends Neurosci. 27, 453–459. Current Biology Vol 21 No 13 1090
43. Prescott, T.J., Montes Gonza´ lez, F.M., Gurney, K., Humphries, M.D., and Redgrave, P. (2006). A robot model of the basal ganglia: Behavior and intrinsic processing. Neural Netw. 19, 31 61.
44. Graybiel, A.M. (2005). The basal ganglia: Learning new tricks and loving it. Curr. Opin. Neurobiol. 15, 638–644.
45. Smith, K.S., Tindell, A.J., Aldridge, J.W., and Berridge, K.C. (2009). Ventral pallidum roles in reward and motivation. Behav. Brain Res. 196, 155–167.
46. Alexander, G.E., DeLong, M.R., and Strick, P.L. (1986). Parallel organization
f functionally segregated circuits linking basal ganglia and cortex. Annu. Rev. Neurosci. 9, 357–381.
47. Cicchetti, F., Prensa, L., Wu, Y., and Parent, A. (2000). Chemical anatomy of striatal interneurons in normal individuals and in patients with Huntington's disease. Brain Res. Brain Res. Rev. 34, 80–101.
48. Kreitzer, A.C. (2009). Physiology and pharmacology of striatal neurons. Annu. Rev. Neurosci. 32, 127–147.
49. Farries, M.A., Meitzen, J., and Perkel, D.J. (2005). Electrophysiological properties of neurons in the basal ganglia of the domestic chick: Conservation and divergence in the evolution of the avian basal ganglia. J. Neurophysiol. 94, 454–467.
50. Wessnitzer, J., and Webb, B. (2006). Multimodal sensory integration in insects—towards insect brain control architectures. Bioinspir. Biomim. 1, 63–75.
51. Clarke, J.D.W., and Lumsden, A. (1993). Segmental repetition of neuronal phenotype sets in the chick embryo hindbrain. Development 118, 151–162.
52. Metcalfe, W.K., Mendelson, B., and Kimmel, C.B. (1986). Segmental homologies among reticulospinal neurons in the hindbrain of the zebrafish larva. J. Comp. Neurol. 251, 147–159.
53. Jones, M.R., Grillner, S., and Robertson, B. (2009). Selective projection patterns from subtypes of retinal ganglion cells to tectum and pretectum: Distribution and relation to behaviour. J. Comp. Neurol. 20, 257–275.
54. Ericsson, J., Robertson, B., and Wikstro¨ m, M.A. (2007). A lamprey striatal brain slice preparation for patch-clamp recordings. J. Neurosci. Methods 165, 251–256.

4. Introduction: Selective Projection Patterns from Subtypes of Retinal Ganglion Cells to Tectum and Pretectum: Distribution and Relation to Behavior

One major goal of neuroscience is to reach an understanding of the cellular bases of goal-directed behavior. Fundamental aspects of how these control systems are designed have been addressed in the lamprey, in which the brainstem/spinal cord networks underlying locomotion and steering are understood at the cellular and synaptic level, as is the vestibular control of body orientation (for reviews, see Grillner, 2003; Deliagina et al., 2008). Visuomotor coordination is another critical aspect that needs to be understood at this detailed level, but has so far received much less attention. In the lamprey, two forms of visual motor behavior have been studied in some detail: escape swimming resulting from sudden visual stimuli (Ulle´ n et al., 1993, 1997; Deliagina and Fagerstedt, 2000), and the dorsal light response, a protective reaction, which makes the lamprey or other fish rotate the dark dorsal aspect of the body toward the sun (the light source) and thereby become less visible for predators. Both depend on the pretectal nuclei and can be elicited after ablation of the entire optic tectum (Ulle´ n et al., 1993, 1997; Deliagina and Fagerstedt, 2000). Tectum is, however, required for ordinary goal-oriented motor behavior, and it contains a well-organized motor map (Saitoh et al., 2007). Stimulation of the optic tectum can result in a combination of eye movements, orienting movements, and locomotion. The amplitude, direction, and combination of motor actions vary in a site-specific manner across the tectal surface. The lamprey retina is well developed, with five different visual pigments (opsins) and photoreceptors, each sensitive to a different wave-length, being orthologous to that of jawed vertebrates (Collin et al., 2003; Davies et al., 2007). The optic system of the lamprey eye is also well developed, with a multifocal lens, which suggests that the ability to create wellfocused color images had already evolved before the lamprey separated from the vertebrate evolutionary line leading to jawed vertebrates (Gustafsson et al., 2008). Less is known about the different types of ganglion cells that forward information to tectum and other areas of the brain: they were subdivided into two groups referred to as outer and inner ganglion cells by Fritzsch and Collin (1990).

When the lamprey transforms from its larval stage to its adult form the retinotectal organization develops (de Miguel et al., 1990). As in other vertebrates, the retinal ganglion cells project directly to the superficial layers of the optic tectum, with a prominent input from the contralateral and a limited input from the ipsilateral retina, as well as to the pretectum (Kennedy and Rubinson, 1977; Repe´ rant et al., 1980, 1982; Vesselkin et al., 1984). However, the detailed organization of this input onto the tectum has not been investigated, and neither have the subtypes of retinal ganglion cells that contribute to this projection or the projection to the pretectum. An appreciation of the projection pattern from the retina to the tectum and pretectum is critical for an understanding of how the visuomotor coordination is achieved. Since the lamprey diverged from the evolutionary line prior to the evolution of jawed vertebrates, it cannot be assumed that the retinal innervation pattern of tectum follows the same “rules” as in these groups. Our aim is therefore to identify the morphological types of retinal ganglion cell in the lamprey and determine which of these cells are important for visually guided pretectal and tectal behaviors. The approach is threefold: first, to identify the different types of retinal ganglion cells in the lamprey retina; second, to identify which retinal ganglion cells contribute to the tectal and pretectal visuomotor pathways; and finally, to examine directly how each of the morphological types of retinal ganglion cells projecting to these areas are distributed throughout the retina. This latter information is not only lacking from lamprey, but from almost all other vertebrates. A handful of studies have investigated how retinal ganglion cells projecting to the tectum are distributed throughout the retina, but in these cases the cells were differentiated only by soma size, not by location and general morphology (Wa¨ ssle and Illing, 1980; Provis and Watson, 1981; Rapaport and Wilson, 1983; Perry and Cowey, 1984; Lugo- Garcia and Kicliter, 1988; Wye-Dvorak et al., 1990; Singman and Scalia, 1990). We report that out of six distinct morphological subtypes of ganglion cell, two that have not been described before in any vertebrate project to the pretectum. Four other ganglion cell types, which may be homologous to those seen in other vertebrates, project to the tectum. This projection is arranged retinotopically and the density of these types in different areas of the retina is correlated with the tectal behavior they may induce.

4.1 Materials and methods

Experiments were performed on a total of 56 young adult (15–18 cm) sea lampreys (Petromyzon marinus) and 12 adult river lampreys (Lampetra fluviatilis). The experimental procedures were approved by the local ethical committee (Stockholm's NorraDjurfo¨ rso¨ ksetiska Na¨ mnd) and were in accordance with The Guide for the Care and Use of Laboratory Animals (National Institutes of Health, 1996 revision). During the investigation, every effort was made to minimize animal suffering and to reduce the number of animals used.

Experimental preparation

The animals were deeply anesthetized in tricane methane sulfonate (MS-222; 100 mg/L; Sigma, St. Louis, MO) diluted in fresh water. They were then transected caudally at the seventh gill and the dorsal skin and cartilage were removed to expose the brain. During the dissection and the injections, the head was pinned down and submerged in ice-cooled oxygenated HEPES buffered physiological solution (138 mM NaCl, 2.1 mM KCl, 1.8 mM CaCl2, 1.2 mM MgCl2, 4 mM glucose, and 2 mM HEPES), pH 7.4.

The meninges surrounding the optic tectum were removed with fine forceps and small 1-mm squares of filter paper, soaked in collagenase solution (1 mg/mL in distilled water), were applied to the dorsal surface of the exposed tectum. Following two 15-minute applications of the enzyme, the membrane covering the tectum could be removed. This was done to ensure that the injection micropipette could penetrate the tissue with maximal ease.

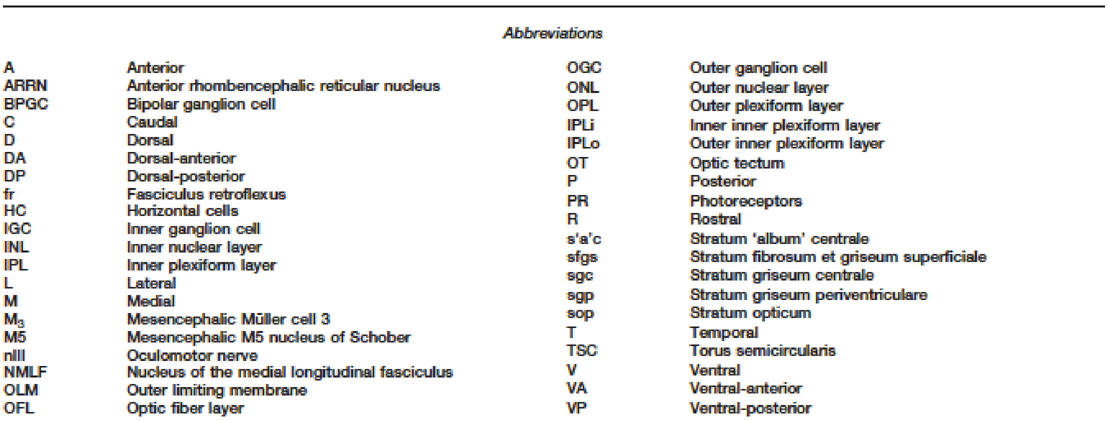

Abbreviations

A	Anterior	OGC	Outer ganglion cell
ARRN	Anterior rhombencephalic reticular nucleus	ONL	Outer nuclear layer
BPGC	Bipolar ganglion cell	OPL	Outer plexiform layer
C	Caudal	IPLi	Inner inner plexiform layer
D	Dorsal	IPLo	Outer inner plexiform layer
DA	Dorsal-anterior	OT	Optic tectum
DP	Dorsal-posterior	P	Posterior
fr	Fasciculus retroflexus	PR	Photoreceptors
HC	Horizontal cells	R	Rostral
IGC	Inner ganglion cell	s'a'c	Stratum 'album' centrale
INL	Inner nuclear layer	sfgs	Stratum fibrosum et griseum superficiale
IPL	Inner plexiform layer	sgc	Stratum griseum centrale
L	Lateral	sgp	Stratum griseum periventriculare
M	Medial	sop	Stratum opticum
M_3	Mesencephalic Müller cell 3	T	Temporal
M5	Mesencephalic M5 nucleus of Schober	TSC	Torus semicircularis
nIII	Oculomotor nerve	V	Ventral
NMLF	Nucleus of the medial longitudinal fasciculus	VA	Ventral-anterior
OLM	Outer limiting membrane	VP	Ventral-posterior
OFL	Optic fiber layer		

Retrograde tracing.

Once the membrane over the optic tectum was removed, 50–200 nL of fluorescently coupled 3 or 10 kD dextrans (Texas Red, Fluorescein or Alexa 488; Molecular Probes Europe, the Netherlands; 12% in distilled water) or neurobiotin (Vector, Burlingame, CA; 20% in distilled water containing fast green to aid visualization of the injected tracer) were pressure-injected unilaterally or bilaterally into the superficial layers (see list of abbreviations, sfgs and sop) of the optic tectum ($n = 43$) or into the pretectum ($n = 6$). The neurobiotin injections covered the whole surface of one tectal hemisphere and were used for the analysis of the retinal ganglion cells. For optic nerve injections ($n = 7$) the brain was dissected out leaving the optic nerves and optic chiasm intact. 20% neurobiotin was then injected into the optic nerve, at the entry to the optic chiasma. Glass (borosilicate, OD = 1.5 mm, ID = 1.17 mm) micropipettes, with a tip diameter of 10–20 _m, were made using a Narishige vertical puller. The micropipettes were fixed in a holder, which was attached to an air supply and a Narishige micromanipulator. The size of the injection and the spread of the tracer were monitored by visual inspection. After a pause of 10–15 minutes, to allow the tracer to diffuse, the injection was repeated to ensure that a sufficient amount of tracer was injected in as small an area as possible. Following injection the head was kept submerged in HEPES in the dark at 4°C for 24–48 hours to allow retrograde transport of the tracer.

Dissection and histology.

The contralateral and the ipsilateral eyes were dissected from the head and careful attention was paid to ensure that the orientation of the eye was known even after it was removed from the cranium. Four incisions were then made in each eye at the four poles (dorsal, ventral, anterior, and posterior), from the lens extending almost to the optic nerve. The lens was then removed and the remainder of the eye was laid flat so that the retinal surface was exposed. The flat retinas were flipped so that the pigment layer was facing up; this was then removed with fine forceps. The retinas were mounted flat on slides and allowed to dry before being mounted in glycerol containing 2.5% diazabicyclanooctane (Sigma).

The brains were then dissected out of the surrounding tissue and fixed by immersion in 4% formalin and 14% saturated picric acid in 0.1 M phosphate buffer (PB), pH 7.4, for 12 hours, after which they were cryoprotected in 20% sucrose in PB for 3 hours. Thirty-_m-thick transverse sections were made using a cryostat, collected on gelatin coated slides, and coverslipped in the same solution as the retinas. For analysis of the neurobiotin retrogradely labeled retinal ganglion cells, the retinas were dissected as above and immersed in fixative for 2 hours followed by 2 hours in 20% sucrose, before 40-_m-thick transverse (through the dorsoventral axis) cryostat sections were made. The sections were subsequently incubated with Cy2/Cy3 conjugated streptavidin (1:1,000; Jackson Immunoresearch, West Grove, PA) and NeuroTrace red/green fluorescent Nissl stain (1:500; Molecular Probes) diluted in 1% bovine serum albumin (BSA), 0.3% Triton X-100 in 0.1 M PB for 2 hours.

Analysis

Transverse brain sections from the pretectum to the rostral rhombencephalon were analyzed using a Nikon fluorescence microscope to locate the injections sites. Photomicrographs of key results were taken with a Zeiss Axiocam digital camera (Carl Zeiss, Stockholm, Sweden), while the location of the injection site was mapped on schematic drawings of transverse sections through the lamprey brain. All injections are mapped on one side of the schematics irrespective of their actual lateralization to facilitate comparison of injection sites. These drawings were made in Adobe Illustrator CS2 (San Jose, CA) from serial transverse Nissl-stained sections. Illustrations were prepared in Adobe Photoshop CS2. The retinas were analyzed with the same equipment as above. The location of labeled retinal fibers was mapped instantly after mounting to ensure that the labeling did not fade. The retinal projections were mapped on retinal schematics and photomicrographs of the retinal projections were taken.

The sectioned retinas were analyzed to determine the distribution of the retinal ganglion cell types. A third party person randomly ordered the slides, each containing ~15 sections, so that the order of the sections was blinded before counting. To systematically randomize which sections were counted, every fifth section was analyzed; in this way 20% of each retina was sampled. We divided up each section into counting areas using a 10 mm eye piece graticule. By counting profiles in every fifth section we ensure that each profile belongs to a single cell, thereby reducing the error in counting single cells multiple times. To ensure that we do not overestimate the number of large-diameter cells we applied the Abercrombie correction factor to our results (Abercrombie, 1946). The soma diameters in the z plane were estimated in a confocal microscope.

For statistical analysis, the data from five ipsilateral and five contralateral retinas were divided up into four-by-four areas and averaged (see Fig. 1D,E). Sections were grouped according to which part of the anterior/posterior retina they were from, anterior-lateral, anterior-medial, posterior-medial, or posterior-lateral, each group contained five analyzed sections per retina. For the dorsoventral axis, each section that uninterruptedly spanned the retina was divided into four equal counting areas using the eye piece graticule and where the retinal cut split the sections each portion of the section was divided into two equal areas. This resulted in each retina being divided up into a four-by-four grid. The profiles counted in each area of the grid were converted to cell density, using the measured length of the area and the known thickness of the section. These cell densities within each area of the grid were then averaged. The cell densities from corresponding grid locations from the five retinas were then averaged and the standard error of the mean was calculated.

To calculate whether there was any significant difference in the cell density across the retina we compared the profile counts from different parts of the retina. For example, the posterior lateral edge (20 points; four from each of the five retinas) were compared to the 20 points from the anterior edge using a two-way unpaired (two-sample) t-test. Confocal Z-stacks of the sectioned retina were obtained using a Zeiss Laser scanning microscope 510 and the projection images were processed using the Zeiss LSM software to verify the 3D shape of the retinal ganglion cells. The soma area (20 cells of each type) was measured from images taken with an Olympus BX51 microscope using the image acquisition program CellA (Olympus soft imaging solutions).

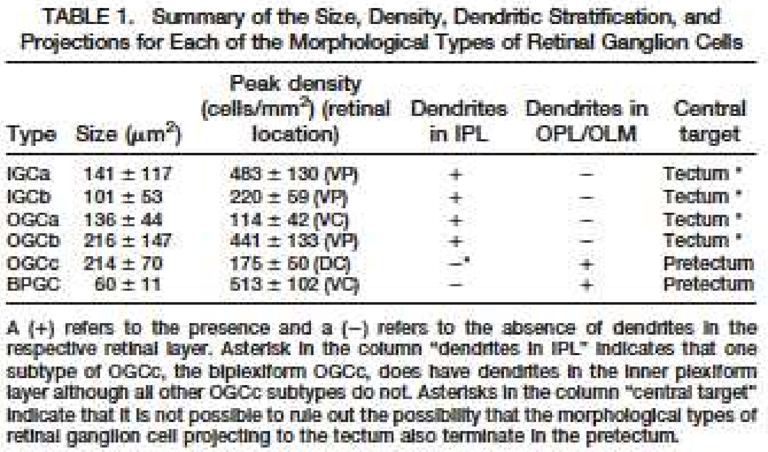

TABLE 1. Summary of the Size, Density, Dendritic Stratification, and Projections for Each of the Morphological Types of Retinal Ganglion Cells

Type	Size (μm^2)	Peak density (cells/mm^2) (retinal location)	Dendrites in IPL	Dendrites in OPL/OLM	Central target
IGCa	141 ± 117	483 ± 130 (VP)	+	–	Tectum *
IGCb	101 ± 53	220 ± 59 (VP)	+	–	Tectum *
OGCa	136 ± 44	114 ± 42 (VC)	+	–	Tectum *
OGCb	216 ± 147	441 ± 133 (VP)	+	–	Tectum *
OGCc	214 ± 70	175 ± 50 (DC)	–*	+	Pretectum
BPGC	60 ± 11	513 ± 102 (VC)	–	+	Pretectum

A (+) refers to the presence and a (–) refers to the absence of dendrites in the respective retinal layer. Asterisk in the column "dendrites in IPL" indicates that one subtype of OGCc, the biplexiform OGCc, does have dendrites in the inner plexiform layer although all other OGCc subtypes do not. Asterisks in the column "central target" indicate that it is not possible to rule out the possibility that the morphological types of retinal ganglion cell projecting to the tectum also terminate in the pretectum.

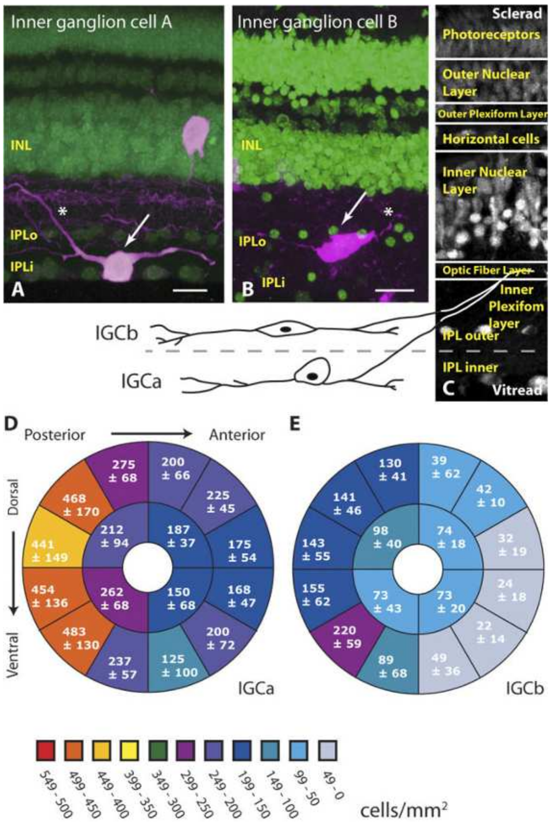

Figure 1.
Photomicrographs of the two types of inner ganglion cells (IGC), labeled after optic nerve injections, with their distribution in the retina. A,B: Confocal images of the retina (green = fluorescent Nissl stain) with the two types of retinal ganglion cells in red, IGCa (A) and IGCb (B). The arrows point at the soma of the cells described and the asterisks indicate their axons. The inner nuclear layer (INL) and the outer (IPLo) and inner (IPLi) sublayers of the inner plexiform layer are indicated. C: Nissl-stained section of the retina with a schematic representation of IGCa and IGCb. The retinal layers are indicated, as are the sclerad and vitread sides of the retina. D,E: Schematic representation of the retinas showing how the cell densities, of the IGCa (D) and IGCb (E), vary across the retina. Scale bars = 20 µm.

4.2 Results

We will report our findings with regard to the six morphological types of retinal ganglion cells and their projections to their two target areas for visuomotor coordination, tectum and pretectum, in the following sequence: 1) A description of six different types of ganglion cells based on retrograde labeling from the optic nerve. 2) The retinotopic map onto the tectum. 3) The projection pattern of four types of ganglion cells onto tectum. 4) The projection pattern on to the pretectum of two ganglion cell types not projecting to the tectum. Types of retinal ganglion cells Injections into the optic nerve, at the level of the optic chiasm, resulted in labeling of retinal ganglion cells in all areas of the retina. The retinal ganglion cells observed were classified based on the location of the soma and the dendritic stratification. First, cells were classified based on the location of their soma, which were observed in both the inner nuclear layer and the inner plexiform layer, termed inner (IGCs) and outer ganglion cells (OGCs), respectively, in accordance with the nomenclature used by Fritzsch and Collin (1990). Second, the IGCs were further subdivided as their somata were located in one of two distinct inner plexiform sublayers, here referred to as inner plexiform outer (IPLo) and inner (IPLi), in accordance with Villar-Cheda et al. (2006). The OGCs were also subdivided based on the location of their soma within or on the border of the outer nuclear layer. Third, the cells were classified according to whether their dendrites terminated in the inner plexiform layer, the outer plexiform layer, or the outer limiting membrane. Based on the soma location alone, we distinguish four groups of retinal ganglion cells. By including the additional criteria of dendritic stratification these can be further subdivided, resulting in a total number of six types of retinal ganglion cell in the lamprey *P. marinus*.

Retinal ganglion cells with dendrites in the inner plexiform layer. Inner ganglion cells.

The somata of the IGC's are situated in one of the two inner plexiform sublayers (Fig. 1A–C). The IGCa somata are situated in IPLi (Fig. 1A), the processes of these cells are all, except for the axon, located within this inner plexiform sublayer (Fig. 1A, Table 1). Once the axons have left the inner plexiform sublayer they pass sclera toward the optic fiber layer. Axon collaterals that branch off after the axon has left the inner plexiform sublayer turn and return to the sublayer they originated from (Fig. 1A). The cell bodies of these cells are round and with an average size of 141 ± 117 μm^2. The IGCa cells were nonuniformly distributed throughout the retina, with the highest density in the ventralposterior retina (483 ± 130 cells/mm^2; Fig. 1D, Table 1). Over the entire retina there was a 2.5 times increase in IGCa cell density from the anterior to the posterior retina. There was a significant difference in the cell densities between the posterior-lateral as compared with the posterior-medial ($P < 0.01$), the anterior-medial ($P < 0.01$) and the anterior-lateral ($P < 0.01$) retina (Fig. 1D). However, there was no significant difference between the dorsal and ventral retina ($P = 0.3$).

The somata of the other subtype, IGCb, are located in the second sublayer of the inner plexiform layer (IPLo) situated closer to the optic fiber layer (Fig. 1B,C). The dendrites and axons of these cells also pass within the plane or sclerad of their inner plexiform sublayer and are never observed passing vitread toward the other inner plexiform sublayer. The soma of IGCb cells were oval-shaped as opposed to round, with an average soma area of 101 ± 53 μm^2 (Table 1). The distribution of IGCb cells throughout the retina was similar to that of the IGCa with the highest density in the ventral-posterior retina (220 ± 59 cells/mm^2; Fig. 1E, Table 1). There was a significant difference in the cell densities between the posterior-lateral as compared with the posterior-medial ($P < 0.01$), the anteriormedial ($P = 0.015$) and the anterior-lateral ($P < 0.01$) retina. However, there was no significant difference between the dorsal and ventral retina ($P = 0.29$). While the IGCa and b cells were distributed in a similar pattern across the retina there were on average 2.2 times fewer IGCb cells in any given area of the retina. Following optic nerve injections, nonretrogradely labeled cells were also observed in both inner plexiform sublayers (Fig. 1A,B).

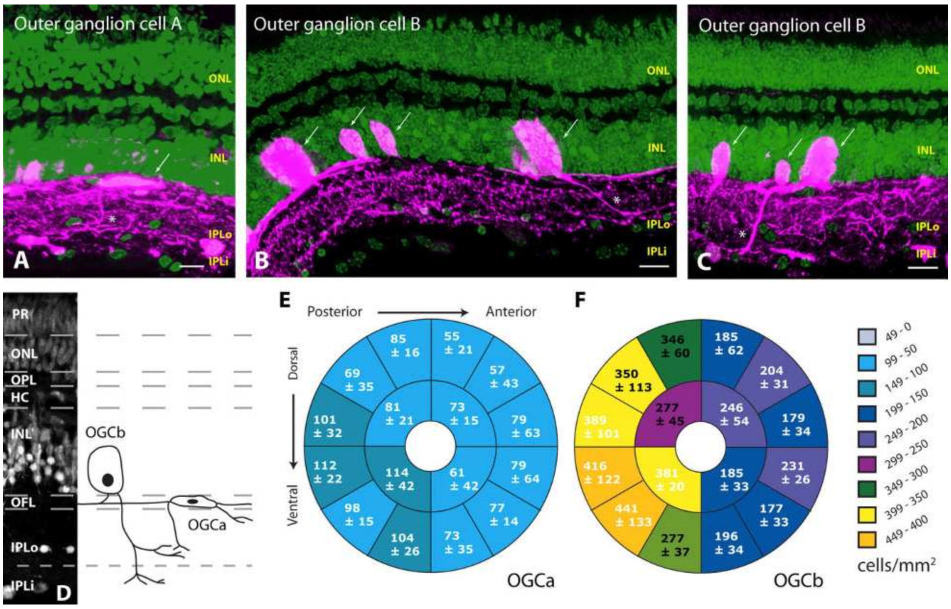

Figure 2. *Photomicrographs of the outer ganglion cells, OGCa and OGCb, labeled after optic nerve injections, with their distribution in the retina. A–C: Confocal images of the retina (green = fluorescent Nissl stain) with ganglion cells in red, OGCa (A) and OGCb (B,C). The arrows point at the soma of the cells described and the asterisks indicate their*

axons. The outer nuclear layer (ONL), inner nuclear layer (INL), and the outer (IPLo) and inner (IPLi) sublayers of the inner plexiform layer are indicated. D: Nissl-stained section of the retina with schematic representation of OGCa and OGCb. E,F: Schematic representation of the retinas showing how the cell densities, of the OGCa (D) and OGCb (E), vary across the retina. The retinal layers are indicated with abbreviations. Scale bars = 20 µm.

Outer ganglion cells.

The somata of the OGCa and OGCb are located in or on the border of the inner nuclear layer (Fig. 2A–D). The dendrites of OGCa and OGCb pass into the inner plexiform layer (Fig. 2A–D, Table 1). The OGCa somata are located on the vitread border of the inner nuclear layer and have oval somata that were on average 136 ± 44 µm2 (Fig. 2A,D, Table 1). Their dendrites pass both within the plane of their cell body and into the outer inner plexiform sublayer (IPLo). The axons of these cells have a characteristic collateral that branches at a 90° angle just after the axon has left the soma. This collateral then passes into the inner plexiform layer but as with the dendrites it does not pass the outer inner plexiform sublayer (IPLo). All processes of these cells are therefore situated vitread of the optic fiber layer (Fig. 2A,D). The OGCa cells are uniformly distributed throughout the retina with the highest density of 114 ± 42 cells/mm2 in the ventral-medial retina (Fig. 2E, Table 1). There was no significant difference between the density of OGCa in the posterior and the anterior retina or between the ventral or the dorsal retina. The somata of OGCb cells, in contrast to OGCa, are located in the midst of the inner nuclear layer and are bell-shaped, with an average size of 216 ± 147 µm2 (Fig. 2B–D, Table 1). These cells characteristically have their axon and a thick primary dendrite emanating from their vitread border (Fig. 2B–D). Unlike the other cell types, dendrites from these cells can be observed in both inner plexiform sublayers. All the processes of this cell type, like those of the OGCa, are observed vitread of the optic fiber layer. These cells are nonuniformly distributed throughout the retina with the highest density of 441 ±133 cells/mm2 in the ventral-posterior retina (Fig. 2F, Table 1). There was a 2.3 times increase in cell density from the anterior to posterior retina. There was a significant difference in the cell densities between the posterior-lateral as compared with the posterior-medial ($P = 0.03$), the anterior-medial ($P < 0.01$), and the anterior-lateral ($P < 0.01$) retina. However, there was no significant difference between the dorsal and ventral retina ($P = 0.76$).

Retinal ganglion cells with dendrites in the outer plexiform layer.

Outer ganglion cells. In contrast to the ganglion cells mentioned above, OGCc’s have dendrites and axon collaterals that run on the sclerad side of the optic fiber layer (Fig. 3A–C,G). These cells all have dendrites that pass through the inner nuclear and horizontal cell layer to ramify in the outer plexiform layer (Fig. 3A–C,G, Table 1). However, unlike the other cell types described their morphology is not uniform. Three different morphologies are observed: cells with only dendrites projecting to the outer plexiform layer (Fig. 3A) whose soma are cone-shaped and taper to a single axonal process are termed OGCc1. Cells with dendrites and axon collaterals projecting to the outer plexiform layer (Fig. 3B) are called OGCc2, and biplexiform cells with dendrites both projecting to the outer and inner plexiform layers are called OGCc3 (Fig. 3C). Those cells with axon collaterals projecting to the outer plexiform layer adhere to a strict pattern. The axon collaterals are never seen innervating the same region as the dendrite, rather they terminate symmetrically on either side of the dendrite in the outer plexiform layer. The distance between the axon collateral and the dendrite may vary, but if it does, it is symmetrical with equal distance between each collateral and the dendrite. The somata of OGCc are large 214 ± 70 µm2 and nonuniformly distributed throughout the retina, with the highest density, 175 ± 50 cells/mm2, in the central retina (Fig. 3D, Table 1). There is a statistically significant increase in the density of cells in the central retina as compared with the periphery ($P > 0.01$).

Bipolar ganglion cells.

The final class of retinal ganglion cell resembles classical bipolar cells (retinal interneurons) described in the lamprey and other vertebrates. Therefore, these ganglion cells are here referred to as bipolar ganglion cells. Their somata are small (60 ± 11 µm2), located in the inner nuclear layer, and are bipolar with a primary dendrite emanating from the slerad side of the soma and an axon from the vitread side (Fig. 3E,G, Table 1). The dendrites project through the inner and outer nuclear layer to terminate in the region of the outer limiting membrane (Fig. 3E,G, Table 1). The axons of these cells project through the optic fiber layer to the inner plexiform layer, as is the case with classical bipolar cells, and in addition these cells contribute an axon to the axon bundles that leave through the optic nerve (Fig. 3E). These cells are only observed in a very small area of the retina ~400 by 650 µm, located in the vertical midline just ventral of the optic nerve, with the largest average cell density of all types of retinal ganglion cell (513 ± 102 cells/mm2; Fig. 3F, Table 1).

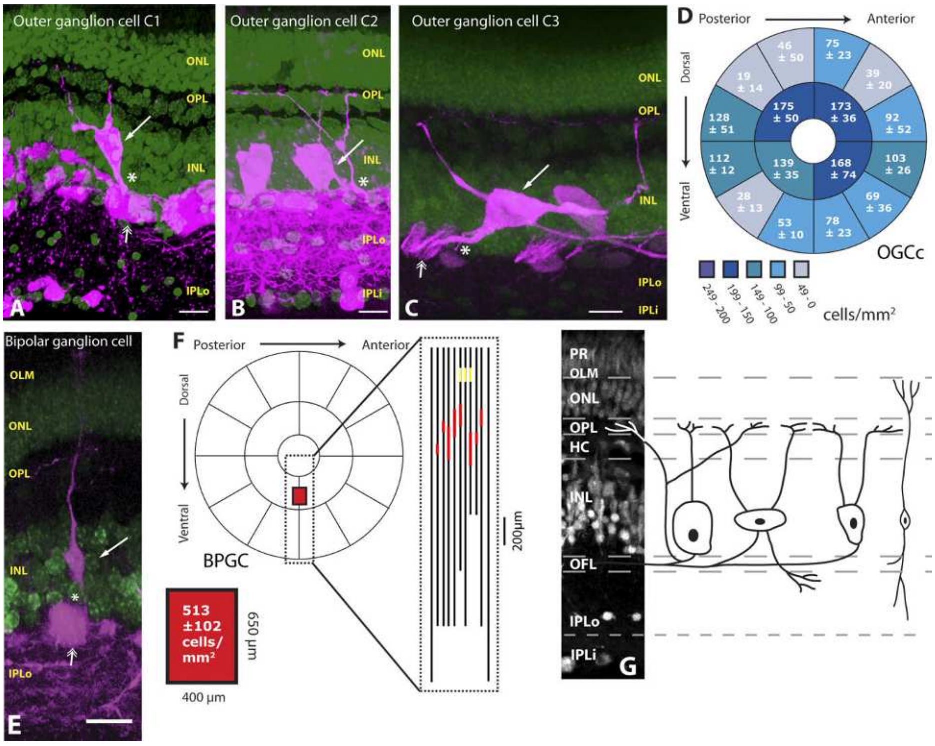

Figure 3.*Photomicrographs of the outer ganglion cells c (OGCc1–3) and bipolar ganglion cells (BPGC) labeled after optic nerve injections, with their distribution in the retina. A–C: Confocal images of the retina (green = fluorescent Nissl stain) with OGCc ganglion cells in red. The arrows point at the soma of the cells described and the asterisks indicate their axons. The double arrowheads indicate a fascicle of axons. D: Schematic representation of the retina showing how the cell density of the OGCc varies across the retina. E: Confocal image of the retina (green = fluorescent Nissl stain) with the bipolar ganglion cell in red. The arrow points at the soma of the cell described and the asterisk indicates the axon. The double arrowhead indicates a fascicle of axons. F: Schematic representation of the retina showing the location of the bipolar ganglion cells. Twelve consecutive sections, aligned to the optic nerve or where the axon fascicles converge, showing the location of the bipolar ganglion cells in red and the optic nerve in yellow. G: Nissl-stained section of the retina with schematic representation of a bipolar ganglion cell and OGCc cells. The retinal layers are indicated with abbreviations. Scale bars = 20 µm.*

4.2.1 Retinotectal projections

Macroscopic arrangement. In order to understand how the retinotectal projection is arranged, we made multiple injections in the tectum to observe which areas of the retina innervate different areas of the tectum. To correlate tectal injection sites with retinal locations, we first defined the rostrocaudal and mediolateral axes through the optic tectum.

The division between the rostral and caudal tectum was drawn immediately before the closure of the 3rd ventricle (Fig. 4A). The separation between the medial and lateral tectum was made at the extreme dorsolateral surface (Fig. 4A). Here the tectum extends ventrally, so the ventral pole of the threedimensional tectum would correspond to the lateral edge if the structure was flattened (Fig. 4A). This means that any injection into the dorsal surface of the tectum is in the medial half of the tectum and any injections in the ventral surface of the tectum are in the lateral half of the tectum. The tectal strata with the superficial (sfgs and sop) and the deeper (sgc_s‘a’c and sgp) layers of the optic tectum can be seen in Figure 4B. Following the dissection, the whole-mount retinas appear in the shape of a four-leaf clover with four obvious quadrants (dorsal-anterior, DA; dorsal-posterior, DP; ventral-anterior, VA; and ventral-posterior, VP). During the course of the experiments we analyzed retrograde labeling in all four quadrants of the contralateral and ipsilateral retina. In all the retinal whole-mounts that contained labeling we observed retrogradely labeled fibers that passed through the optic nerve and then diverged across the retina. During the analysis the observed projections were mapped on to schematic retinas, circles divided into four quadrants (Fig. 4G).

Retinotectal organization.

An example of retrograde labeling in a retinal whole-mount, following a tectal injection, can be seen in Figure 4D. Texas Red-dextran was injected into the most caudomedial portion of the tectum (Fig. 4C, red) and fluorescein-dextran (Fig. 4C, green) was injected into the same tectal hemisphere in the middle of the medial tectum. Here we observe two distinct injections in the same tectal hemisphere that give rise to retrogradely labeled fibers in different parts of the retina (Fig. 4D,G). The Texas Red retrogradely labeled fibers in the contralateral retina were observed spreading from the optic nerve toward the anterior retinal edge (Fig. 4D,G). The injection of fluorescein into the middle part of the medial tectum results in labeling in the whole contralateral ventral retina (Fig. 4D,G). No labeling was observed in the ipsilateral retina. The injection sites are in close approximation and may overlap in the rostrocaudal midline; axons that terminate in this region may therefore take up both tracers and appear orange. This colocalization of tracers is observed within the most anterior part of the ventralanterior retinal quadrant. This shows that there is a smooth transition from ventral to anterior retina innervation along the rostrocaudal axis of the medial tectum. The degree of separation observed in the retina is also maintained throughout the optic tract and optic chiasm. The majority of retrogradely labeled fibers from each injection can be seen passing through the optic chiasm (Fig. 4E) and optic tract (Fig. 4F) in separate bundles, while a few fibers contain both tracers, as is the case in the retina. When the data from the 33 injected *P.marinus* were combined, the injected surface encompassed the entire superficial layer of the optic tectum and the corresponding labeled retinal segments also covered the entire retinal surface. Nine injections were chosen to illustrate the injected area of the tectum that corresponds to labeling of one of the contralateral retinal poles or labeling of the horizontal band and the ipsilateral retina (Fig. 5A–D). These nine injections were sufficient to label the entire retinal surface and also covered the whole tectal surface. Injections in the lateral and medial tectum result in labeling in the dorsal and ventral retina, respectively (Fig. 5A,B). Injections spanning the medial-lateral midline result in labeling in both the dorsal and ventral retina (Fig. 5C,D) (for a dorsal view of the projection see Fig. 7). Injections in the rostral and caudal tectum give rise to labeling in the posterior and anterior retina, respectively (Fig. 5C,D). Retrograde labeling in the ipsilateral retina was observed when injections were made into the middle of the rostrocaudal and ventrodorsal axis.

The ipsilateral labeling observed was confined to the posterior retina, whereas the contralateral labeling was confined to the horizontal midline (Fig. 5D). We also confirmed that the retinotectal projection was organized in a retinotopic manner in another lamprey species, *L. fluviatilis*, which is commonly used in locomotor research. Here the contralateral retinal organization was the same as that of *P. marinus*, but we did not observe any labeling in the ipsilateral retina (data not shown).

4.2.2 Tectal projecting retinal ganglion cells

In order to understand which of the six types of retinal ganglion cells in the *P. marinus* retina project to the tectum, injections were made that covered the entire optic tectum. Following retrograde transport, the cells were visualized in transverse sections of the retina. Four of the six types of retinal ganglion cells, both types of IGC as well as OGCa and OGCb, were observed in all areas of the contralateral retina following tectal injections (Fig. 6A,B). These four types of ganglion cell were also observed in the ipsilateral retina but were confined to the posterior retina, the area of the retina that receives information from the front of the visual field that is likely to be where there is binocular overlap (Fig. 6C). All four ganglion cell subtypes have their dendrites in the inner plexiform layer (Fig. 6D), but not in the outer layers in which OGCc and bipolar ganglion cells extend their dendrites.

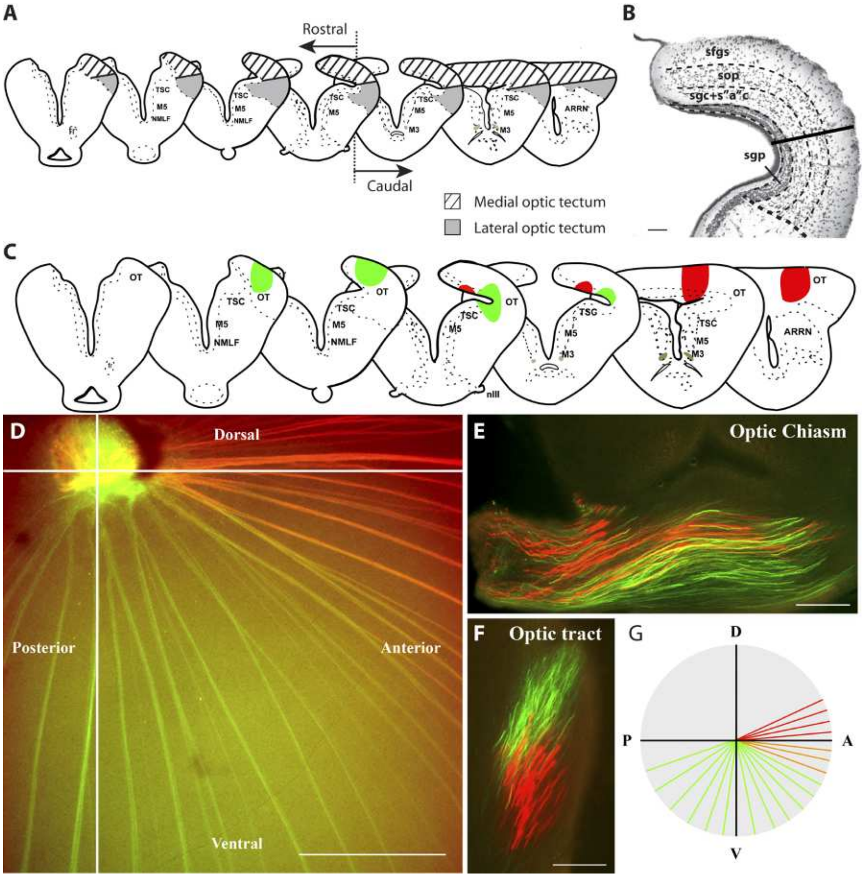

Figure 4.
Schematics of transverse sections through the lamprey optic tectum and retrograde labeling in the ventral and anterior retina of P. marinus. A: The defined rostrocaudal and mediolateral axes. B: A Nissl-stained transverse section of the optic tectum at the level of the rostrocaudal midline with dotted lines indicating the different tectal layers. The

superficial layers include the stratum fibrosum et griseum superficiale (sfgs) and the stratum opticum (sop). The deeper layers include stratum 'album' et griseum centrale (s'a'c and sgc) and the stratum griseum periventriculare (sgp). C: Schematics of transverse sections through the lamprey optic tectum showing the injection sites.
The injection of fluorescein, mapped in green, is located in the rostromedial optic tectum. The injection of Texas Red, mapped in red, is restricted to the most caudomedial part of the optic tectum. D: Magnified image of a retinal whole-mount showing retrogradely labeled fibers resulting from the injection of fluorescein in green and those from the injection of Texas Red in red. E: Photomicrograph of the optic chiasm showing retrogradely labeled fibers organized in separate bundles. F: Photomicrograph of the optic tract showing retrogradely labeled fibers organized in separate bundles. G: Schematic retina showing the retinal location of labeled fibers. A magenta/green version is provided as Supplementary Figure 1. Scale bars = 200 µm in B; 100 µm in D–F.

The distribution of tectal projecting OGCa, unlike the distribution pattern of OGCa labeled after optic nerve injection (cf. Fig. 2E), was nonuniform. There was no increase in cell density from anterior to posterior retina but rather there was an increase in cell density from the ventro- and dorsolateral to ventro- and dorsomedial retina (Fig. 6B). From the lateral edge to the horizontal retinal midline the cell density increased 2.2 times to a peak density of 105 ± 38 cells/mm2; this difference was statistically significant both from the ventral edge to the midline (*P* = 0.003) and from the dorsal edge to the midline (*P* = 0.004; Fig. 6B). The number of ganglion cells of this type or any tectal projecting type was not increased by performing multiple tectal injections. The density of OGCa was on average 18% lower than the density of OGCa's observed following optic nerve injections. The average soma size of OGCa labeled after tectal injections was 123 ± 44 µm2, there was no significant difference between these and the size of OGCa labeled after optic nerve injections (*P* > 0.05). Only the large OGCb was uniformly distributed throughout the retina, with the highest cell density of 163 ± 11 cells/mm2. The density of tectal projecting OGCb did increase slightly in the posterior retina, although this was not statistically significant (*P* = 0.09; Fig. 6B). This is in contrast to the nonuniform distribution of OGCb observed after optic nerve injections (cf. Fig. 2F). The density of tectal projecting OGCb's was on average 57% lower than the density of OGCb's observed following optic nerve injections. The average soma size of OGCb labeled after tectal injections was 261 ± 129 µm2; there was no significant difference between these and the size of OGCb labeled after optic nerve injections (*P* > 0.05). The IGCa and IGCb were nonuniformly distributed throughout the retina with similar patterns of distribution and with the highest density in the ventral-posterior retina, 181 ± 75 cells/ mm2 and 117 ± 48 cells/mm2, respectively (Fig. 6B), as was the case with the IGC's following optic nerve injections (cf. Fig. 1D,E). IGCa had the most dramatic increase in cell density with a 3.4 times increase from anterior to posterior retinal edge. There was a significant difference in the cell densities between the posterior-lateral and the anterior-medial (*P* = 0.025) or the anterior-lateral (*P* = 0.001) retina.

However, there was no significant difference within the posterior retina between the posterior-lateral and the posterior-medial part (*P* = 0.382). Nor was there any change in the cell density from the dorsal to the ventral retinal edge (Fig. 6B). The density of tectal projecting IGCa's was on average 66% lower than the density of IGCa's observed following optic nerve injections. The average soma size of an IGCa labeled after tectal injections was 83 ± 22 µm2, significantly smaller on average than the IGCa's labeled after optic nerve injection (*P* = 0.04). The largest soma area of a tectal projecting IGCa was 119 µm2, 27% of the IGCa labeled after optic nerve injections were larger than this, the largest having a soma size of 661 µm2. For IGCb, the increase in cell density was more modest, with a 2.4 times increase in cell density from anterior to posterior. There was only a statistically significant difference in cell density between the posterior-lateral and anterior-lateral retina (*P* = 0.004; Fig. 6B). The density of tectal projecting IGCb's was on average 30% lower than the density of IGCb's observed following optic nerve injections. The average soma size of IGCb labeled after tectal injections was 93 ± 30 µm2; there was no significant difference between these and the size of IGCb labeled after optic nerve injections (*P* > 0.05).

All four types of retinal ganglion cells were found in the ipsilateral retina following unilateral tectal injections, these cells were confined to the posterior retina (Fig. 6C). Of the four cell types, OGCa showed the highest density. This cell type's ipsilateral distribution was similar to that of the contralateral retina, with the highest density of retrogradely labeled cells found in the horizontal meridian, with a peak density of 54 ± 27 cells/mm2 (Fig. 6C). All other cell types were uniformly distributed throughout this area with low average cell densities of IGCa: 10 ± 3, IGCb; 8 ± 3, OGCb; 9 ± 2 cells/mm2 (data not shown).

Tectal locations.

In order to show the macroscopic tectal locations that receive specific visual input and to define the axes over which the input changes, color-coded contralateral (Fig. 7A) and ipsilateral (Fig. 7B) retinal locations are mapped onto a photograph of a *P. marinus* brain (Fig. 7C), as are the retinal ganglion cell densities (Fig. 7D). The posterior/anterior retinal axis can be seen running from the rostral tectum (posterior/ yellow; Fig. 7C) to the caudal tectum (anterior/purple; Fig. 7C). The areas of the optic tectum that receive input from both the anterior and posterior halves of the retina are located in the midline of this axis; for example, the area that receives input from the ventral retina has to receive input from both the VA and VP portion of the retina and is located in the midline of the rostrocaudal axis (V in Fig. 7C). Deviations from this midline in the rostral direction reveal areas that receive input predominantly from the posterior retina and vice versa, deviations in the caudal direction reveal areas that receive input predominantly from the anterior retina. A second axis runs from the medial to the lateral tectum corresponding to the ventral/dorsal retinal axis (green/red in Fig. 7C). The retinal input that an area receives depends on its position with respect to these two axes.

The area where the boundaries between A/P and D/V meet is innervated by the characteristic horizontal retinal pattern. What is interesting is that despite this location, also being on the boundary of the D/V axis, it does not receive projections from the dorsal or ventral part of the retina specifically. This, as mentioned earlier, is also the only area that receives input from the ipsilateral retina (black in Fig. 7C). Due to the nonuniform distribution of retinal ganglion cells projecting to the tectum, different tectal areas receive different combinations of retinal ganglion cell input (Fig. 7D–F). The rostral tectum receives input from the posterior retina, which has a high density of all four types of retinal ganglion cells (Fig. 7D,F), whereas areas of the caudal tectum, both medially and laterally, receive input from the anterior retina that has a low density of OGCa and IGC's (Fig. 7F). The mediolateral midline of the tectum also receives a specific combination of retinal ganglion cell input coming from the area of the retina which has the highest density of OGCa (Fig. 7F).

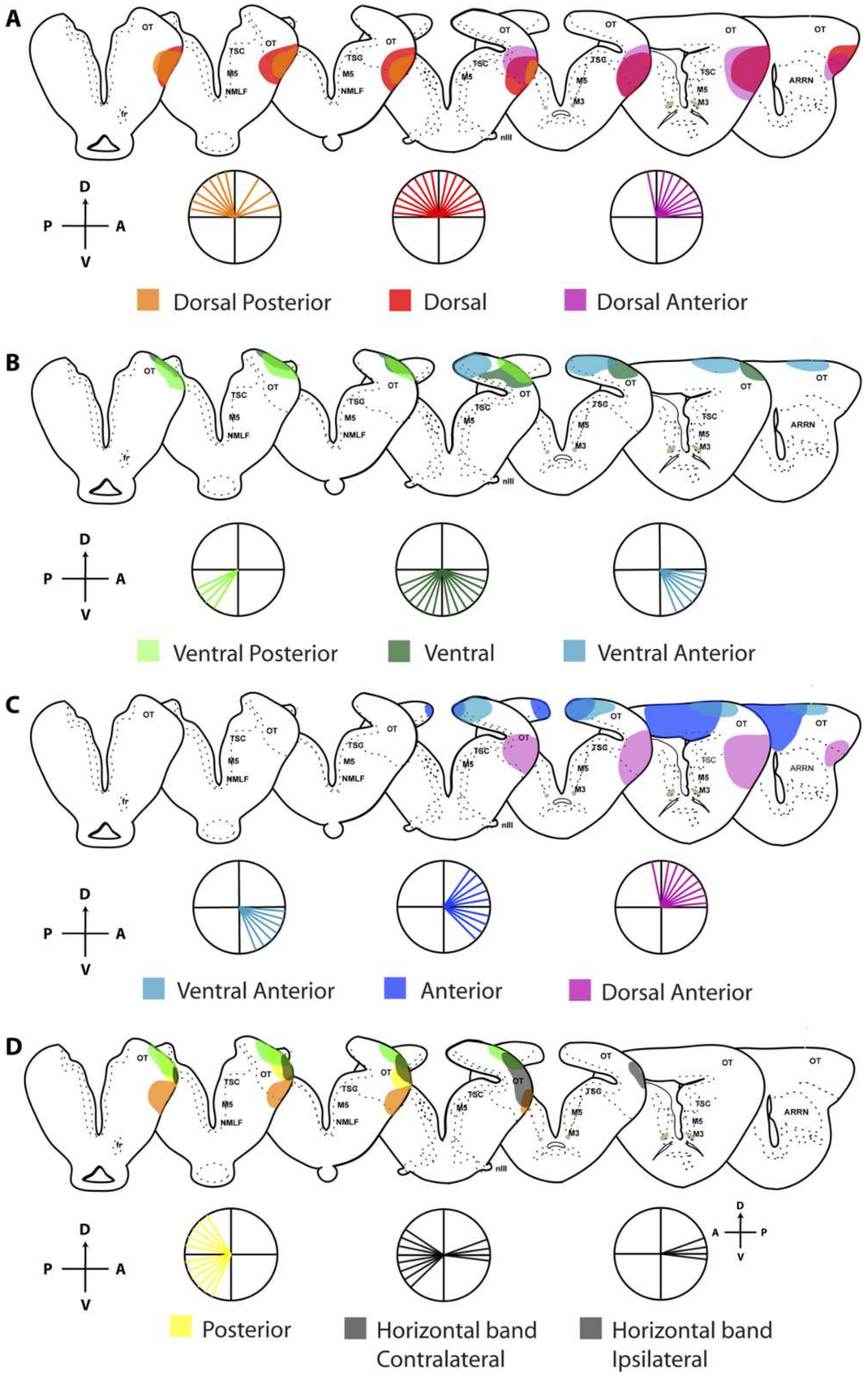

Figure 5*. Schematic drawings of transverse sections of the P. marinus optic tectum, showing the location of nine injection sites and the corresponding schematic retinal location of the retrograde labeling. A: Series one shows the location of three injection sites that give rise to labeling in the contralateral, dorsal, dorsal-anterior, and dorsalposterior retina. The injections are all restricted to the lateral portion of the optic tectum. B: Series two shows the location of three injection sites that result in labeling in the contralateral ventral, ventral-anterior, and ventral-*

posterior retina. These injection sites are all located in the medial optic tectum. C: Series three shows the location of three injection sites that give rise to contralateral labeling in the anterior, dorsal-anterior, and ventral-anterior retina. These three injections are located in the caudal tectum. D: Series four shows the location of four injection sites that give rise to labeling in the contralateral posterior, contralateral horizontal, and ipsilateral posterior retina. The injection sites are all restricted to the rostral portion of the optic tectum except the injection site that gives rise to labeling in the horizontal portion of the retina. This injection site is in the midline of both the rostrocaudal axis and the mediolateral axis.

4.2.3 Pretectal projecting retinal ganglion cells

In order to understand which of the six types of retinal ganglion cells in the P. marinus retina project to the pretectum, injections were made that covered the entire pretectum including the optic tract, which is innervated by the dendrites of pretectal neurons (Zompa and Dubuc, 1998). Retrograde labeling of ganglion cells with dendrites in the outer plexiform layer and at the outer limiting membrane (OGCc and bipolar ganglion cell) was observed in the contralateral retina following pretectal injections (Fig. 8A–C), as were the four types projecting to the tectum (see Fig. 6A–D). No labeling was observed in the ipsilateral retina. As the injection site included the optic tract we cannot rule out the possibility that axons from retinal ganglion cells passing to the tectum may take up the tracer and become labeled, despite not terminating in the pretectum. Due to this we are not able to make any conclusions about whether the four types of tectal projecting ganglion cells also terminate in the pretectum and they are therefore not considered further in this section of the results. Despite this, as the pretectal injections retrogradely labeled the bipolar ganglion cells and OGCc cells (Fig. 8A–D), which were never labeled following tectal injections, we can conclude that these two types of ganglion cell terminate in the pretectum. The bipolar ganglion cells, as those labeled after optic nerve injection, have small somata (53 ± 11 µm2) that were not statistically different in size ($P > 0.05$). They were located, as with the optic nerve injections, in only a small portion of the retina (400–650 µm), just ventral of the optic nerve (Fig. 8E). The density of these cells was not significantly different than that observed following optic nerve injections (548 ± 91 cells/mm2). To rule out the possibility that these cells were labeled by passage of the tracer through gap junctions from another ganglion cell in the retina, 3 kD dextran was injected, which due to its large size should not pass through gap junctions. The bipolar ganglion cells, along with all other ganglion cell types, were still labeled after 3 kD dextran was injected into the pretectum (Fig. 8A). Two morphological types of OGCc were also observed following pretectal injections (cf. Fig. 3A–C). These were the OGCc2, which have dendrites and axon collaterals projecting to the outer plexiform layer (Fig. 8B), and those that only send dendrites to the outer plexiform layer, OGCc1 (Fig. 8C). The biplexiform OGCc3, labeled after optic nerve injections, were never observed following pretectal injections. The size of the OGCc soma (182 ± 63 µm2) labeled after pretectal injections were not significantly different from those labeled after optic nerve injections ($P > 0.05$). The distribution of OGCc observed after these injections was similar to that observed following optic nerve injections; there was a statistically significant increase in the cell density in the central retina ($P < 0.01$). The average cell density, however, was 55% lower than that observed after optic nerve injections, with a peak density of 106 ± 45 cells/mm2.

4. 3 Discussion

Both the tectum and the pretectum are, as mentioned, involved in visually guided behaviors (see Vanegas, 1984). Here we show that each of these structures receives input from a different subset of the six distinct morphological types of retinal ganglion cell identified (see Fig. 9). All areas of the tectum receive input from four types of retinal ganglion cell, those that have dendrites in the inner plexiform layer. The areas of the tectum that induce evasive behavior receive input from areas of the retina with a low density of these four types, whereas the areas of the tectum that can induce both orienting and evasive behavior receive input from areas of the retina with a high density of these four types. The pretectum receives input from two ganglion cell types, OGCc and bipolar ganglion cells, that have not been described in other vertebrates. These cells send their dendrites to the outer plexiform layer or the outer limiting membrane and therefore bypass the image-forming architecture in the retina.

4.3.1 Retinal ganglion cells

The gross morphology of the agnathan retina is for the most part similar to that of the gnathostome retina, with its three nuclear layers and ganglion cells distributed throughout the ganglion cell and inner nuclear layer. Despite this, it differs in a number of ways, including the shifted position of the optic fiber layer (Fritzsch and Collin, 1990). The morphology and distribution of the *P. marinus* ganglion cells is here shown to have both similar and unique features when compared to the gnathostome vertebrates. One immediate striking difference is that in contrast to the gnathostome vertebrates, where ~98% of ganglion cells are located in the ganglion cell layer, in *P. marinus* only ~40% of the ganglion cells are located in this layer, both in the differentiated (present study) and the developing retina (Rubinson and Cain, 1989). This difference is even more pronounced in another lamprey species, *Ichthyomyzon unicuspis*, where the ganglion cell layer contains only a minority of ganglion cells (26%; Fritzsch and Collin, 1990).

The peak density of ganglion cells in the *P. marinus* retina was 1,270 cells/mm2 (present study), one of the lowest densities found in any vertebrate (Collin, 2008), suggesting that the density of ganglion cells may have been underestimated. However, as mentioned in the Results, multiple injections did not increase the number of ganglion cells labeled, suggesting that we labeled all tectal projecting ganglion cells. In addition, another lamprey species, *I. unicuspis* (Fritzsch and Collin, 1990), also has a comparatively low peak density, 3,600 cells/ mm2, indicating that a low density of ganglion cells may be a common feature for lamprey as compared with gnathostome vertebrates (see database, Collin, 2008).

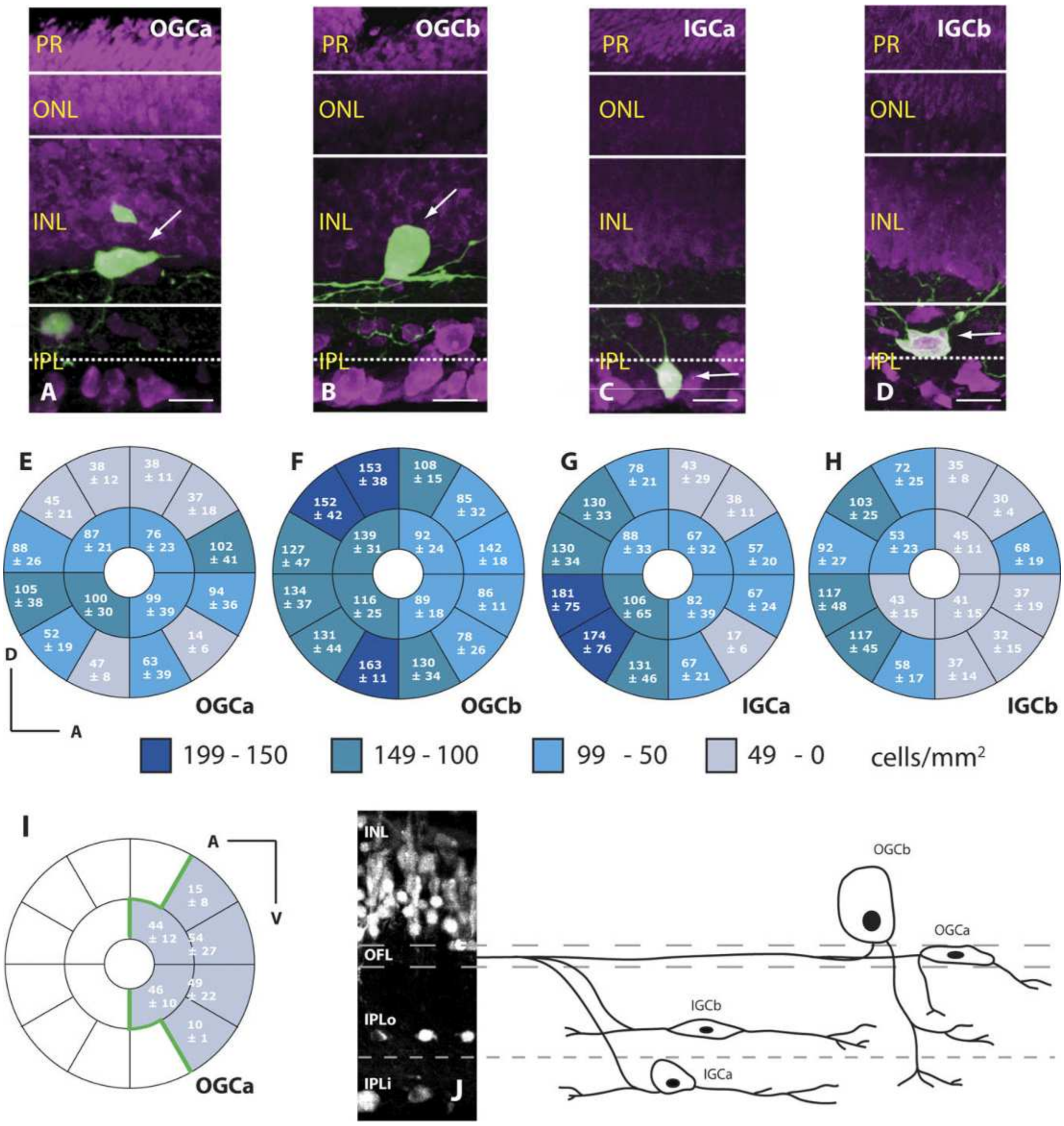

Figure 6.
Photomicrographs of the four morphological types of retinal ganglion cells labeled after tectal injections, with their distribution in the retina. A–D: Confocal images of the retina (red = fluorescent Nissl stain) with the four types of retinal ganglion cells in green The arrows indicate the cells that are described. E–H: Schematic representation of the contralateral retinas showing how the cell densities of the four types of ganglion cell vary across the retina. The highest density of OGCa located in the horizontal midline, the distribution of OGCb is close to uniform with a slight increase in the cell density in the posterior retina, the highest density of IGCa is in the posterior retina, the highest density of IGCb is in the posterior retina. I: Schematic representation of the ipsilateral retina showing how the OGCa cell density varies across the retina. The green line indicates the maximal area of the retina where labeled retinal ganglion cells of all types were found. J: Nissl-stained section of the retina, showing the inner nuclear, optic fiber, and inner plexiform layers with schematic representations of OGCa, OGCb, IGCa, and IGCb. Scale bars = 25 µm.

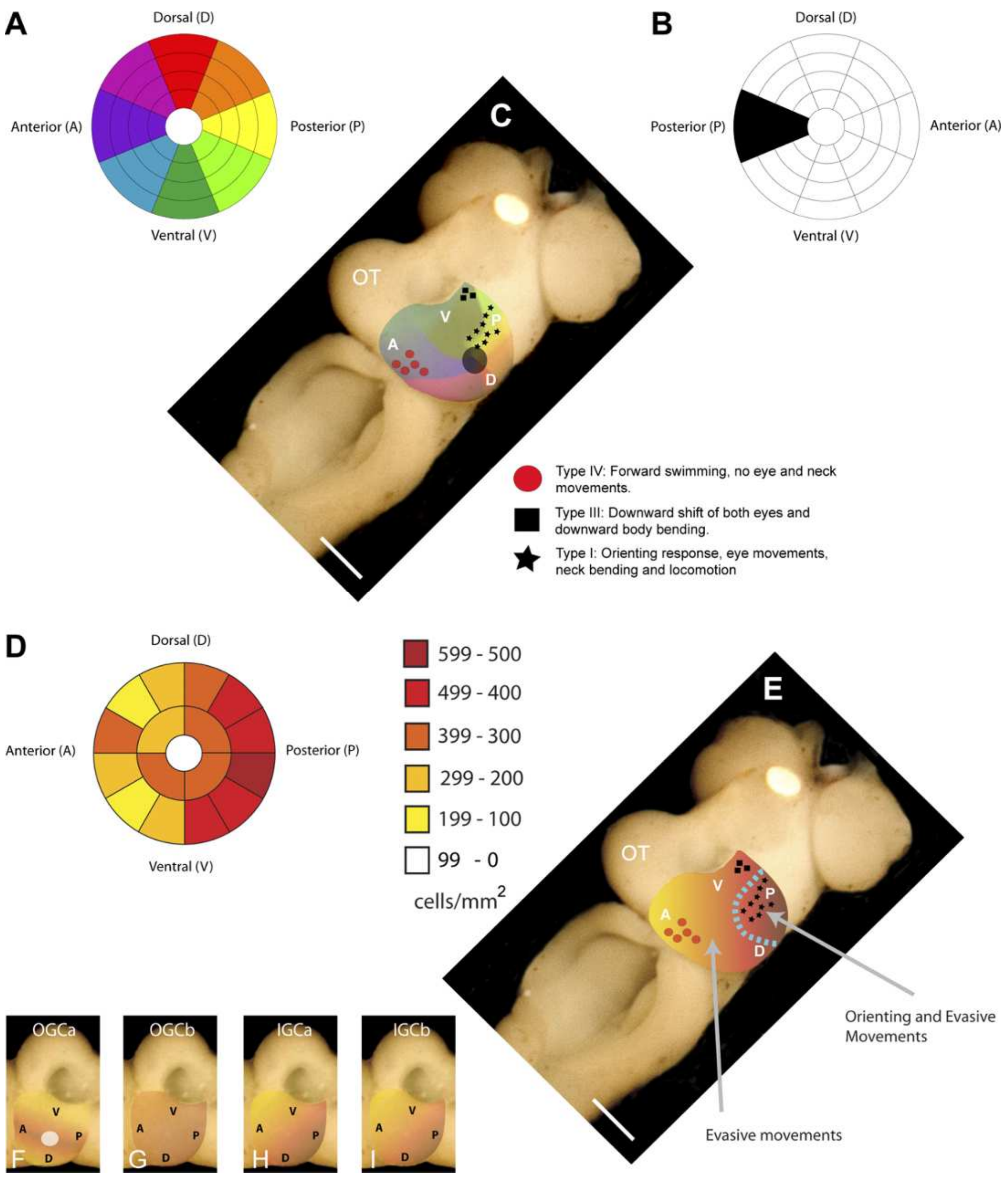

Figure 7. *Color-coded schematic retinas for the (A) contralateral and (B) ipsilateral eye. C: Photograph of the lamprey (P. marinus) brain showing the tectal locations of the color-coded retinal input. The retinal poles dorsal (D), ventral (V), anterior (A), and posterior (P) are marked with white letters on the optic tectum (OT). This shows the macroscopic arrangement of the retinal input with the posterior retinal input terminating in the rostral tectum, the anterior retinal input terminating in the caudal tectum, and the ventral and dorsal retinal input terminating in the medial and lateral optic tectum, respectively. In addition, this figure shows the tectal locations that when electrically stimulated give rise to Type I, III, and IV motor behaviors. These stimulation data have been previously described by Saitoh et al. (2007) and is here adapted to see the spatial overlap with the color coded retinotopic map. D: Schematic retina showing how the combined tectal projecting ganglion cell density is represented over the retinal surface. E: Photograph of the P. marinus tectum, showing how the combined total ganglion cell density is represented on the tectal surface. The stimulation locations from Saitoh et al. (2007) are spatially overlapped with this representation showing that the areas that when stimulated induce type IV and type III behavior receive input from areas of the retina that have a low cell density, whereas the area that when stimulated induces type I behavior receives input from the area of the retina which has the highest cell density of all four types of retinal ganglion cells. F–I: Photograph of the P. marinus tectum, showing how the difference in retinal cell density is represented on the tectal surface. Brown represents areas that receive input from areas of the retina with a high cell density, while orange represent areas of the tectum that receive input from areas of the retina with a low cell density. The mediolateral midline is the area of the tectum that receives*

input from the area of the retina with the highest density of OGCa. OGCb is approximately uniformly distributed throughout the retina with a slight increase in the posterior retina; this is represented on the tectal surface. The rostral tectum receives input from the area of the retina with the highest density of IGCa. The rostral tectum receives input from the area of the retina with the highest density of IGCb. Scale bars =_ 1 mm.

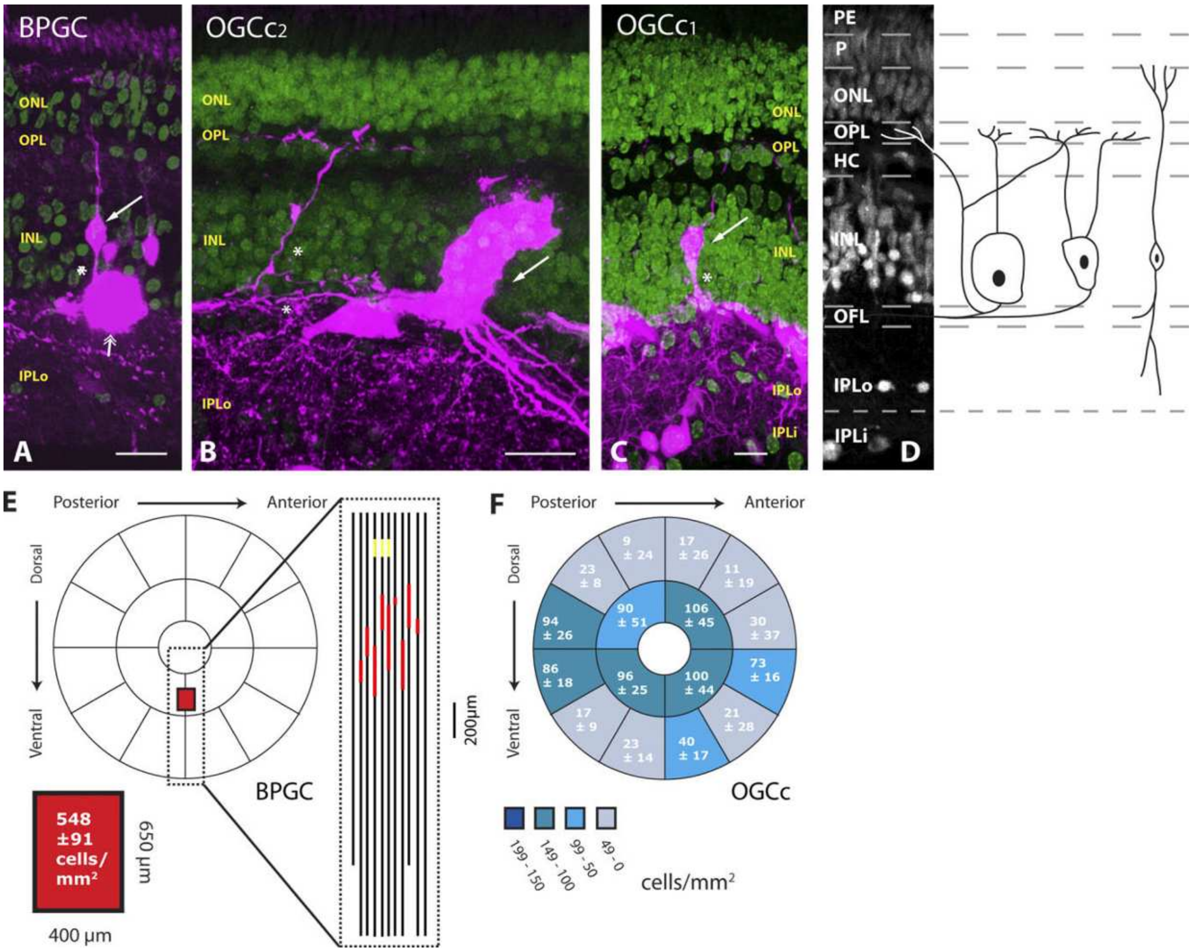

Figure 8.
Photomicrographs of ganglion cells, labeled after pretectal injections, with their distribution in the retina. A–C: Confocal images of the retina (green = fluorescent Nissl stain) with the ganglion cells in red, bipolar ganglion cell (3 kDa dextran tracer; A), and the OGCc (B,C). The arrows point to the cells of interest and the asterisks indicate the axons. The double arrowhead indicates a fascicle of axons. D: Nissl-stained section of the retina with schematic representation of a bipolar ganglion cell and OGCc. E: Schematic representation of the retina showing the location of the bipolar ganglion cells. Eleven consecutive sections, aligned to the optic nerve or where the axon fascicles converge, showing the location of the bipolar ganglion cells in red and the optic nerve in yellow. F: Schematic representation of the contralateral retina showing how the cell density of OGCc varies across the retina. Scale bars = 20µm.

Inner ganglion cells. The somata of IGCa and IGCb are located in one of the two inner plexiform sublayers; in addition, their dendrites and axon collaterals are confined to their respective sublayer. The presence of two ganglion cell sublayers in the lamprey inner plexiform layer is interesting to note, as there are also a number of sublamina in the gnathastome inner plexiform layer (Ramon y

Cajal, 1972). Here ganglion cells, depending on which sublamina their dendrites stratify in, respond to light with either an ON or OFF-center response as a consequence of connections with different populations of bipolar cells (Kuffler, 1953; Nelson et al., 1978). This is similar to the lamprey, where different types of bipolar cells have also been shown to terminate at different depths in the inner plexiform layer (Villar-Cheda et al., 2006). Furthermore, the processes of displaced amacrine cells in the inner plexiform layer of the lamprey also stratify in these two sublayers, as is the case with other vertebrates (Mariani, 1990; Pombal et al., 2003). The presence of displaced amacrine cells in the inner plexiform layer could explain why we observed nonretrogradely labeled cells in this layer, although we cannot rule out the possibility that some of these cells may have been unlabeled ganglion cells.

Outer ganglion cells. Biplexiform cells, first observed in the rhesus monkey (Mariani, 1982), have been identified in a large number of vertebrates, including macaques (Wa¨ ssle et al., 2000), mice (Doi et al., 1995), frogs (Toth and Straznicky, 1989), fish (Cook et al., 1996; Pushchin and Kondrashev, 2003), and lamprey (de Miguel et al., 1989; Fritzsch and Collin, 1990). This type of ganglion cell has dendrites that project to both the inner and outer plexiform layers, as is the case with the OGCc3 cells. The somata of the biplexiform cells are either located in the inner nuclear layer or in the ganglion cell layer, depending on the species. Despite this, due to the presence of biplexiform ganglion cells across the vertebrate phylum, it is unlikely that this cell type has evolved independently in each species but rather suggests that biplexiform ganglion cells may have been present in a common vertebrate ancestor. The biplexiform cell dendrites in the outer plexiform layer have been shown to directly contact photoreceptors in primates (Zrenner et al., 1983). In the lamprey L. fluviatilis, direct contacts between ganglion cells and photoreceptors have also been observed in the outer plexiform layer (Rio et al., 1998). These contacts were assumed to be between photoreceptors and biplexiform ganglion cells, as in other species, but may also be formed between the other morphological types of OGCc that we describe here, which are not biplexiform. OGCc2 cells have an additional surprising feature in that their axon collaterals enter the outer plexiform layer, which to our knowledge has never been observed in other vertebrates studied.

The OGCb morphologically resembles the classical cells of Dogiel (1883), as they are located in the same nuclear layer, have large bell-shaped soma, and have two primary processes, one axon and one primary dendrite, extending into the inner plexiform layer. These cells have been observed in a number of vertebrates (see Ramon y Cajal, 1972), including frogs (Singman and Scalia, 1990), and have been shown to respond to moving stimuli (Britto, 1983). These morphological similarities suggest that the OGCb may be homologous to the cell of Dogiel and potentially were present in the common ancestor before the agnathan and gnathostome vertebrates diverged.

Bipolar ganglion cells. One population of ganglion cells, observed in P. marinus, resembled bipolar cells. Morphologically similar ganglion cells have been observed in the developing retina in other vertebrate species including the lamprey, chick, rat, and cat retina (Nishimura, 1980; Maslim et al., 1986; de Miguel et al., 1989; Villar-Cervino et al., 2006). Here we demonstrate for the first time that bipolar ganglion cells are retained in an adult vertebrate. As these cells resemble a specific bipolar cell type that gives rise to the so-called Landolt's club, which is observed in a large number of vertebrate species, including lamprey (Villar-Cheda et al., 2006), lungfish (Locket, 1970), newt (Hendrickson, 1966), chicken (Shen et al., 1956), chimpanzee, and humans (Polyak, 1941), they could be interpreted as bipolar cells that contribute an axon to the optic nerve. However, in the developing P. marinus, retina cells that resemble these bipolar ganglion cells contain glutamate, which is not true for the bipolar cells (Villar- Cheda et al., 2006). These cells were interpreted as ganglion cells that transiently maintain their contact with the outer limiting membrane. In light of our results, one may conclude that these contacts are not transient but are retained in the adult animal. Interestingly, these cells also resemble the photoreceptor contacting neurons in other nonimage-forming photoreceptor organs, such as the teleost pineal organ (Ekstro ¨m, 1987) and the hagfish eye (Holmberg, 1970). The hagfish ganglion cells, which directly contact the photoreceptors, also resemble the bipolar ganglion cells described here in that they project predominantly to the pretectum and do not innervate the tectum (Kusunoki and Amemiya, 1983).

Tectal projecting retinal ganglion cells, retinotopy, and relation to behavior. Only four of the six morphological types of retinal ganglion cell were shown to project to the ipsilateral and contralateral tectum. These were the IGCa and b and OGCa and b, all of which have their dendrites in the inner plexiform layer. This is different from the majority of vertebrates studied, where all identified types of retinal ganglion cell project to the contralateral tectum/superior colliculus, (cat: Wassle and Illing, 1980; hamster: Chalupa and Thompson, 1980; mouse: Rapaport and Wilson, 1983; Hofbauer and Drager, 1985). One should note, however, that in these studies the types of retinal ganglion cell were determined purely on the basis of soma size and not on morphological characteristics. Indeed, in those cases that have examined the central projections of different morphological classes of ganglion cell (Karten et al., 1977; Rodieck and Watanabe, 1993; Martinez-Marcos et al., 2002; Ott et al., 2007) it was observed that only a subset of the morphological classes project to the tectum. The cat is the only species to our knowledge where the central projections of the ganglion cells have been examined and all morphological classes of ganglion cell shown to project to the tectum (Leventhal et al.,1985). The ipsilateral projection is often less homogeneous and in some of the above studies, where the analysis was based on soma size, it was observed that the small ganglion cells did not project to the ipsilateral tectum (Rapaport and Wilson, 1983; Hofbauer and Drager, 1985).

Two of the four types of ganglion cell that we observe projecting to the tectum are “displaced,” with their soma located in the inner nuclear layer (Fig. 9). In the pigeon, displaced ganglion cells have been shown to project selectively to the accessory optic system (Karten et al., 1977; Fite et al., 1981). This, however, is a vertebrate exception as opposed to a rule, as the displaced ganglion cells in the majority of vertebrates, as in the lamprey, project to other targets, including the tectum/superior colliculus (Hayes and Holden, 1983; Famiglietti, 1990; Martinez-Marcos et al., 2002; Abdel-Majid et al., 2005).

The relative proportion of the total ganglion cells projecting to the tectum varies substantially across the vertebrate phylum. Here we show that ~50% of all types of ganglion cells project to the tectum. This is similar to that in cat (40–50%; Wassle and Illing, 1980) and in the hamster (50%; Chalupa and Thompson, 1980). Only a few species have a lower proportion of tectal projecting ganglion cells, e.g., opossum (31%; Rapaport and Wilson, 1983) and monkey (10%; Perry and Cowey, 1984). If the proportion of ganglion cells that project to a structure is an indication of its importance for processing visual information, then a larger proportion of visual processing occurs outside the lamprey tectum than in species such as mice, where 70% of the ganglion cells project to the tectum (Hofbauer and Drager, 1985). This figure is even higher in rats (90%; Linden and Perry, 1983), pigeons (85%; Hayes and Holden, 1980), and frogs (85%; Singman and Scalia, 1990).

The proportion of each type of ganglion cell that projects to the tectum is not uniform, rather 34% of the IGCa, 70% of the IGCb, 82% of the OGCa, and 43% of the OGCb project to the tectum. Interestingly, those cells with a low proportion (IGCa and OGCb) have dendrites in the vitread sublayer of the inner plexiform layer (IPLi). It may be possible that these cells project to a different tectal lamina, as is the case with ganglion cells in mice (Hofbauer and Drager, 1985). However, the injections sites were analyzed and encompassed all visuorecipient layers. Here we also showed that the largest IGCa do not project to the tectum, and a low proportion of the largest cell type, the OGCb, project to the tectum. In other vertebrate species it has been shown that the largest ganglion cells project to the lateral geniculate nucleus (Rapaport and Wilson, 1983; Leventhal et al., 1985; Lugo-Garcia and Kicliter, 1988). Thus, another explanation for the low proportion of IGCa and

OGCb projecting to the tectum could be that these large ganglion cells project to the lamprey homolog of the lateral geniculate nucleus.

Retinotopy. The retinotectal projection is arranged in a retinotopic manner in the cyclostomes P. marinus and L. fluviatilis. This retinotopic arrangement is shared with all other vertebrates studied, including frogs (Gaze, 1958), fish (Jacobson and Gaze, 1964), birds (Frost et al., 1990), rats (Diao et al., 1983), cats (Apter, 1945), and primates (Cooper et al., 1953; Humphrey, 1968), suggesting that the retinotopic arrangement of the retinotectal connection was established prior to the separation of the jawed and jawless vertebrates _560 million years ago (Kumar and Hedges, 1998).

Despite the common feature of retinotopy between all vertebrates, there are differences in the arrangement of the map between species. The most common arrangement of the map is that the dorsal retina projects to the lateral tectum, the ventral retina projects to the medial tectum, the posterior retina to the rostral, and the anterior retina to the caudal tectum. This “classical” retinotopic arrangement is present in the lamprey, which suggests that any variations seen in other vertebrates, such as in the iguana, where the retinotopic map is rotated 90° (Stein and Gaither, 1981), are due to later individual species adaptation. The degree of ipsilateral input also varies between species. There is an ipsilateral input to the superior colliculus in mammals but it is sparse in rodents (Lund, 1965) and more extensive in primates (Hubel et al., 1975) and cats (Graybiel, 1975). In P. marinus, the lateral edge of the rostrocaudal midline receives ipsilateral input. This suggests that it may have a region of binocular vision that is then represented in the optic tectum. The possibility of binocular vision in P. marinus is also supported by the specific retinal input this area receives. The middle part of the tectum receives input from the contralateral and the ipsilateral posterior retina, and the natural stimuli that would coactivate these regions would come from objects directly in front of the animal, and so are in the same visuotopic space.

Relation to behavior. The efferent motor output of the lamprey tectum has been mapped by Saitoh et al. (2007), who reported that the type of eye, trunk, and locomotor movements observed depended on the spatial location and intensity of the stimulation. The motor patterns observed were grouped into four characteristic patterns of motor behavior. These were classed as: Type I, orienting responses, where a combination of eye movements, neck bending, and locomotion were observed; Type II, rhythmic eye and neck movements; Type III, downward shift of both eyes and downward body bending; and Type IV, forward swimming with no eye and neck movements. Using the data on the organization of the retinal input, the retinotopic map (present study) and the motor map (Saitoh et al., 2007) were spatially overlapped to observe whether there is a spatial correlation between what behavior is induced by stimulating a specific region of the optic tectum, and what specific retinal input these regions receive (Fig. 7C).

Stimulation of all areas of the optic tectum can induce evasive movements, which would take the animal away from where the natural visual stimuli would be perceived (Type I, II, IV movements all take the animal away from where the natural stimuli would be perceived). In contrast, orienting movements are only observed when the rostrolateral tectum is stimulated (Type I, movements can move the animal toward or away from where the natural stimuli would be perceived). This area of the tectum receives input from the area of the retina with the highest density of retinal ganglion cells. The density of retinal ganglion cells is one of the factors that determine visual acuity (Land, 2002); in other species this has been shown to be important for object discrimination (Harman et al., 2001). If a visual stimulus were presented to an area of the lamprey retina with a low visual acuity, where it is not possible to discriminate between prey and predator, it would be an advantage to evade this stimulus and avoid potentially orienting toward a predator. This is what is observed with the stimulation of the lamprey tectum, areas that receive input from parts of the retina with a low retinal acuity when stimulated give rise to purely evasive movements, whereas stimulation of the rostrolateral tectum that receives input from the area of the posterior retina, the area with the highest density of retinal ganglion cells, gives rise to both orienting and evasive movements. The predominance of the tectum controlling orienting or evasive behavior depends on the level of predation the animal is subject to (Dean et al., 1989). In animals subject to intense predation, such as the lamprey, stimulation of the tectum/ superior colliculus can induce both orienting and evasive behavior (Sahibzada et al., 1986). However, stimulation of the superior colliculus of animals not subject to intense predation such as primates predominately induces orienting behavior (Robinson, 1972). Despite this, the superior colliculus in these animals has still been shown to play a role in inducing evasive behavior (King and Cowey, 1992). Despite the difference in density, we have also shown that all areas of the tectum receive input from the four morphological types of tectal projecting ganglion cells independent of whether they can induce evasive or orienting behavior. This suggests that different retinal ganglion cells in the lamprey do not encode different features selective for prey as opposed to predators, as is the case for other species such as frogs (Lettvin et al., 1968).

4.3.2 Pretectal projecting retinal ganglion cells and relation to behavior

The lamprey pretectum, as described in the introduction, has been shown to be important for both escape swimming in response to sudden visual stimuli and the dorsal light response (Ulle´ n et al., 1993, 1997; Deliagina and Fagerstedt, 2000). Here we show that the pretectal nucleus receives input from two morphologically distinct types of retinal ganglion cell, the bipolar ganglion cells and OGCc, both having dendrites that stratify sclerad of the inner nuclear layer and potentially directly contact photoreceptors. In the lamprey, the two pretectal visual behaviors that have been described can be elicited by global eye illumination, a stimulus that has no motion component. The ganglion cells that respond to global illumination would need to simply respond to the intensity of light. Interestingly, the OGCc and bipolar ganglion cells are in a unique position to fulfill this need, as they both have dendrites vitread of the inner nuclear layer and so could form the direct connections between photoreceptors and ganglion cells, which are observed in lamprey (Rio et al., 1998). This is similar to other vertebrates where the pretectum controls the pupillary light reflex (Trejo and Cicerone, 1984); here the pretectum, as in the lamprey, receives input from a class of ganglion cell that directly contacts rod photoreceptors; these ganglion cells express melanopsin and are intrinsically photosensitive (Hattar et al., 2002). Despite this intrinsic photosensitivity, the pupillary light reflex at least in part relies on the direct contacts between the rod photoreceptors and these ganglion cells (Guler et al., 2008). While it would be premature to suggest homologies between these ganglion cells and those observed in the lamprey, it is clear that both in the lamprey and other vertebrates the pretectum receives input from the nonimage-forming part of the retina, where information from the photoreceptors is directly conveyed to ganglion cells and then monosynaptically to the pretectum. The projections from the nonimage-forming retina in other species such as the melanopsin-expressing ganglion cells in mice, project to other areas of the brain including the suprachiasmatic nucleus and the lateral habenula (Hattar et al., 2006). Future studies will have to be performed to test if the projections from OGCc cells follow a similar pattern.

The ganglion cells that transmit the sensory signal that will induce the dorsal light response need to respond when the dark dorsal aspect of the body is no longer facing the light source (Ulle´ n et al., 1997). By virtue of their morphology, projections, and distribution, located in a small portion of the ventral-medial retina, the bipolar ganglion cells seem well suited to fulfill this requirement. When the dorsal aspect of the body is rotated toward the light source, light will hit the most ventral portion of the retina. If the body rolls or the light source moves then the light will illuminate a larger portion of the ventral retina. It is at this point that the bipolar ganglion cells could respond, thereby communicating that the dorsal aspect of the body is no longer rotated toward the light. This is the first time to our knowledge that a specific ganglion cell type has been suggested to be involved in the dorsal light response, although a causal link still remains to be established between this cell type and the behavior. Whether other fish also have a similar specialization or whether they employ a different mechanism to carry out the dorsal light response will have to be investigated in future studies.

4.4 Conclusion

In conclusion, we show here that there are at least six distinct morphological types of retinal ganglion cells in P. marinus, four of which project to tectum in a retinotopic manner, with the posterior retina being represented in the anterior part of tectum. The density of ganglion cells in the posterior retina is the highest, representing the visual field in front of the lamprey. The dendrites of all four subtypes are distributed in the inner plexiform layer, which may, as in other vertebrates, represent the retinal processing layer necessary for image formation.

In contrast, the remaining two types of ganglion cells project to pretectum and their dendrites ramify in the outer plexiform layer or at the outer limiting membrane (OGCc1–2 and bipolar ganglion cells). These cells are therefore well placed to form the direct contacts between the photoreceptors and ganglion cells, which are observed in lamprey (Rio et al., 1998), and may constitute the output from the nonimage-forming part of the retina. These retinal ganglion cells would be well suited to carry information with minimal delay from the eye to elicit both the visual escape response and the dorsal light response, both of which are dependent on the pretectum and but not on the tectum.

Acknowledgment

We thank Dr. Peter Walle´ n and Dr. Jeremy Cook for comments on the article.

4.5 References

1. Abdel-Majid RM, Archibald ML, Tremblay F, Baldridge WH. 2005. Tracer coupling of neurons in the rat retina inner nuclear layer labeled by Fluorogold. Brain Res 1063:114 –120.
2. Abercrombie M. 1946. Estimation of nuclear population from microtome sections. Anat Rec 94:239 –247. Apter JT. 1945. Projection of the retina on superior colliculus of cats. J Neurophysiol 8:123–134.
3. Britto LR. 1983. Retinal ganglion cells of the pigeon accessory optic system. Braz J Med Biol Res 16:357–363.
4. Chalupa LM, Thompson I. 1980. Retinal ganglion cell projections to the superior colliculus of the hamster demonstrated by the horseradish peroxidase technique. Neurosci Lett 19:13–19 Collin SP. 2008. A database of retinal topography maps. Clin Exp Optom 91:85–95. Database at URL http://www.optometrists.asn.au/ceo/ retinalsearch
5. Collin SP, Knight MA, Davies WL, Potter IC, Hunt DM, Trezise AE. 2003. Ancient colour vision: multiple opsin genes in the ancestral vertebrates. Curr Biol 13:R864 – 865.
6. Cook JE, Kondrashev SL, Podugolnikova TA. 1996. Biplexiform ganglion cells,

characterized by dendrites in both outer and inner plexiform layers, are regular, mosaic-forming elements of teleost fish retinae. Vis Neurosci 13:517–528.

7. Cooper S, Daniel PM, Whitteridge D. 1953. Nerve impulses in the brainstem and cortex o the goat; spontaneous discharges and responses to visual and other afferent stimuli. J Physiol 120:514 –527.
8. Davies WL, Cowing JA, Carvalho LS, Potter IC, Trezise AE, Hunt DM, Collin SP. 2007. Functional characterization, tuning, and regulation of visual pigment gene expression in an anadromous lamprey. FASEB J 21: 2713–2724.
9. de Miguel E, Rodicio MC, Anadon R. 1989. Ganglion cells and retinopetal fibers of the larval lamprey retina: an HRP ultrastructural study. Neurosci Lett 106:1– 6.
10. de Miguel E, Rodicio MC, Anadon R. 1990. Organization of the visual system in larval lampreys: an HRP study. J Comp Neurol 302:529 –542.
11. Dean P, Redgrave P, Westby GW. 1989. Event or emergency? Two response systems in the mammalian superior colliculus. Trends Neurosci 12:137–147.
12. Deliagina TG, Fagerstedt P. 2000. Responses of reticulospinal neurons in intact lamprey to vestibular and visual inputs. J Neurophysiol 83:864–878.
13. Deliagina TG, Beloozerova IN, Zelenin PV, Orlovsky GN. 2008. Spinal and supraspinal postural networks. Brain Res Rev 57:212–221.
14. Diao YC, Wang YK, Xiao YM. 1983. Representation of the binocular visual field in the superior colliculus of the albino rat. Exp Brain Res 52:67–72. Dogiel AS. 1883. Die Retina der Ganoiden. Arch Mikrosk Anat 22:419 – 472.
15. Doi M, Uji Y, Yamamura H. 1995. Morphological classification of retinal ganglion cells in mice. J Comp Neurol 356:368 –386.
16. Ekstro¨m P. 1987. Photoreceptors and CSF-contacting neurons in the pineal organ of a teleost fish have direct axonal connections with the brain: an HRP-electron-microscopic study. J Neurosci 7:987–995.
17. Famiglietti EV. 1990. A distinct type of displaced ganglion cell in a mammalian retina. Brain Res 535:169 –173.
18. Fite KV, Brecha N, Karten HJ, Hunt SP. 1981. Displaced ganglion cells and the accessory optic system of pigeon. J Comp Neurol 195:279 –288.
19. Fritzsch B, Collin SP. 1990. Dendritic distribution of two populations of ganglion cells and the retinopetal fibers in the retina of the silver lamprey (Ichthyomyzon unicuspis). Vis Neurosci 4:533–545.
20. Frost BJ, Wise LZ, Morgan B, Bird D. 1990. Retinotopic representation of the bifoveate eye of the kestrel (Falco spraverius) on the optic tectum. Vis Neurosci 5:231–239.
21. Gaze RM. 1958. The representation of the retina on the optic lobe of the frog. Q J Exp Physiol Cogn Med Sci 43:209 –214.
22. Graybiel AM. 1975. Anatomical organization of retinotectal afferents in the cat: an autoradiographic study. Brain Res 96:1–23.
23. Grillner S. 2003. The motor infrastructure: from ion channels to neuronal networks. Nat Rev Neurosci 4:573–586.
24. Guler AD, Ecker JL, Lall GS, Haq S, Altimus CM, Liao HW, Barnard AR, Cahill H, Badea TC, Zhao H, Hankins MW, Berson DM, Lucas RJ, Yau KW, Hattar S. 2008. Melanopsin cells are the principal conduits for rod-cone input to non-image-forming vision. Nature 453:102–105.
25. Gustafsson OS, Collin SP, Kroger RH. 2008. Early evolution of multifocal optics for well-focused colour vision in vertebrates. J Exp Biol 211: 1559–1564.
26. Harman A, Dann J, Ahmat A, Macuda T, Johnston K, Timney B. 2001. The
27. retinal ganglion cell layer and visual acuity of the camel. Brain Behav

28. Evol 58:15–27.
29. Hattar S, Liao HW, Takao M, Berson DM, Yau KW. 2002. Melanopsincontaining retinal ganglion cells: architecture, projections, and intrinsic photosensitivity. Science 295:1065–1070.
30. Hayes BP, Holden AL. 1980. Size classes of ganglion cells in the central yellow field of the pigeon retina. Exp Brain Res 39:269 –275.
31. Hayes BP, Holden AL. 1983. The distribution of displaced ganglion cells in the retina of the pigeon. Exp Brain Res 49:181–188.
32. Hendrickson A. 1966. Landolt's club in the amphibian retina: a Golgi and electron microscope study. Invest Ophthalmol 5:484 – 496.
33. Hofbauer A, Drager UC. 1985. Depth segregation of retinal ganglion cells projecting to mouse superior colliculus. J Comp Neurol 234:465– 474.
34. Holmberg K. 1970. The hagfish retina: fine structure of retinal cells in Myxine glutinosa, L., with special reference to receptor and epithelial cells. Z Zellforsch Mikrosk Anat 111:519 –538.
35. Hubel DH, LeVay S, Wiesel TN. 1975. Mode of termination of retinotectal fibers in macaque monkey: an autoradiographic study. Brain Res 96:25–40.
36. Humphrey NK. 1968. Responses to visual stimuli of units in the superior colliculus of rats and monkeys. Exp Neurol 20:312–340.
37. Jacobson M, Gaze RM. 1964. Types of visual response from single units in the optic tectum and optic nerve of the goldfish. Q J Exp Physiol Cogn Med Sci 49:199 –209.
38. Karten JH, Fite KV, Brecha N. 1977. Specific projection of displaced retinal ganglion cells upon the accessory optic system in the pigeon (Columbia livia). Proc Natl Acad Sci U S A 74:1753–1756.
39. Research in Systems Neuroscience The Journal of Comparative Neurology 274 M.R. JONES ET AL. Kennedy MC, Rubinson K. 1977. Retinal projections in larval, transforming and adult sea lamprey, Petromyzon marinus. J Comp Neurol 171:465–479.
40. King SM, Cowey A. 1992. Defensive responses to looming visual stimuli in monkeys with unilateral striate cortex ablation. Neuropsychologia 30: 1017–1024.
41. Kuffler SW. 1953. Discharge patterns and functional organization of mammalian retina. J Neurophysiol 16:37– 68.
42. Kumar S, Hedges BS. 1998. A molecular timescale for vertebrate evolution. Nature 392:917–920.
43. Kusunoki T, Amemiya F. 1983. Retinal projections in the hagfish, Eptatretus burgeri. Brain Res 262:295–298.
44. Leventhal AG, Rodieck RW, Dreher B. 1985. Central projections of cat retinal ganglion cells. J Comp Neurol 237:216 –226.
45. Linden R, Perry VH. 1983. Massive retinotectal projection in rats. Brain Res 272:145–149.
46. Locket NA. 1970. Landolt's club in the retina of the African lungfish, Protopterus aethiopicus, Heckel. Vision Res 10:299 –306.
47. Lugo-Garcia N, Kicliter E. 1988. Morphology of ganglion cells which project to the dorsal lateral geniculate and superior colliculus in the ground squirrel. Brain Res 454:67–77.
48. Lund RD. 1965. Uncrossed visual pathways of hooded and albino rats.
49. Science 149:1506 –1507.
50. Mariani AP. 1982. Biplexiform cells: ganglion cells of the primate retina that contact photoreceptors. Science 216:1134 –1136.
51. Mariani AP. 1990. Amacrine cells of the rhesus monkey retina. J Comp
52. Neurol 301:382– 400.
53. Martinez-Marcos A, Lanuza E, Martinez-Garcia F. 2002. Retinal ganglion cells projecting to

the optic tectum and visual thalamus of lizards. Vis Neurosci 19:575–581.

54. Maslim J, Webster M, Stone J. 1986. Stages in the structural differentiation of retinal ganglion cells. J Comp Neurol 254:382– 402.
55. Nelson R, Famiglietti EV Jr, Kolb H. 1978. Intracellular staining reveals different levels of stratification for on- and off-center ganglion cells in cat retina. J Neurophysiol 41:472– 483.
56. Nishimura Y. 1980. Determination of the developmental pattern of retinal ganglion cells in chick embryos by Golgi impregnation and other methods. Anat Embryol 158:329 –347.
57. Ott M, Walz BC, Paulsen UJ, Mack AF, Wagner HJ. 2007. Retinotectal ganglion cells in the zebrafish, Danio rerio. J Comp Neurol 501:647–658.
58. Perry VH, Cowey A. 1984. Retinal ganglion cells that project to the superior colliculus and pretectum in the macaque monkey. Neuroscience 12: 1125–1137.
59. Polyak SL. 1941. The retina. Chicago: University of Chicago Press.
60. Pombal MA, Abalo XM, Rodicio MC, Anadon R, Gonzalez A. 2003. Choline acetyltransferase-immunoreactive neurons in the retina of adult and developing lampreys. Brain Res 993:154 –163.
61. Provis JM, Watson CR. 1981. The distribution of ipsilaterally and contralaterally projecting ganglion cells in the retina of the pigmented rabbit. Exp Brain Res 44:82–92.
62. Pushchin, II, Kondrashev SL. 2003. Biplexiform ganglion cells in the retina of the perciform fish Pholidapus dybowskii revealed by HRP labeling from the optic nerve and optic tectum. Vision Res 43:1117–1133.
63. Ramon y Cajal S. 1972. The structure of the retina [compiled by Thorpe SA, Glickstein M). Springfield, IL: Charles C. Thomas.
64. Rapaport DH, Wilson PD. 1983. Retinal ganglion cell size groups projecting to the superior colliculus and the dorsal lateral geniculate nucleus in the North American opossum. J Comp Neurol 213:74 – 85.
65. Repe´ rant J, Vesselkin NP, Ermakova TV, Kenigfest NB, Kosareva AA. 1980. Radioautographic evidence for both orthograde and retrograde axonal transport of labeled compounds after intraocular injection of [3H]proline in the lamprey (Lampetra fluviatilis). Brain Res 200:179–183.
66. Repe´ rant J, Vesselkin NP, Kenigfest NB, Miceli D, Rio JP. 1982. Bidirectional axonal and transcellular transport of [3H]adenosine from the lamprey retina. Brain Res 246:305–310.
67. Rio JP, Vesselkin NP, Repe´ rant J, Kenigfest NB, Versaux-Botteri C. 1998. Lamprey ganglion cells contact photoreceptor cells. Neurosci Lett 250:103–106.
68. Robinson DA. 1972. Eye movements evoked by collicular stimulation in the alert monkey. Vision Res 12:1795–1808.
69. Rodieck RW, Watanabe M. 1993. Survey of the morphology of macaque retinal ganglion cells that project to the pretectum, superior colliculus, and parvicellular laminae of the lateral geniculate nucleus. J Comp Neurol 338:289 –303.
70. Rubinson K, Cain H. 1989. Neural differentiation in the retina of the larval sea lamprey (Petromyzon marinus). Vis Neurosci 3:241–248.
71. Sahibzada N, Dean P, Redgrave P. 1986. Movements resembling orientation or avoidance elicited by electrical stimulation of the superior colliculus in rats. J Neurosci 6:723–733.
72. Saitoh K, Me´ nard A, Grillner S. 2007. Tectal control of locomotion, steering, and eye movements in lamprey. J Neurophysiol 97:3093–3108.
73. Shen SC, Greenfield P, Boell EJ. 1956. Localization of acetylcholinesterase in chick retina during histogenesis. J Comp Neurol 106:433– 461.
74. Singman EL, Scalia F. 1990. Quantitative study of the tectally projecting retinal ganglion cells in the adult frog: I. The size of the contralateral and ipsilateral projections. J Comp Neurol 302:792– 809.

75. Stein BE, Gaither NS. 1981. Sensory representation in reptilian optic tectum: some comparisons with mammals. J Comp Neurol 202:69 – 87.
76. Toth P, Straznicky C. 1989. Biplexiform ganglion cells in the retina of Xenopus laevis. Brain Res 499:378 –382.
77. Trejo LJ, Cicerone CM. 1984. Cells in the pretectal olivary nucleus are in the pathway for the direct light reflex of the pupil in the rat. Brain Res 300:49 – 62.
78. Ulle´ n F, Orlovsky GN, Deliagina TG, Grillner S. 1993. Role of dermal photoreceptors and lateral eyes in initiation and orientation of locomotion in lamprey. Behav Brain Res 54:107–110.
79. Ulle´ n F, Deliagina TG, Orlovsky GN, Grillner S. 1997. Visual pathways for postural control and negative phototaxis in lamprey. J Neurophysiol 78:960 –976.
80. Vanegas H. 1984. Comparative neurology of the optic tectum. New York: Plenum Press.
81. Vesselkin NP, Repe´ rant J, Kenigfest NB, Miceli D, Ermakova TV, Rio JP. 1984. An anatomical and electrophysiological study of the centrifugal visual system in the lamprey (Lampetra fluviatilis). Brain Res 292:41–56.
82. Villar-Cervino V, Abalo XM, Villar-Cheda B, Melendez-Ferro M, Perez- Costas E, Holstein GR, Martinelli GP, Rodicio MC, Anadon R. 2006. Presence of glutamate, glycine, and gamma-aminobutyric acid in the retina of the larval sea lamprey: comparative immunohistochemical study of classical neurotransmitters in larval and postmetamorphic retinas. J Comp Neurol 499:810 – 827.
83. Villar-Cheda B, Abalo XM, Anadon R, Rodicio MC. 2006. Calbindin and calretinin immunoreactivity in the retina of adult and larval sea lamprey. Brain Res 1068:118 –130.
84. Wa¨ ssle H, Illing RB. 1980. The retinal projection to the superior colliculus in the cat: a quantitative study with HRP. J Comp Neurol 190:333–356.
85. Wa¨ ssle H, Dacey DM, Haun T, Haverkamp S, Grunert U, Boycott BB. 2000. The mosaic of horizontal cells in the macaque monkey retina: with a comment on biplexiform ganglion cells. Vis Neurosci 17:591– 608.
86. Wye-Dvorak J, Straznicky C. 1991. Retinal distribution of ganglion cells which project to the ipsilateral optic tectum in Bufo marinus. Brain Res 555:313–318.
87. Zompa IC, Dubuc R. 1998. Diencephalic and mesencephalic projections to rhombencephalic reticular nuclei in lampreys. Brain Res 802:27–54.
88. Zrenner E, Nelson R, Mariani A. 1983. Biplexiform ganglion cells of the primate retina with direct contact with photoreceptors. Fortschr Ophthalmol 80:516 –519.

5. Introduction: Tectoreticular pathway and its link to visuomotor control (poster)

Symmetric activation of the brainstem descending pathway that drives the rhythmic pattern generators in the spinal cord provides the basis for the propulsive machinery responsible for swimming, all of which is well understood in the lamprey. However, for the animal to turn, steering commands must generate asymmetric activation of brainstem descendingcommands via the reticulospinal cells. The optic tectum has an active role in this. Another important aspect for studying visuo-moto coordination in lamprey is the fact that the lamprey retina provides a retinotopic projection to the tectum and that stimulation of the tectum gives rise to sitespeci _c eye/head movements and _nally also locomotor movements (Saitoh et al., 2007; Jones et al., 2009). However, for the optic tectum to generate a movement, the removal of the tonic inhibition produced by the basal ganglia is required. Our long-term goal is to decipher the tectal microcircuit and to provide an understanding of its role during visuomotor control during steering.

Aims

1. To determine the distribution of tectal e_erents that aris from the motor (deep) layer of the optic tectum projecting to the brainstem.
2. To explore their morphological features and physiological properties.

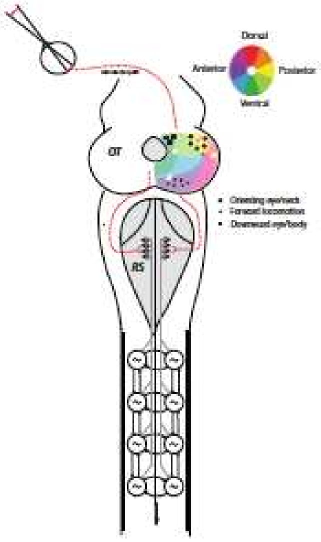

Figure 1. *Schematic of the lamprey brain representing processes during visuomotor control.*
Visual information arrives to the super_cial layer of the optic tectum (OT) at locations shown by the colour coded retinal input. Black dots, squares and stars show the motor responses that arise from stimulation of these tectal sites. Tectal output activates the reticulospinal (RS) cells in the brainstem which then in turn activate the central pattern generators that causes the animal to turn towards and away from stimuli in its environment.

Methods

1. **Neuronal tract tracing**

   Alexa Fluor 488, Dextran Biotin and Neurobiotin were injected into the brainstem and the optic tectum and visualised with Streptavidin-Cy2/Cy3 and counterstained with a fluorescent Nissl stain.

2. **Electrophysiology**

   Tectal cells were investigated with whole-cell recordings patch clamp recording in acute tranverse brain slices at 8°C. Cells were prelabelled with dextran-rhodamine after injections into theMRRN. Animals were then left for 24-48 hours after to facilitate transport.

Neuroanatomy

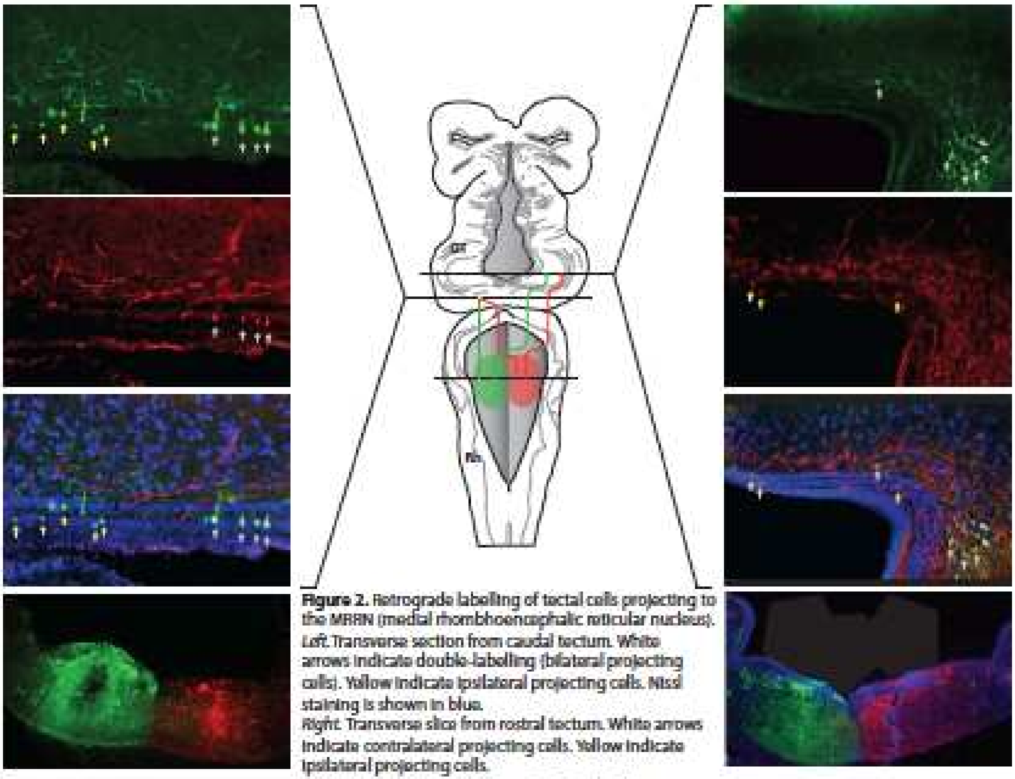

Figure 2. Retrograde labelling of tectal cells projecting to the MRRN (medial rhombhoencephalic reticular nucleus).
Left. Transverse section from caudal tectum. White arrows indicate double-labelling (bilateral projecting cells). Yellow indicate ipsilateral projecting cells. Nissl staining is shown in blue.
Right. Transverse slice from rostral tectum. White arrows indicate contralateral projecting cells. Yellow indicate ipsilateral projecting cells.
Bottom images show injection sites from both cases, respectively.

Electrophysiology

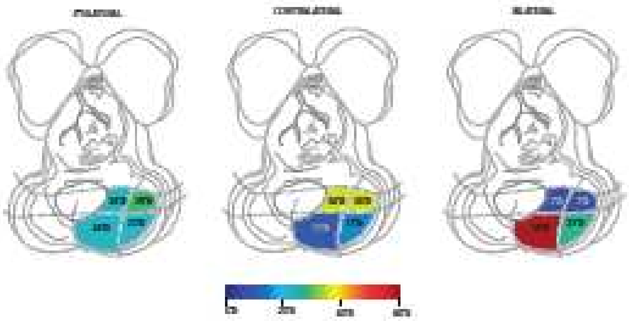

Figure 3. Distribution of tectal cell types (ipsilateral, contralateral and bilateral) across the optic tectum (n = 14) divided into a 4 by 4 grid spanning rostrocaudally and mediolaterally.

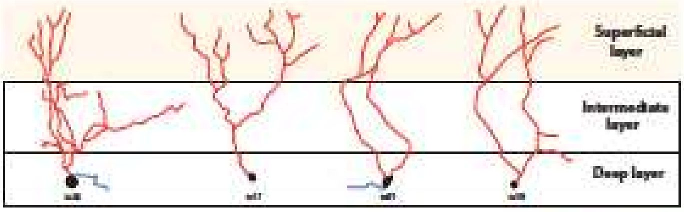

Figure 4.

Top. Morphology of tectal cells that are located in the deep (output) layer. Red traces indicate dendrites; Blue traces indicate axons; Black circular areas indicate cell somas.

Right. Transverse tectal section illustrating the columnar structure between superficial (input) layer and deep layer by small injection of neurobiotin in superficial layer.

Figure 5. *Top.* Infra-red image of an ipsilaterally projecting tectal cell, pre-labelled from MRRN during whole-cell patch recordings.
Middle. Fluorescent image of the same cell indicating its prelabelling. *Bottom.* Same cell, intracellularly filled with neurobiotin to reveal its morphological characteristics.

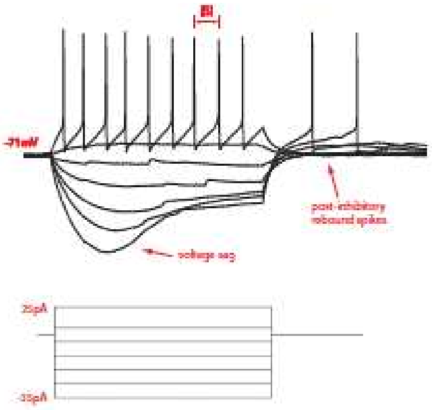

Figure 6. *Top.* Voltage responses of a tectal cell to hyperpolarising and depolarising 1 s current steps of 5 pA per step, elicited from rest at –71 mV. This cell exhibits a regular firing pattern and post-inhibitory rebound action potentials upon hyperpolarization. *Bottom.* Current steps used to drive the voltage response above.

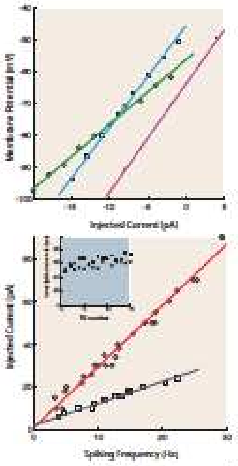

ry

Figure 7. *Top.* I–V plot of the steady-state voltage deflections to current steps of three different tectal cells. *Bottom.* I-F plot; plot of injected current as a function of the firing rate during a 1 s current pulse in two cells. *Inset.* Inter spike intervals (ISI) plotted against the ISI illustrating the regular firing patterns of these cells at about 15Hz.

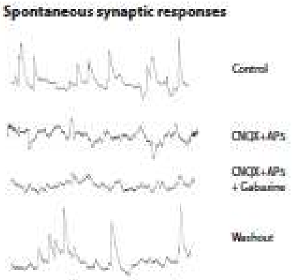

Figure 8. Current clamp recordings of spontaneous synaptic input at –70 mV. The upper trace shows synaptic input during control conditions. The rest of the traces show synaptic input after the application of specific drugs applied in the bath solution.

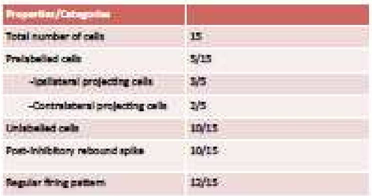

Properties/Categories	
Total number of cells	15
Prelabelled cells	5/15
-Ipsilateral projecting cells	3/5
-Contralateral projecting cells	2/5
Unlabelled cells	10/15
Post-inhibitory rebound spike	10/15
Regular firing pattern	12/15

Conclusion

1. **Ipsilateral** projecting cells, responsible for avoidance, are distributed equally across tectum. **Contralateral** projecting cells, responsible for orienting responses, are located mostly rostrally. **Bilateral** projecting cells are located caudally and maybe responsible for forward locomotion.

2. Morphological analysis of tectal cells in deep layers reveals that **a)** their dendrites extend to *and* through the super_cial layer, and **b)** main dendritic arbouration occurs in the retinorecipient super_cial layer.

3. Whole-cell patch recordings show that these cells exhibit a regular _ring pattern with post-inhibitory rebound spikes.

References

1. Saitoh K, Ménard A, Grillner S. 2007. Tectal control of locomotion, steering, and eye movements n lamprey. J Neurophysiol 97:3093-3108.

2. Jones M.R., Grillner S. and Robertson B. 2009. Selective Projection Patterns from Subtypes of Retinal Ganglion Cells to Tectum and Pretectum – Distribution and Relation to Behavior. J. Comp Neurol. 517:257–275.

Acknowledgments

This work was supported by EU FP7 Select-and-Act 2007-201716, EU FP7 Lampreta-2008-216100 and Karolinska Institutet research funds.